Nanoscale Devices for Studying Quantum Fluids and Electrostatic Field-Effects in Superconducting Nanoconstrictions

Andrew John Guthrie (MPhys)

Supervisor: Dr. Sergey Kafanov
Dr. Viktor Tsepelin

Department of Physics
University of Lancaster

This dissertation is submitted for the degree of
Doctor of Philosophy

February 2020

Declaration

I hereby declare that except where specific reference is made to the work of others, the contents of this dissertation are original and have not been submitted in whole or in part for consideration for any other degree or qualification in this, or any other university. This thesis is my own work and that of my collaborators, as specified in the text and Author's contributions. I declare that the total number of words in this thesis is 30,629, and therefore does not exceed 80,000 words.

Andrew John Guthrie (MPhys)
February 2020

Acknowledgements

Experimental low-temperature research is always a collective effort and this thesis is no different. The work in this thesis would not be possible without the support of both the ULT and QTC groups. I would particularly like thank my supervisors, Sergey and Viktor. I attribute this project's success to Sergey's tireless enthusiasm and commitment, coupled with Viktor's expert guidance and patience. Without their hard work and ingenuity, I would definitely not have got this far.

I would like to thank all the group members for their contributions. Special thanks go to Yuri for his help with all the papers, Malcolm and Roch for installing the ^{4}He lines, Alan for keeping the helium flowing, Kunal for his support in the cleanroom, and Stephen Holt and his team for the excellent electrical help. Thanks to Josh and Alex for their help with the fridges, answering my many questions, and for always being up for a discussion. I would also like to mention Jon, Dima, Samuli and Rich for their excellent words of wisdom.

A special thanks go to Josh, Ash, Alex, Theo, Ilya, Xiao, and Francis for the 11am coffee train that kept me awake, Friday pub trips that kept me sane, and for being a constant source of amusement and support. Collectively you make the physics department a fantastic place to work. A special mention goes to the Mountaineering Society for giving me friends for life, and more adventures than I can can count. I would like to thank my parents for their constant support and patience, and giving me a place to escape my work stress. I am also forever indebted to my partner Sophie, for being the best friend, and rock, that I needed throughout this difficult journey.

Abstract

Nanofabricated devices, where the characteristic dimension is less than one micron (10^{-6} m), have remarkable potential as highly sensitive tools to observe the quantum world to which we belong. By operating such devices at extremely low temperatures we can engineer physical scenarios never before seen in nature. Investigating the laws which govern at such small energy and length scales has the potential to upend our current understanding of the universe. This thesis introduces two main bodies of experimental work, both of which utilise nanoscale devices as precise detectors for various unique quantum phenomena.

In Part I, nanomechanical devices with extremely high mass sensitivity were used as probes of quantum fluids, namely superfluid ^{4}He. We present the first measurements of nanomechanical devices in superfluid ^{4}He, measuring the spectra of thermal excitations, and use our devices to demonstrate a new quasiparticle driving mechanism, which we call the ‘phonon wind’. Here, a nanobeam can be moved coherently under the influence of a modulated flux of thermal excitations. We go on to use nanobeams as high-speed detectors for the phenomenon of quantized vortices in ^{4}He, ultimately concluding with the systematic study of a single vortex trapped by a nanobeam. We also present the first measurements of micromechanical torsional tuning forks in superfluid ^{4}He, demonstrating a unique multimode detection scheme where torsional oscillations are used to sense quantised vortices generated by flexural oscillations.

In Part II, nanoelectronic devices with extremely high charge sensitivity were used as probes of the superconducting field-effect. The superconducting field-effect, as previously observed in nanoconstrictions, is a completely unexpected phenomenon and cannot theoretically coexist with the well-established Bardeen, Cooper and Schrieffer theory of superconductivity. Using a gated Dayem bridge coupled to a high-frequency circuit, we characterise this effect with far greater time resolution than previously possible, demonstrating that the observed effect is merely a result of electron tunnelling causing localised heating in the constriction.

Table of contents

List of publications xi

Author's contributions xiii

List of figures xvii

List of tables xix

Nomenclature xxi

I Nanoscale Devices for Probing Quantum Fluids 1

1 Introduction 3

2 Superfluidity in ^{4}He 5

2.1 Two-Fluid Model 7

2.1.1 Sound Propagation in Superfluids 8

2.2 Superfluid Excitations 10

2.3 Quantum Turbulence in Superfluid ^{4}He 13

3 Mechanical Oscillators 17

3.1 Damped, Driven Oscillators 18

3.1.1 Duffing Oscillators 19

3.2 Nanomechanical Beams 21

3.2.1 Euler-Bernoulli Beam Theory 21

3.2.2 Thermalisation of Nanomechanical Beams 23

3.3 Tuning Forks 24

3.4 Dissipation in Oscillating Structures 26

3.4.1 Clamping Losses 27

3.4.2 Thermoelastic Effect 27

3.4.3 Magnetomotive Damping 28

3.5 Dissipation for Oscillating Structures in Superfluid ^{4}He 28

3.5.1 Hydrodynamic Regime 29

3.5.2 Ballistic Regime 30

3.5.3 Acoustic Dipole Emission 32

3.5.4 Acoustic Quadrupole Emission 32
3.5.5 Cavitation 33
3.5.6 Quantum Turbulence 34
3.6 Quantum Vortices Trapped by a Nanoscale Beam 36
3.7 Driving Nanoscale Beams using a Phonon Flux 37
3.7.1 Detected Power from a Phonon Flux. 38
3.7.2 Noise Power from Thermal Fluctuations 39

4 Experiments on Nanoscale Beams in ^{4}He **41**
4.1 Samples 41
4.2 Measurement Scheme 42
4.2.1 2 Port Scattering Parameters 43
4.3 Results 45
4.3.1 Vacuum 45
4.3.2 Hydrodynamic Regime of ^{4}He 48
4.3.3 Ballistic Regime of ^{4}He 51
4.3.4 Driving a Nanobeam with a Phonon Flux 56
4.4 Conclusions and Outlook 58

5 Experiments on Vortex Dynamics probed by Nanoscale Beams **61**
5.1 Samples 61
5.2 Measurement Scheme 62
5.3 Results 63
5.3.1 Characterisation 63
5.3.2 Real-Time Vortex Dynamics 64
5.3.3 Properties of Trapped Vortices 68
5.4 Conclusions and Outlook 71

6 Experiments on Multimode Torsional Tuning Forks in ^{4}He **73**
6.1 Samples 73
6.2 Measurement Scheme 74
6.2.1 Calibration using using Doppler Vibrometry 75
6.3 Results 76
6.3.1 Vacuum 76
6.3.2 Response of Multimode Fork in ^{4}He 77
6.3.3 Multimode Detection of Quantum Turbulence 79
6.3.4 Coupling two Tuning Forks with Quantum Turbulence 80
6.4 Conclusions and Outlook 81

II Field-Effect in Superconducting Nanoconstrictions **83**

7 Introduction **85**

8 Superconductivity **87**
8.1 Surface Impedance 88
8.2 Josephson Effect 90
8.3 Superconducting Transmission Lines 92
8.3.1 Quarter Wavelength Resonator 93

9 Experiments on JoFETs Coupled to Microwave Cavities **95**
9.1 Samples 95
9.2 Measurement Scheme 96
9.2.1 3 Port Scattering Parameters 97
9.3 Results 98
9.3.1 Spectroscopy Measurements 98
9.3.2 Noise Measurements 100
9.4 Field-Electron Emission 103
9.4.1 Current-Voltage Measurements 104
9.5 Conclusions and Outlook 105

References **107**

A Experimental Details **115**
A1 Scattering Parameters 115
A2 Experimental Cells 115
A3 Cryostats 115
A3.1 1 K Cryostat:I 115
A3.2 1 K Cryostat:II 117
A3.3 Cryogen-Free Dilution Cryostat 121
Nanobeam measurements in ^{4}He cell 122
Vortex measurements using nanobeams in ^{4}He cell 123
JoFET measurements 123

B Recipes **125**
B1 Al-on-Si Nanomechanical Beams 125
B2 Al-on-Si_3N_4 Nanomechanical Beams 126
B3 JoFETs Coupled to Superconducting Resonators 127

C Software **129**

List of publications

The following publications are the result of the work presented in this thesis:

I ‘Probing superfluid ^{4}He with high-frequency nanomechanical resonators down to millikelvin temperatures’ Phys. Rev. B 100, 020506(R) (2019) (Chapter 4)

II ‘Detecting a “phonon flux” in superfluid ^{4}He by a nanomechanical resonator’ Phys. Rev. B 101, 060503(R) (2020) (Chapter 4)

III ‘Real-Time Quantum Vortex Detection using a Nanoscale Resonator in Superfluid ^{4}He at millikelvin Temperatures’ In Preparation (Chapter 5)

IV ‘Multimode probing of ^{4}He by tuning forks’ Appl. Phys. Lett. 115, 113103 (2019) (Chapter 6)

V ‘On the Origin of the Superconducting Field-Effect in Gated-Nanoconstrictions’ In Preparation (Chapter 9)

Author's contributions

This thesis revolves around five articles that I authored along with members of the ULT group at Lancaster University, and some external collaborators. Publications I, II and IV were prepared by the author, using cryogenic experimental data and analysis collected and performed by the author, with the help of Dr. S. Kafanov, Prof. Yu. A. Pashkin, Dr. V. Tsepelin, Prof. O. Kolosov. The nanobeam samples for these experiments were fabricated in Grenoble Alpes University by Dr. E. Collin, O. Maillet and R. Gazizulin. The initial calibration of the tuning fork was performed by Prof. O. Kolosov and M. Mucientes. The initial measurements in bulk ^{4}He were done with the help of Dr. M. Sarsby and A. Jennings. For publication III, the author designed and installed the experiment, and played a central role in data collection and analysis, and co-wrote the paper along with Dr. M. T. Noble, with the help of Dr. S. Kafanov and Dr. V. Tsepelin. The samples were fabricated at Moscow State University by A. A. Dorofeev, V. A. Krupenin and D. E. Presnov. For publication V, the author designed the samples, played a major role in fabrication and installing the experiment, and was central in the data collection and analysis, along with Dr. S. Kafanov and I. Golokolenov. The manuscript was prepared by Dr. S. Kafanov, and Prof. Yu. A. Pashkin. Data for all experiments presented were taken using software developed by myself.

List of figures

2.1 Phase diagram for ^{4}He 6
2.2 Two-fluid model for ^{4}He 8
2.3 First sound velocity in ^{4}He 10
2.4 Dispersion relation for superfluid ^{4}He 11
2.5 Schematic of a quantum vortex. 14
2.6 Kelvin-wave cascade diagram 15
2.7 Kelvin-wave cascade diagram 16

3.1 Lorentzian function. 19
3.2 Frequency response of a Duffing oscillator. 20
3.3 Magnetic actuation of nanomechanical device. 21
3.4 Schematic showing thermalisation of a nanobeam. 23
3.5 Quartz tuning fork schematic and readout 26
3.6 Hydrodynamic fluid clamping to a nanobeam 29
3.7 Hydrodynamic fluid clamping to a nanobeam 31
3.8 Critical velocity for turbulence production as a function of frequency . . . 35
3.9 Process of vortex reconnection 37

4.1 SEM of two nanoscale beams 42
4.2 PCBs for mounting nanoscale beams 43
4.3 Schematic of a 2-port scattering matrix 44
4.4 Plot of fundamental frequency for various nanobeam lengths. 46
4.5 Duffing-like behaviour in 150 μm Al-on-Si_3N_4 47
4.6 Magnetic damping for two Al-on-Si nanoscale beams 48
4.7 Field dependence in vacuum for two Al-on-Si_3N_4 nanoscale beams 49
4.8 Temperature dependence of the resonance for three Al-on-Si nanobeams . 50
4.9 Temperature and field dependence for two Al-on-Si_3N_4 nanobeams in ^{4}He 52
4.10 Force velocity for two Al-on-Si_3N_4 nanobeams in vacuum and ^{4}He 54
4.11 Time-dependence of resonance properties for Al-on-Si_3N_4 nanobeam in ^{4}He 55
4.12 Schematic of measurement scheme for detecting a phonon flux 57
4.13 Spectra and power dependence for a phonon flux signal 58

5.1 SEM of Moscow State Si_3N_4 nanobeams 62
5.2 PCB for ^{4}He vortex dynamics measurements 63

5.3 Force-velocity for nanobeam and TF in ^{4}He at 10 mK. 64
5.4 Example of vortex frequency shift event for a nanobeam in ^{4}He 65
5.5 Histograms of vortex event rate and length for nanobeam in ^{4}He. 67
5.6 Magnetic field dependence of damping for several vortex configurations. . 69
5.7 Damping for the 1st, 3rd and 5th harmonics in ^{4}He after vortex event. . . 70

6.1 SEM of 76 kHz TF with dimensions shown. 74
6.2 PCB used for measurements of two torsional TFs. 75
6.3 Optical calibration data from Doppler-vibrometer. 76
6.4 Force-velocity for multimode tuning fork in vacuum and ^{4}He 78
6.5 Frequency sweep for flexural and torsional mode 79
6.6 Temperature Dependence of both tuning fork resonances 80
6.7 Multimode detection scheme for TFs in superfluid ^{4}He 81

8.1 Schematic showing expulsion of magnetic field in a superconductor 88
8.2 Density of states in a superconductor 89
8.3 Current-voltage characteristics for Josephson Junction 91
8.4 Schematic of a unit cell for a coplanar waveguide 93
8.5 Current and voltage distribution for a quarter wavelength resonator . . . 94

9.1 SEM of resonator coupled Dayem bridge chip 95
9.2 PCB and Sample holder for for CPW coupled JoFET measurements . . . 96
9.3 Diagram of 3-Port scattering in a resonator coupled to a feedline 97
9.4 Gate dependence of the measured Lorentzian for CPW coupled JoFET . . 99
9.5 Frequency shift and quality factor for CPW coupled JoFET 100
9.6 Conversion to frequency noise from voltage noise data 101
9.7 Spectral density and spectral density gradient for CPW coupled JoFET . 102
9.8 Schematic representation of field-electron emission 103
9.9 Differential conductance from the gate of a CPW coupled JoFET 105

A.1 Photographs of two helium cell designs 116
A.2 Photograph of 1 K cryostat setup 116
A.3 Photograph of 1 K cryostat insert 118
A.4 Electrical schematic for nanobeam measurements above 1 K 118
A.5 Schematic of glass immersion cryostat for helium measurements 119
A.6 Electrical schematic for tuning fork measurements 119
A.7 Photograph of dilution cryostat for measurements below 1 K 121
A.8 Image of cryostat with mounted cell 122
A.9 Electrical Schematic for nanobeam measurements at 7 mK 123
A.10 Electrical schematic for TF measurements at 1 K 123
A.11 Electrical schematic for JoFET measurements at 7 mK 124

C.1 Live-plotting GUI for the data-collection software. 130
C.2 Live-plotting output for the data analysis script. 131

List of tables

4.1 Hydrodynamic fitting parameters for nanomechanical beam in ^{4}He 51

6.1 Table of tuning fork parameters 77

Nomenclature

Physical Constants

ϵ_0	Permittivity of free space
$\hbar$	Reduced Planck's constant
e	Electron charge
h	Planck's constant
k_B	Boltzmann constant

Acronyms / Abbreviations

EBPVD	Electron Beam Physical Vapour Deposition
FFT	Fast-Fourier-Transform
FWHM	Full Width at Half Maximum
JoFET	Josephson Field Effect Transistor
LDV	Laser Doppler Vibrometer
MEMS	Micro-Electro-Mechanical Systems
MLA	Multi-frequency-Lock-in-Amplifier
NEMS	Nano-Electro-Mechanical Systems
NMR	Nuclear Magnetic Resonance
PCB	Printable Circuit Board
RF	Radio Frequency
SA	Spectrum Analyser
ScS	Superconductor-Superconducting constriction-Superconductor
SEM	Scanning Electron Microscope
SIS	Superconductor-Insulator-Superconductor

SMA	Sub-Miniature Type-A
SMP	Sub-Miniature Pushable
SNS	Superconductor-Normal Metal-Superconductor
SQUID	Superconducting Quantum Interference Device
SS’S	Superconductor^1-Superconductor^2-Superconductor^1
TF	Tuning Fork
VNA	Vector Network Analyser
VWR	Vibrating Wire Resonator

Part I

Nanoscale Devices for Probing Quantum Fluids

Chapter 1

Introduction

Superfluid ^{3}He and ^{4}He are truly remarkable systems, due to the fact they are macroscopic objects yet still exhibit quantum behaviour. Superfluids possess a plethora of quantum phenomena and collective excitations unique to these systems, making them a topic of scientific fascination since their discovery. Careful measurements of superfluid behaviour could yield insight into some of the great unsolved problems in physics by linking the field of condensed matter physics to that of high-energy physics and cosmology. From the outset, mechanical oscillators, where properties of the fluid are inferred from the motion of a vibrating object, have provided an invaluable tool for superfluid research.

This work presents several experiments involving micro and nano-scale mechanical oscillators undertaken in superfluid ^{4}He at ultra-low temperatures, embracing the recent advances in nanofabrication techniques pushed forward by the microprocessor industry. In doing so, we firmly establish the suitability of nanoscale mechanical devices for use in future experiments.

Firstly, we will discuss experiments demonstrating the use of nano-electro-mechanical systems (NEMS) in superfluid ^{4}He across a broad temperature range showcasing their remarkable versatility. Our work include the first measurements of NEMS in bulk superfluid ^{4}He, and at mK temperatures in ^{4}He, exploring the full range of dissipation mechanisms present. We go on to introduce a unique quasiparticle driving mechanisms using a resonant 'phonon wind' in ^{4}He, the first demonstration of such an effect.

Secondly, with our knowledge of nanoscale beam behaviour, we can create an experiment for the detection of single quantum vortices in ^{4}He. Here, a quartz tuning fork (TF) is used as a source of vortex rings, suspended above a nanomechanical beam which is used as a detector. We demonstrate the real-time detection of vortex-nanobeam interactions on the time-scale of milliseconds, and go on to measure the properties of trapped vortices under several configurations.

Lastly, we will discuss experiments probing superfluid ^{4}He using micro-tuning forks with a well defined torsional mode, where the tines twist inwards and outwards in anti-phase. In typical experiments, quartz TFs with resonant frequencies in the kilohertz range, operating in the flexural mode, have been used. For flexural oscillations the legs flex inwards in antiphase normally comprising the lowest frequency mode. There has been little study into the mechanics of higher-order harmonics or twisting modes operating in a superfluid. In addition, we demonstrate a novel measurement technique where two oscillation modes on a single device are used to separate the excitation and detection mechanisms. These comprise the first example of the ‘multimode’ technique with potential application both inside and outside of low-temperature research.

Chapter 2 will outline the discovery and underlying physics of the superfluid state, including the various successful models in different temperature regimes. Chapter 3 will introduce the general theory of operation for mechanical oscillators, and specify to that of doubly-clamped beams and TFs. This chapter will introduce the limited previous uses of nanomechanical devices as low-temperatures probes, as well as their use in the wider community. Three experimental chapters, Chapter 4, Chapter 5 and Chapter 6, will discuss the experiments involving NEMS in ^{4}He, quantum vortex detection in ^{4}He and multimode TFs in ^{4}He, respectively.

Chapter 2

Superfluidity in ^{4}He

Despite being the second most abundant element in the universe, helium was not discovered on earth until 1895 when Sir William Ramsey first obtained the inert gas from the mineral ore clevite [1]. ^{3}He and ^{4}He comprise the two stable isotopes of helium with the heavier isotope constituting 99.999863% abundance. ^{4}He was first liquefied in 1908 by Kamerlingh Onnes whilst working at Leiden by cooling a sample of gas below 4.2 K [2]. Owing to the small Van-der-Waals force, due to the large zero point energy, ^{4}He does not undergo a liquid-solid transition at any temperature at atmospheric pressure [3]. The absence of a solid state at low-temperatures allows the phenomena known as superfluidity to manifest. Despite reaching a temperature of 1.7 K, well below the superfluid transition, Onnes made no observations of any additional phase change below the liquid transition. He achieved these record breaking temperatures using a liquid nitrogen precooling stage combined with a Hampson-Linde cycle. It wasn't for another twenty-four years, in 1932, that the first signs of an additional phase transition were observed, when Keesom and Clausius noticed a diverging specific heat capacity of ^{4}He close to 2.17 K, which they named the λ-point [4]. Six years later, in 1938, Allen and Misener [5], and Kapitza [6] independently observed a vanishing viscosity of the helium liquid below the λ-point. Kapitza termed this effect 'superfluidity' to describe the ability of this substance to flow with seemingly no resistance. The superfluid state persists down to the lowest temperatures at atmospheric pressure, and is suppressed by pressures > 25 bar. The phase diagram for ^{4}He is shown in Fig. 2.1.

In the superfluid state, helium enters a phase ordered state, such that the fluid can be described by a single wavefunction in which all ^{4}He atoms in the condensate occupy the lowest energy level allowed by the uncertainty principle. This condensate requires breaking the gauge symmetry with respect to the phase parameter, in stark contrast to symmetric systems where the observables are invariant to changes in the wavefunction phase. The Pauli exclusion principle states that no two fermions can occupy the same quantum state. Condensation can occur because ^{4}He atoms act as bosons owing to an integer combined spin of the nucleus, allowing the atoms to occupy the same energy level in the condensate. The wavefunction for superfluid ^{4}He is given by

$$\psi(r) = \psi_0 e^{i\varphi(r)}, \tag{2.1}$$

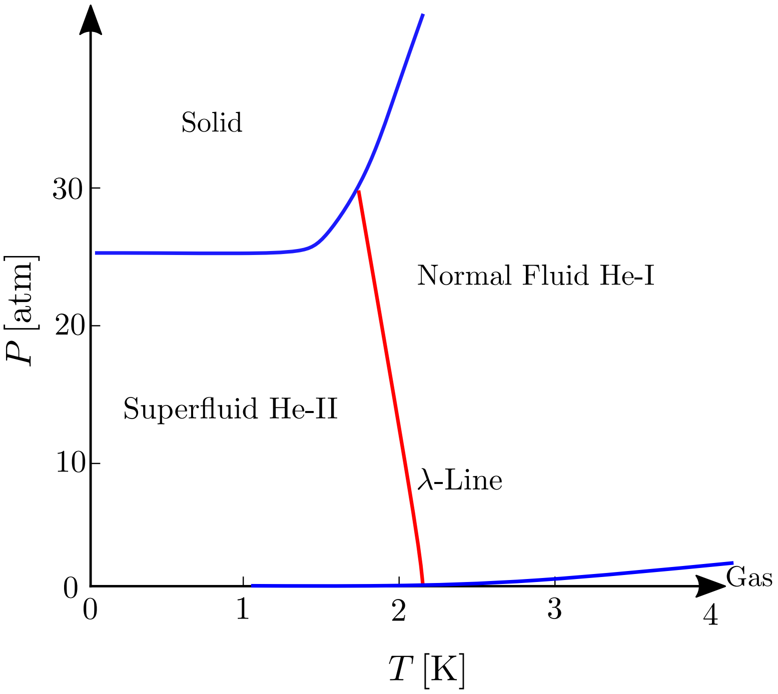

Fig. 2.1 Phase diagram for ^{4}He in the vicinity of the superfluid transition. At atmospheric pressure this transition occurs at $T = 2.17\,\mathrm{K}$. ^{4}He only has a liquid-solid transition at high pressure ($> 25\,\mathrm{atm}$). Importantly, ^{4}He has no triple point as would be found in most materials. Adapted from [7].

where $\varphi(r)$ is the superfluid phase, a function of the position r, and the amplitude given by

$$\psi^*\psi = |\psi_0|^2 = \frac{\rho_s}{m_4}, \tag{2.2}$$

where m_4 is the mass of a ^{4}He atom, and ρ_s is the superfluid density. The momentum of a ^{4}He atom in the condensate can be represented by the momentum operator

$$\hat{p}\psi = -i\hbar\nabla\psi, \tag{2.3}$$

and hence the superfluid velocity

$$\mathbf{v}_s = \frac{\hbar}{m_4}\nabla\varphi(r). \tag{2.4}$$

It is clear that the superfluid velocity directly determines the phase of the wavefunction. The particles in the condensate form a bound-state in momentum space, with the superfluid phase rigidly defined at all points in space.

The most striking manifestation of superfluidity is the ability to flow through extremely narrow capillaries without experiencing any friction [6, 5], however this is not the only remarkable property of superfluid ^{4}He. Superfluids have been shown to escape over the walls of a beaker when suspended above the helium bath [8]. They also exhibit the thermomechanical, or fountain, effect, whereby a heater immersed in a superfluid ^{4}He vessel containing a superleak causes fluid to 'fountain' out of the leak [9]. Superfluids also demonstrate what is known as 'second-sound', in which waves of temperatures propagate coherently through the fluid, allowing the generation of standing waves of temperature [10]. Such a process can only occur due to the incredible heat conductivity of ^{4}He close to T_λ, the highest of any known material [3]. This is achieved by submerging a heater and thermometer in a cavity of variable length, L, in liquid ^{4}He and driving the heater with an AC current. By varying the frequency, f, of the current one finds longitudinal resonant standing modes at frequencies $f = nc_1/2L$, where c_1 is the wave-speed and $n = 1, 2, 3 \ldots$.

2.1 Two-Fluid Model

To explain these remarkable behaviours, Landau [11] and Tisza [12] independently proposed the phenomenological 'two-fluid model' which treats the superfluid state as a mixture of two interpenetrating, non-interacting components. In reality, you cannot distinguish between individual ^{4}He atoms in the condensate and therefore the two-fluids cannot actually be separated. Despite this, the two-fluid model has remarkable success in explaining many of the observed phenomena of superfluid ^{4}He. The total density, ρ, is given by the sum of the densities of the two individual components

$$\rho = \rho_n + \rho_s, \tag{2.5}$$

where ρ_n is the normal fluid density, and ρ_s is the superfluid density. In the two-fluid model, at $T = 0$ the normal fluid component vanishes. Correspondingly, the superfluid fraction goes to zero at the λ-point temperature, T_λ. Importantly, only the normal-fluid component has non-zero entropy, S, and viscosity, ν. The first measurements of the temperature dependence of the normal-fluid fraction were experimentally realised by Andronikashvili in 1946 using an oscillating stack of torsional discs [13]. The relative quantities of the two-fluid fractions in the liquid phase are shown in Fig. 2.2.

We want to understand how the motion of the two components gives rise to observed phenomena, in particular sound emission. In the two-fluid model, the momentum density of mass flow can we written as

$$\mathbf{j} = \rho_n \mathbf{v}_n + \rho_s \mathbf{v}_s, \tag{2.6}$$

where $\mathbf{v}_n$ and $\mathbf{v}_s$ are the velocity of the normal and superfluid component respectively. In this formulation

$$\frac{\partial \rho}{\partial t} = -\nabla \cdot \mathbf{j} \tag{2.7}$$

represents the continuity equation. Since the viscosity of the normal-fluid is very low, its influence can be neglected to a first-order approximation, and can be treated as an ideal fluid, described by the Euler equation [3]

$$\frac{\partial \mathbf{j}}{\partial t} + \rho_n \mathbf{v}_n \cdot \nabla \mathbf{v}_n = -\nabla p, \tag{2.8}$$

where p is the fluid pressure. The Euler equation is the equivalent of Newtons second law for systems with non-discretised mass. If the velocity remains low, as is the case

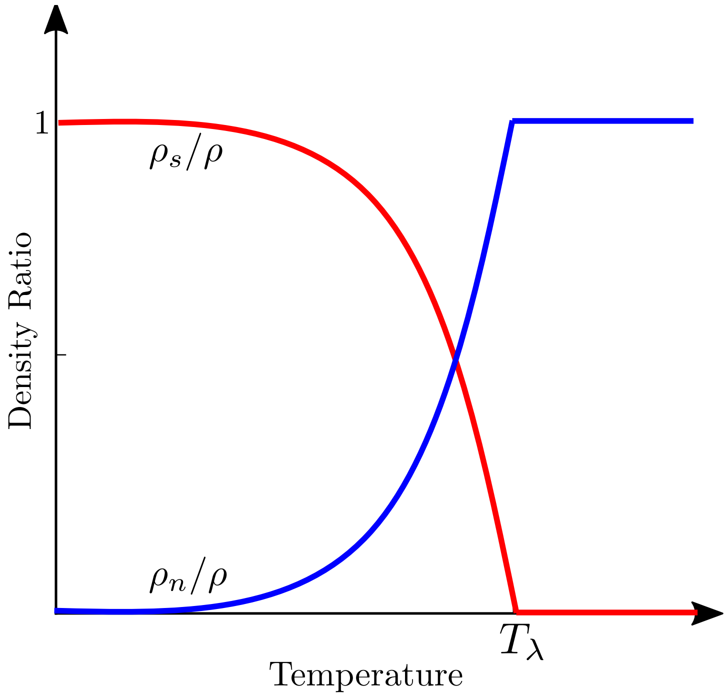

Fig. 2.2 Dependence of the normal and superfluid fractions of liquid ^{4}He on temperature.

in superfluid flow, the second term can be neglected. Since no dissipative process is occurring in this flow, entropy is conserved.

The equations of motion for the two components are therefore given by [3]

$$\frac{\partial(\rho S)}{\partial t} = \nabla \cdot (\rho S \mathbf{v}_n), \tag{2.9}$$

$$S\nabla T - \frac{1}{\rho}\nabla p = \frac{\partial \mathbf{v}_s}{\partial t}, \tag{2.10}$$

where p is the pressure acting on the system. Equation (2.9) and Eq. (2.10) represent the central equations of motion for the two-fluid model, which we will utilise to explain the process of sound propagation in the next section.

2.1.1 Sound Propagation in Superfluids

From a macroscopic perspective, a sound wave is a small oscillation in a thermodynamic quantity, typically density for classical sound. Superfluids have the ability to support multiple sound modes stemming from the behaviour of the two separate, yet interpenetrating fluids. Emission of sound has significant implications for the use of probes to measure fundamental helium physics, since it often dominates the damping at the lowest temperatures. The time differential of the continuity equation, Eq. (2.7), is given by

$$\frac{\partial^2 \rho}{\partial t^2} = \nabla \cdot \frac{\partial j}{\partial t}, \tag{2.11}$$

since $\partial/\partial t(\nabla \cdot A) = \nabla \cdot (\partial A/\partial t)$ for all A. By substituting this into into Eq. (2.8) we obtain that [3]

$$\frac{\partial^2 \rho}{\partial t^2} = \nabla^2 p. \tag{2.12}$$

Assuming a stationary fluid on average *i.e.* $\mathbf{v}_n = \mathbf{v}_s = 0$, and disregarding the terms of higher order (since we are only interested in small perturbations) in Eq. (2.9) and Eq. (2.10) gives the corresponding relation for temperature and entropy as

$$\frac{\partial^2 S}{\partial t^2} = \frac{\rho_s S^2}{\rho_n} \nabla^2 T. \tag{2.13}$$

To rewrite these two equations to be independent of the pressure terms, we substitute the total derivatives

$$dp = \left(\frac{\partial p}{\partial \rho}\right)_S d\rho + \left(\frac{\partial p}{\partial S}\right)_\rho dS, \tag{2.14}$$

$$dT = \left(\frac{\partial T}{\partial \rho}\right)_S d\rho + \left(\frac{\partial T}{\partial S}\right)_\rho dS. \tag{2.15}$$

Substituting these into the previous expression yields two wave equations, one for oscillations in the density (first-sound), and one for oscillations in the *entropy* (second-sound):

$$\frac{\partial^2 \rho}{\partial t^2} = \left(\frac{\partial p}{\partial \rho}\right)_S \nabla^2 p + \left(\frac{\partial p}{\partial S}\right)_\rho \nabla^2 S, \tag{2.16}$$

$$\frac{\partial^2 S}{\partial t^2} = \frac{\rho_s}{\rho_n}\left[\left(\frac{\partial T}{\partial \rho}\right)_S \nabla^2 \rho + \left(\frac{\partial T}{\partial S}\right)_\rho \nabla^2 S\right]. \tag{2.17}$$

To solve these differential wave equations two plane-wave solutions are used; one solution for oscillating density, and one solution for oscillating entropy. The two general solutions are given by

$$\rho(t) = \rho_0 + A_\rho \exp\left(i\omega(t - x)/v\right), \tag{2.18}$$

$$S(t) = S_0 + A_S \exp\left(i\omega(t - x)/v\right), \tag{2.19}$$

where ρ_0 and S_0 are the unperturbed density and entropy values, A_ρ and A_S are the amplitudes of the perturbations, and v is the wave propagation velocity. Substituting these solutions into the previous expressions and differentiating yields two linear equations

$$\left[\left(\frac{v}{u_1}\right)^2 - 1\right] A_\rho + \left(\frac{\partial p}{\partial S}\right)_\rho \left(\frac{\partial \rho}{\partial p}\right)_S A_S = 0, \tag{2.20}$$

$$\left[\left(\frac{v}{u_2}\right)^2 - 1\right] A_S + \left(\frac{\partial T}{\partial \rho}\right)_S \left(\frac{\partial S}{\partial T}\right)_\rho A_\rho = 0, \tag{2.21}$$

where the substitutions $u_1 = \left(\frac{\partial p}{\partial \rho}\right)_S$ and $u_2 = \rho_s/\rho_n S^2 \left(\frac{\partial T}{\partial S}\right)_\rho$. First sound occurs for oscillations in the density *i.e.* $A_\rho \neq 0$ and $A_S = 0$. We arrive at the conclusion that

$$\rho_n \frac{\partial}{\partial t}(\mathbf{v}_n - \mathbf{v}_s) = \rho S \nabla T = 0, \tag{2.22}$$

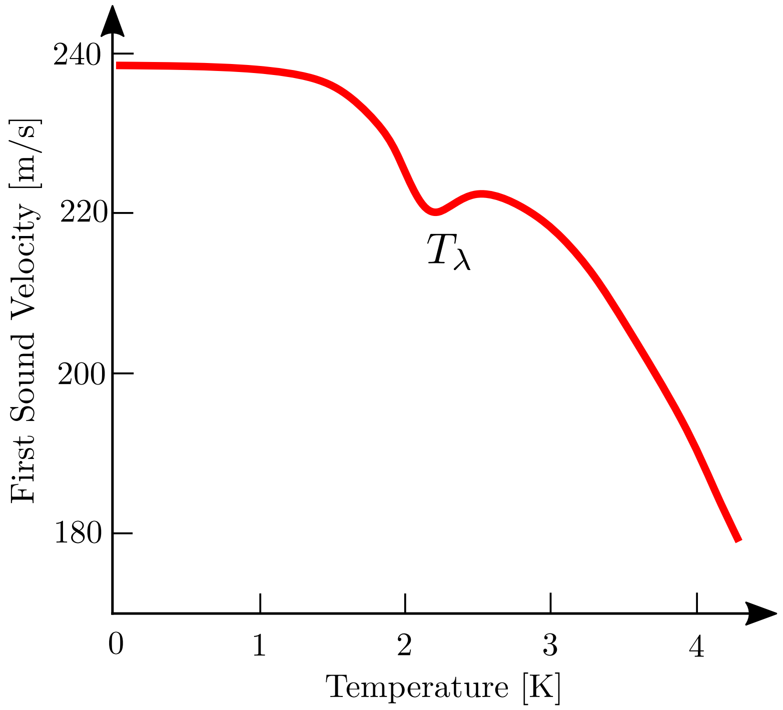

Fig. 2.3 Velocity of first sound in the temperature range $1\,\mathrm{K} < T < 4\,\mathrm{K}$ with the λ-point indicated. At the lowest temperatures, the first-sounds velocity is $\sim 238\,\mathrm{m\,s^{-1}}$. Adapted from [3].

and hence

$$\frac{\partial \mathbf{v}_n}{\partial t} = \frac{\partial \mathbf{v}_s}{\partial t}. \tag{2.23}$$

Importantly, since the two fluids are moving in phase first sound can be treated classically since there is no distinction between the two components. Such a result implies that the two types of sound are completely decoupled, which is typically only true far below T_λ. We go on to discuss the damping due first-sound emission in Sec. 3.5.3. The speed of first sound varies significantly over the temperature range $1\,\mathrm{K} < T < 4\,\mathrm{K}$, as shown in Fig. 2.3.

2.2 Superfluid Excitations

The two-fluid model provides an excellent description of superfluid ^{4}He and helps us to explain many of the observed phenomena. However, it is not a microscopic model explaining the origin of these phenomena. The first microscopic model was provided by Landau [14], when he realised that the presence of dissipationless flow must imply some kind of ground state, with a finite energy, Δ, required to create collective excitations. In this way, momentum transfer is not allowed for arbitrarily low velocities. Because of this energy gap, there must exist a finite critical velocity, v_L, above which superfluid flow will destroy the condensate. In 1941 Landau proposed two collective excitations in superfluid ^{4}He: longitudinal phonons with a linear dispersion, and rotons with a characteristic energy gap. The phonon is often referred to as the *Goldstone mode* of the system, since it is a gapless excitation corresponding to the spontaneous breaking of a global symmetry

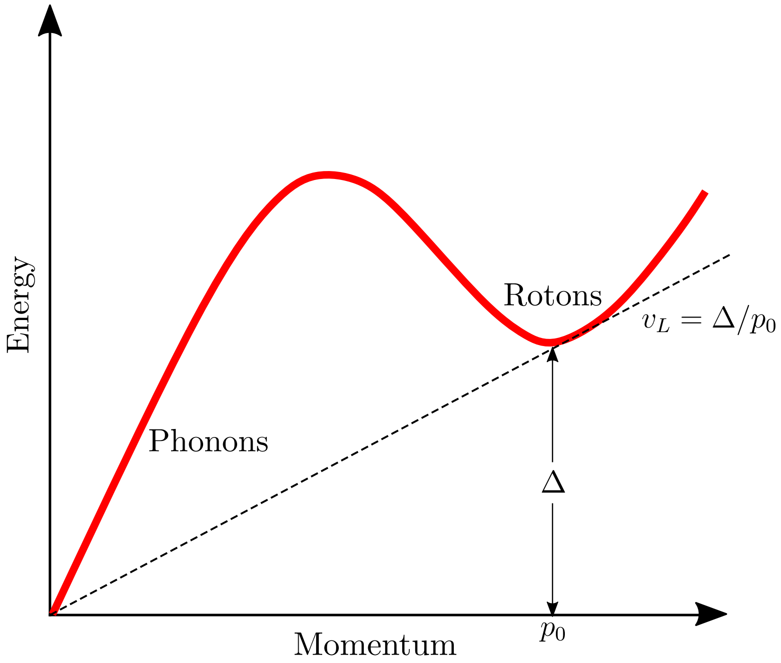

Fig. 2.4 Dispersion curve for excitation in superfluid ^{4}He. Two collective excitations are shown: longitudinal phonons, with a linear dispersion, and rotons, with a characteristic energy gap.

of the Lagrangian, *i.e.* the superfluid phase [15]. The exact microscopic origin of the roton mode in terms of gauge symmetry breaking is not well established.

In Landau's picture, superfluid helium is treated as a gas of these weakly interacting excitations. Rigorously, the thermodynamic properties are determined by the fluctuations in this quasiparticle field, where the excitations are treated as single-particle Green's functions [16]. For mathematical simplicity, the excitations will be discussed in terms of a kinematic picture rather than the exact quantum field description. The dispersion relation for phonons is given by

$$E = pc_{\mathrm{ph}}, \tag{2.24}$$

where p is the momentum, E is the energy and c_{ph} is the velocity of phonons. Importantly, since phonons are the origin of sound emission in the condensate, the velocity of first sound is determined by the phonon velocity ($u_1 = c_{\mathrm{ph}}$), and we shall use this notation from now on. In the vicinity of the p_0, the dispersion relation is approximated to be

$$E \approx \Delta + \frac{(p - p_0)^2}{2m^*}, \tag{2.25}$$

where p_0 is the roton momentum at the gap, and m^* is the effective mass of the excitation. The dispersion curve for superfluid ^{4}He is shown in Fig. 2.4 with these excitations highlighted. The Landau critical velocity is given by $v_L = \Delta/p_0 = 60\,\mathrm{m\,s^{-1}}$, indicated by the dashed-black line. Landau proposed that these two excitations are what comprise the normal fluid, such that

$$\rho_n = \rho_{\mathrm{ph}} + \rho_{\mathrm{ro}}, \tag{2.26}$$

where ρ_{ph} and ρ_{ph} are the phonon and roton densities respectively.

The number density of phonons can be calculated directly from Bose-Einstein statistics. From the dispersion relation given in Eq. (2.24), the phonon density of states per unit volume, $g(E)$ is given by

$$g_{\mathrm{ph}}(E)dE = \frac{E^2}{2\pi^2(c_{\mathrm{ph}}\hbar)^3}dE. \tag{2.27}$$

The number of phonons per unit volume can now be expressed as

$$N_{\mathrm{ph}} = \int_0^\infty \frac{g(E)dE}{\exp(E/k_{\mathrm{B}}T)-1} = \frac{1}{2\pi^2(c_{\mathrm{ph}}\hbar)^3}\int_0^\infty \frac{E^2 dE}{\exp(E/k_{\mathrm{B}}T)-1}. \tag{2.28}$$

By performing a substitution $x = E/k_{\mathrm{B}}T$, and hence $dx = dE/k_{\mathrm{B}}T$, the number density can be calculated as

$$N_{\mathrm{ph}} = 8\pi\zeta(3)\left(\frac{k_{\mathrm{B}}T}{c_{\mathrm{ph}}h}\right)^3, \tag{2.29}$$

where $\zeta(3) = 1.20$ is the Riemann zeta function. Similarly, the mass density can be calculated by substituting an effective mass $m^* \sim E/c_{\mathrm{ph}}^2$

$$\rho_{\mathrm{ph}} = \frac{1}{2\pi^2 c_{\mathrm{ph}}^5\hbar^3}\int_0^\infty \frac{E^3 dE}{\exp(E/k_{\mathrm{B}}T)-1} = \frac{2\pi^2(k_{\mathrm{B}}T)^4}{45 c_{\mathrm{ph}}^5\hbar^3}. \tag{2.30}$$

Using Eq. (2.25) the density of states of rotons is given by

$$g_{\mathrm{ro}}(E)dE = \frac{(E-\Delta)^{1/2}m^{*3/2}}{\sqrt{2}\pi^2\hbar^3}dE. \tag{2.31}$$

Rotons can be described by Boltzmann statistics, since they always contain a component of their energy, Δ, which is large compared to $k_{\mathrm{B}}T$ at low temperatures. The number density of rotons is hence given by

$$N_{\mathrm{ro}} = \int_0^\infty \frac{g(E)dE}{\exp(E/k_{\mathrm{B}}T)} = \frac{m^{*3/2}}{\sqrt{2}\pi^2\hbar^3}\int_0^\infty \frac{(E-\Delta)^{1/2}dE}{\exp(E/k_{\mathrm{B}}T)}. \tag{2.32}$$

Again, performing a substitution $x = (E-\Delta)/k_{\mathrm{B}}T$ and correspondingly $dx = dE/k_{\mathrm{B}}T$, the number density for rotons is given by

$$N_{\mathrm{ro}} = \left(\frac{m^* k_{\mathrm{B}}T}{2\pi\hbar^2}\right)^{3/2}\exp(-\Delta/k_{\mathrm{B}}T). \tag{2.33}$$

Finally, by applying same the logic as used to calculate the phonon density, the roton density is given by

$$\rho_{\mathrm{ro}} = \frac{2m^{*1/2}p_0^4}{3(2\pi)^{3/2}(k_{\mathrm{B}}T)^{1/2}\hbar^3}\exp(-\Delta/k_{\mathrm{B}}T). \tag{2.34}$$

The expressions calculated here will allows us to calculate the damping on an oscillator at a given temperature, giving us an effective means of thermometry in ^{4}He. Since we began from a microscopic picture of the superfluid excitations, the derived expressions are theoretically valid to arbitrarily low temperatures.

2.3 Quantum Turbulence in Superfluid ^{4}He

Similarly to classical turbulence, which describes the tendency for fluids to exhibit chaotic motion at high flow rates, *quantum* turbulence describes the chaotic motion of quantum fluids at high flow rates. At large length scales, quantum and classical turbulence have the tendency to mimic each other, however, at the scale of a single vortex the two are governed by different physics due to the quantized nature of vortices in quantum fluids [17]. Here we will introduce the physics of single vortices, and introduce systems of multiple vortices. In Sec. 3.5.6, we will go on to see how quantum turbulence affects objects at large length scales. How to reconcile these two regimes remains a major challenge, and is one of the major goals of quantum turbulence [18].

Initially, it was assumed that superfluids would not support internal circulation, *i.e.* $\nabla \times v_s = \nabla \times \nabla\varphi = 0$, however in 1955 Feynman questioned this assumption [19]. He suggested that the circulation in a superfluid must be quantized, with the core of the vortex corresponding to a topological defect in the quantum fluid [18]. He went on to proposed experiments on how to verify this. This effect was first observed by Vinen in 1961 and dubbed 'quantum turbulence' using a vibrating wire in a rotating ^{4}He vessel [20]. Upon rotation, vortices would become trapped along the length of the wire, such that the rotation split otherwise degenerate oscillation modes. If we consider a simply connected region of superfluid of length L, enclosing an area A the circulation in the region can be described by Stokes' theorem [7]

$$\kappa = \iint_A (\nabla \times \mathbf{v}_s) \cdot d\mathbf{A} = \oint_L \mathbf{v}_s \cdot d\mathbf{l}, \tag{2.35}$$

where $\mathbf{v}_s = \hbar\nabla\varphi(r)/m_4$, and m_4 is the mass of a ^{4}He atom. Hence,

$$\kappa = \hbar\Delta\varphi_L/m_4, \tag{2.36}$$

where $\Delta\varphi_L$ is the phase difference along the line integral. Since the superfluid is described by a single wavefunction, the phase difference along a closed loop must be integer multiples of 2π. The circulation then becomes

$$\kappa = \frac{h}{m_4}n, \quad \text{where} \quad n \in \mathbb{Z}. \tag{2.37}$$

Clearly, this result implies that vortices in superfluid ^{4}He can only take certain quantized values of $\kappa = (9.9 \times 10^{-8}\,\mathrm{m\,s^{-1}})n$. As in classical turbulence, the velocity of the superfluid component increases as you get closer to the centre of the vortex such that

$$v_s = \frac{\kappa}{2\pi r} = \frac{\hbar}{m_4 r}n. \tag{2.38}$$

The superfluid velocity rises until the Landau critical velocity is exceeded, and a normal fluid-like core is formed. The diameter of the normal fluid core is give by $d_0 = \kappa/2\pi v_c \approx 26\,\mathrm{nm}$. The diameter of this normal fluid core can be thought of as the distance over which

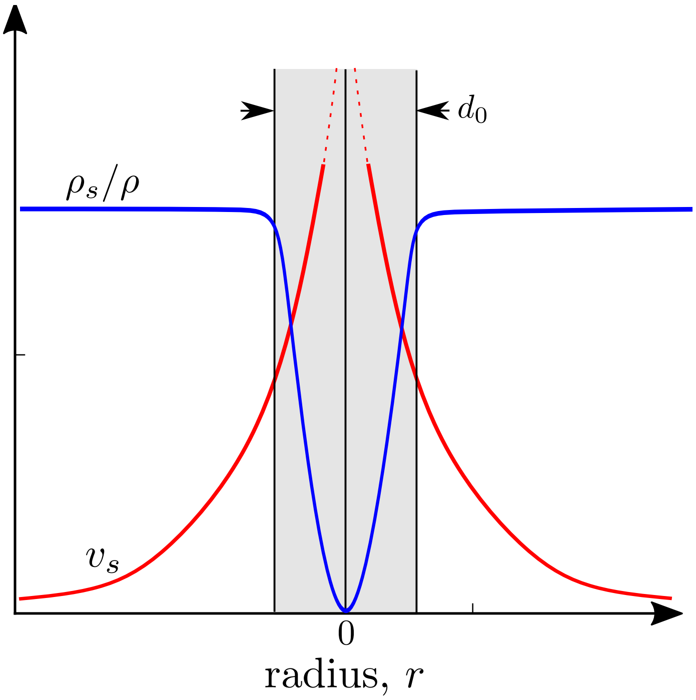

Fig. 2.5 Schematic illustration of superfluid velocity, and superfluid fraction as a function from a vortex core in ^{4}He. The grey region indicates where the superfluid velocity is greater than the Landau critical velocity, suggesting that the condensate is destroyed in the region.

the superfluid fraction can fall to zero from its bulk value. This is shown schematically in Fig. 2.5.

If we consider a container with multiple quantized vortices, the energy per unit length of each vortex, E_L, is calculated by integrating the kinetic energy per unit volume between the vortex-core, at distance d_0, to the nearest vortex, at distance b, and is given by [3]

$$E_L = \frac{\rho_s \kappa^2}{4\pi} \ln\left(\frac{2b}{d_0}\right), \tag{2.39}$$

Since $\kappa \propto n$, $E_L \propto n^2$. Although the angular velocity, $L \propto v/r$, increases linearly with n [3], the kinetic energy increases quadratically. For this reason, it is energetically favourable to create two vortices with $n = 1$, than one vortex with $n = 2$. Therefore remarkably, not only is the circulation quantized, it is identical for all vortices and has value h/m_4. For this reason, quantum turbulence is often described as an ‘ideal system’ for the study of classical turbulence; it is the simplest possible turbulent system.

Vortices in ^{4}He can form so-called ‘vortex rings’ where a vortex line of length $2\pi r_v$, where r_v is the ring radius, wraps to form a loop. The energy of a vortex ring is given by $E_r = 2\pi r_v E_L$, with the propagation velocity given by [3]

$$v_r = \frac{\kappa}{4\pi r_r}\left[\ln\left(\frac{2r_v}{d_0}\right) - \frac{1}{4}\right]. \tag{2.40}$$

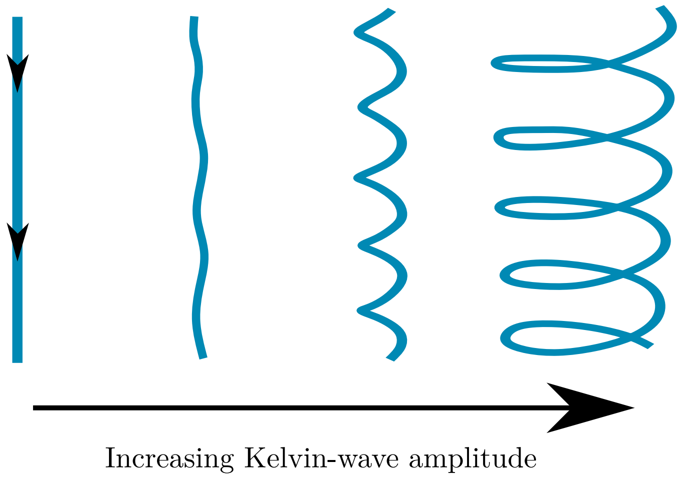

Fig. 2.6 Schematic representation of helical Kelvin wave excitations on a vortex line, shown in blue, for four different amplitudes. The scale of the displacement has been exaggerated for representation.

Quantum turbulence can be nucleated in ^{4}He either intrinsically or extrinsically. Intrinsic nucleation typically requires a high critical velocity ($v_c \sim 10\,\mathrm{m\,s^{-1}}$), whereas extrinsic (where existing vortex lines are manipulated under the influence of a superflow) can have much lower critical velocities ($v_c \sim 10^{-3}\,\mathrm{m\,s^{-1}}$) [18, 21]. The initial vortex lines in a system are typically created by the Kibble-Zurek mechanism, where the system is cooled quickly through the superfluid phase transition [22]. The phase cannot adjust everywhere at the same time, leading to topological defects in the condensate which manifest as quantum vortices.

Quantum turbulence is then dissipated by two processes. At high temperatures ($> 1\,\mathrm{K}$), mutual friction creates coupling between the normal-fluid and the superfluid producing dissipation. At lower temperatures, no significant normal-fluid fraction exists to introduce mutual friction, and dissipation is thought to come from Kelvin waves. Kelvin waves are helical displacements of vortex core, and allow energy to be transferred from large length-scales towards smaller length scales by a non-linear interaction between different wavenumbers. Helical Kelvin wave excitations are shown schematically in Fig. 2.6, for varying amplitude of the excitation. The dispersion relationship for Kelvin waves is given by [24]

$$\omega \approx \frac{\kappa k^2}{4\pi}, \tag{2.41}$$

where k is the wavenumber, meaning that shorter waves rotate faster.

In a classical fluid, energy transfers from large vortexes to smaller vortexes by the process of reconnection, following the Richardson cascade. The Richardson cascade is caused by reconnection of larger loops creating more smaller loops, allowing energy to 'cascade' to smaller length scales. The energy density relationship $E \propto k^{-5/3}$ for the Richardson cascade is an experimentally derived result. The process of vortex reconnection will be introduced in Sec. 3.6. In quantum turbulence, the Kelvin-wave cascade extends the Richardson cascade when the wavenumber scale reaches the mean inter-vortex spacing

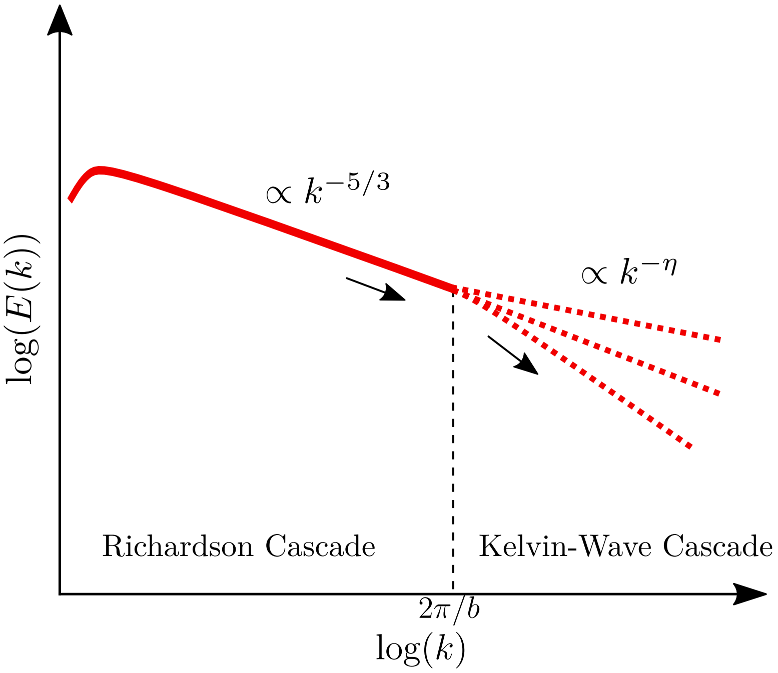

Fig. 2.7 Energy cascade spectra for quantum turbulence at zero temperature. For small wavenumbers ($k < 2\pi/b$) a Richardson cascade creates a Kolmogorov spectra ($E(k) = C\epsilon^{2/3}k^{-5/3}$), similar to that observed in classical turbulence. Above this, the wavenumber becomes comparable to the mean-inter-vortex distance, and the Kelvin-cascade dominates. The functional dependence of the Kelvin-wave energy spectra is not known, represented by the dashed lines. Adapted from [23].

in a quantum fluid. As such, the Richardson cascade is still measurable in quantum fluids at higher temperatures. The energy density spectra for Kelvin waves is not yet known, however using simulations it has been proposed that the exponent, ν, may be the same as that of the Richardson cascade [25], although since the microscopic origin of this result is completely different this is merely coincidence. The Kelvin-wave cascade excites higher wavenumber (and therefore smaller wavelength) modes, such that energy can be dissipated as fundamental excitations on the scale of the superfluid coherence length, typically by phonons in the form of sound. A schematic diagram of this process is shown in Fig. 2.7, where the arrows indicate the flow of energy. The dashed line indicates the region where the wavelength becomes smaller than the superfluid coherence length, in which energy is contained in the form of low energy phonons.

Superfluids clearly have a plethora of fascinating phenomena to be studied. In the next chapter, we will detail the operation of various mechanical oscillators, and how they can be used to probe various superfluid effects.

Chapter 3

Mechanical Oscillators

Mechanical oscillators have long provided a highly versatile tool for probing the properties of quantum fluids. In previous experiments involving superfluids, mechanical oscillators have been used as probes of temperature [26], superfluid density [13] and viscosity [27]. They have been used to create [28–31] and detect [32] quantum turbulence, study acoustic emission [33–35], cavitation [36, 37], Andreev scattering [38–40], second sound attenuation [41], NMR excitation [42], study pairing configurations in differing ^{3}He phases[43, 44] and even as pixels in a ^{3}He quasiparticle camera [45, 46]. Outside of helium physics, mechanical oscillators are routinely used as sensors of viscosity in a wide variety of applications such as the automotive [47], and oil industry [48].

The most utilised mechanical oscillator for superfluid research is the vibrating wire, consisting of a superconductor a few millimeters of length in a 'goalpost' configuration [49]. Experiments have also demonstrated the use of large floppy wires [50], grids [51], and spheres [52]. Recently, experiments have pushed towards smaller and more sensitive probes, involving devices such as micro-TFs [33] and comb-drive electrostatic micro-electro-mechanical systems (MEMS) [53–55]. Quartz TFs are extremely sensitive probes, with particularly widespread use in scanning probe microscopy [56–58]. (NEMS), a class of mechanical objects with dimensions below the $1\,\mu$m length scale, present the next logical step in the quest towards increasingly more sensitive probes [59–62].

The development of NEMS is driven by advancement in fabrication technology allowing mechanical devices to push towards sub-micron scales. Nanomechanical devices typically require the use of electron-beam lithography, which presents a limitation to the scalability of device fabrication. NEMS have already found use in a range of applications, such as such as atomic force microscopy [63] and nanofluidics [64], due to their extremely high mass and force sensitivity [65–67] however their scientific potential remains relatively unexplored. Several recent experiments are beginning to implement such devices into experiments involving superfluids [68–72]. This body of work aims to demonstrate the use of NEMS as precise, versatile probes for current and future low-temperature work.

NEMS have two unique motivations aside from increase in sensitivity. Firstly, they offer a chance to explore regimes where the device dimensions are comparable to the coherence length of a quantum fluid, approximately 80 nm in ^{3}He. Such regimes have never been investigated before with a mechanical device and the physics of such a system are as yet unknown. Secondly, there is the possibility of cooling high frequency NEMS into their quantum ground state due to the very low temperatures achievable by cooling ^{3}He with nuclear demagnetisation of copper. The superfluid ^{3}He would be well thermalised with the nanobeams allowing 'brute force' cooling [73–75]. This would allow a bulk system can be studied in the limit where it is governed by quantum mechanics.

Low frequency torsional oscillators have also had significant importance for superfluid research historically, with a system of torsional discs providing the first accurate measurements of the normal-fluid fraction below the λ-point, as previously discussed [13]. Torsional TFs, in which the prongs rotate in opposing directions, have yet to find significant implementation in scientific research despite their novel mechanical properties. Torsional TFs provide an opportunity to extend torsional oscillator research towards the high-kilohertz range, unlocking a new frequency regime for superfluid research.

Here we will cover the theory of operation for oscillator probes, starting from the theory of resonance for simple harmonic oscillators. We will describe the expected motion and the various oscillatory modes with particular focus on the impacts of damping on the system. This will be derived for both nanomechanical beams, and TFs. In addition, we will discuss the impact of the surrounding media and measurement circuit on the operation of the probe. We will introduce the effects of high drives on operation, and the non-linear effects that result. In this way we can introduce the theory of nanobeam, and TF operation as a measurement probe for superfluid ^{4}He. Through measurement of the electrical response of the system, we can infer the damping within the system. Through careful treatment of the various dissipation mechanisms we can use this information to measure the properties of the surrounding media.

3.1 Damped, Driven Oscillators

In general, the motion of a damped, driven oscillator with displacement, x, can be described using the differential equation

$$m\frac{d^2x}{dt^2} + \delta\frac{dx}{dt} + kx = F(t), \tag{3.1}$$

where m is the mass, δ is a constant related to the damping, k is the spring constant and $F(t) = F_0 e^{i\omega t}$ is the periodic driving force. The stated equation remains valid in the case that the amplitude of displacement remains small comparable the geometry of the system, such that k can be considered approximately constant. To solve this, we introduce the trial solution $\dot{x} = \dot{x}_{max} e^{i\omega t}$ where $\dot{x}_{max}$ is the maximum amplitude of the velocity. In this way we obtain the familiar Lorentzian solution for the velocity,

$$\dot{x} = \frac{F_0 i\omega}{-\omega^2 m + i\omega\delta + k}. \tag{3.2}$$

This expression can be split into its real and imaginary components which can be resolved in experiments

$$Re(\dot{x}) = \frac{F_0\omega^2\delta}{\omega^2\delta^2 + (\omega^2 m - k)^2}, \tag{3.3}$$

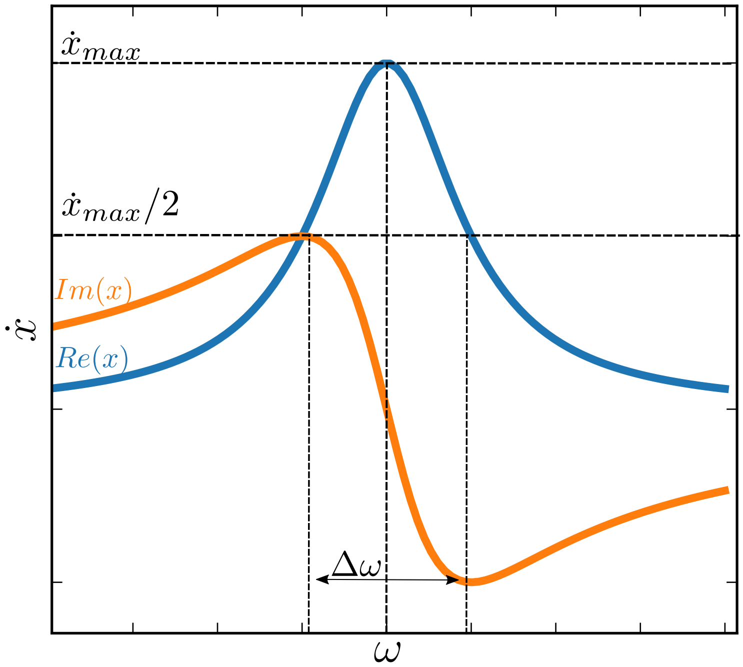

Fig. 3.1 Lorentzian function for a resonator, showing the magnitude of the real and imaginary components of the signal, given by Eq. (3.3) and Eq. (3.4). The full-width half maximum (FWHM) is indicated by $\Delta\omega$, along with the method of determining this.

$$Im(\dot{x}) = \frac{F_0\omega(k-\omega^2 m)}{\omega^2\delta^2 + (\omega^2 m - k)^2}, \tag{3.4}$$

in which we denote the central frequency by ω_0, otherwise known as the resonant or natural frequency of the oscillator, where ω_0 is given by

$$\omega_0 = \sqrt{\frac{k}{m}}, \tag{3.5}$$

The frequency dependence of the two components, given by Eq. (3.3) and Eq. (3.4), are shown in Fig. 3.1. Since our experiments typically rely on electrical measurements, we plot the velocity, $\dot{x}$, as this is proportional to the measured signal, which we will show in Sec. 3.2.

Importantly, the quantity $\Delta\omega$ can now be defined in terms of the damping constant δ as

$$\Delta\omega = \frac{\delta}{2\pi m}. \tag{3.6}$$

The various origins of the damping term for both nanomechanical devices, and TFs will be discussed in Sec. 3.4.

3.1.1 Duffing Oscillators

When the amplitude of oscillation becomes large it becomes important to consider the effects of non-linear terms in the differential equation. As is typically the case for nanoscale resonators, this additional term takes a cubic form and such devices are described as

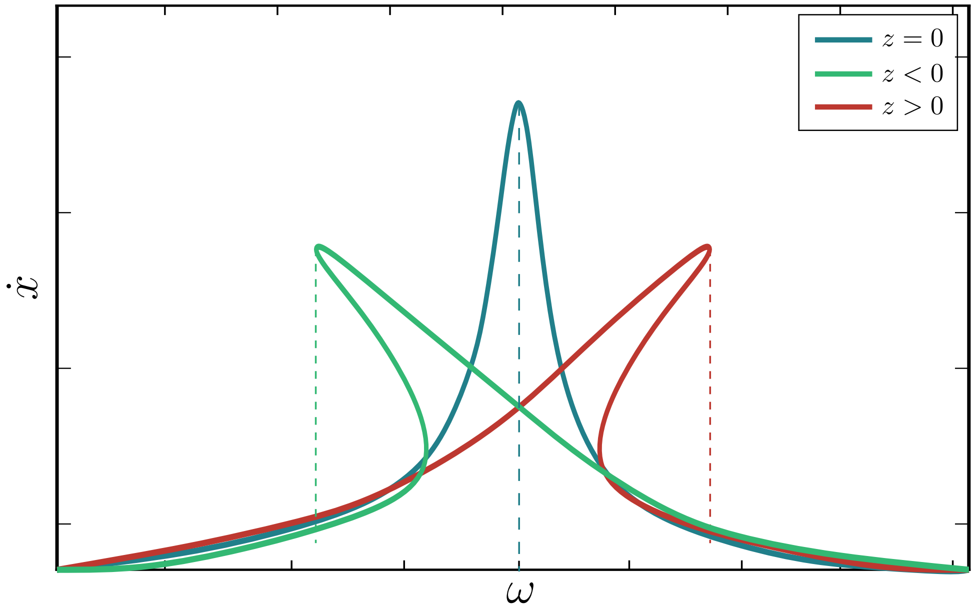

Fig. 3.2 Numerical solutions for the frequency response of three resonators with varying non-linear term, z. Resonators with $z > 0$ are known as hardeners, whereas those with $z < 0$ are known as softeners.

Duffing oscillators. A quadratic non-linearity would result in a force parallel to the displacement, which is considered non-physical and therefore neglected. The onset of these non-linear effects tends to decrease with the device dimensions, posing a limit on the dynamic range of such nanoscale oscillators [76]. The Duffing equation is given by [77]

$$m\frac{d^2x}{dt^2} + \delta\frac{dx}{dt} + kx + zx^3 = F, \tag{3.7}$$

where z gives the magnitude of the Duffing term. Systems where z is positive and negative are known as hardeners and softeners respectively due to the influence this term has on the effective spring constant of the system. The damped, driven Duffing equation is not exactly solvable analytically however it has some simplified numerical solutions. Importantly, frequency-space solutions to the Duffing equation enter a period of bi-stability close to the resonance frequency, in which there are multiple solutions for a single value of ω. For real systems this is resolved by sharp jumps between the stable solutions at different points in the frequency sweep, as well as hysteresis with respect to sweep-direction, behaviours that are difficult to mathematically model. Numerical solutions to the Duffing equation for different values of z are shown in Fig. 3.2.

Given the difficulty in exactly characterising this behaviour, we try to operate probes in a regime were the Duffing term is negligible. This is known as the ‘linear’ regime and measurements are typically performed here.

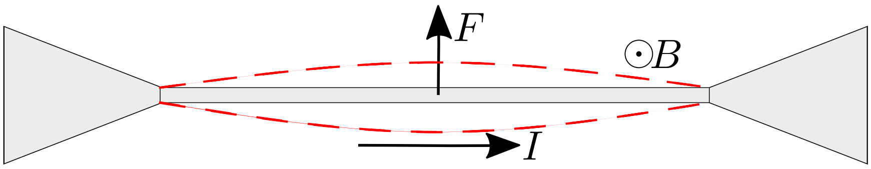

Fig. 3.3 Schematic diagram of the magnetomotive actuation scheme for a nanomechanical beam. An oscillating current in a constant magnetic field creates a force which is mutually perpendicular to both. The beam motion in the field generates a back-emf which is detectable by the circuit.

3.2 Nanomechanical Beams

The presented equations hold true for any oscillating structure where the restoring force is proportional to the displacement, modelling the objects as a point mass. The real geometry of the devices presented in this section are that of doubly-clamped beams, in which a suspended structure is held between two electrodes and allowed to oscillate freely. The devices were driven using a magnetomotive driving scheme [78], in which an external magnetic field and oscillating current of the form $I = I_0 e^{i\omega t}$ are used to induce a Lorentz force within the wire. The resultant force is mutually perpendicular to both the magnetic field and the driving current, and given by $\mathbf{F} = \mathbf{I} \times \mathbf{B}$. This type of geometry and driving method is shown schematically in Fig. 3.3.

When the nanobeam moves inside the magnetic field, a voltage is induced between the electrodes according to Faraday's law. This is known as the 'back-emf' and forms the key principle of our detection scheme. The magnitude of this emf is given by

$$V = \frac{d(B \cdot A)}{dt}, \tag{3.8}$$

where A is the area traversed by the conductor in the magnetic field, approximated to be Lx where L is the length of the nanobeam. In this way, the voltage drop across the nanobeam can be written as

$$V = BL\dot{x}. \tag{3.9}$$

The magnetomotive actuation scheme has significant implications for the sensitivity of the system, which will be discussed further in Sec. 3.4.3.

3.2.1 Euler-Bernoulli Beam Theory

The previous section described beam mechanics in the framework of a simple harmonic oscillator with resonant frequency ω_0, which depends only on a spring constant, k, and the mass, m. In reality, the spring constant, k, is not known for a given oscillator, and therefore the resonant frequency cannot be predicted using such a model. We will now discuss the dynamics of real beam motion in the framework of Euler-Bernoulli beam theory, and arrive at an expression for the resonance frequency in terms of known dimensions. In the absence of an external drive, the differential equation describing the motion for the flexural mode on such a beam is given by [79]

$$EI\frac{\partial^4 x}{\partial l^4} - T_0\frac{\partial^2 x}{\partial l^2} + \rho A\frac{\partial^2 x}{\partial t^2} = 0, \tag{3.10}$$

where E is the Young modulus, I is the moment of inertia, T_0 is the internal tension, ρ is the beam density and A is the cross sectional area. As previously, x is the deflection from the rest position, and l is the position along the beam. The devices described here, being clamped at both ends, impose the following boundary condition on the system:

$$x(0,t) = x(L,t) = \frac{\partial x}{\partial l}(0,t) = \frac{\partial x}{\partial l}(L,t) = 0. \tag{3.11}$$

The general solution to the differential equation is given by

$$x(l,t) = \sum_n u_0 g_n(l) e^{i(\omega_0 t + \phi_n)} = \sum_n u_n(t) g_n(l), \tag{3.12}$$

where n is the mode number, and $g_n(l)$ us the spatial function of the n^{th} mode. The differential equation can now be solved for two limits: where $EI > T_0$, known as the string limit, and where $EI < T_0$, known as the bending limit. For the string limit, the resonant frequency is determined by the tension, and the rigidity can be neglected. The displacement profile is given by

$$g_n(l) = u_n \sin\left(\sqrt{\frac{\rho A}{T_0}}\omega_n l\right), \tag{3.13}$$

yielding the resonance frequency of the nth harmonic to be

$$\omega_n = \frac{n\pi}{L}\sqrt{\frac{T_0}{\rho A}}. \tag{3.14}$$

Importantly, we note that in this limit the harmonics are integer multiples of the fundamental frequency.

The bending limit, in which the rigidity dominates and we can neglect the tensile term, we arrive at a fourth-order differential equation. The general solution to this equation has the form

$$g_n(l) = C_1\sin(\beta_n l) + C_2\cos(\beta_n l) + C_3\sinh(\beta_n l) + C_4\cosh(\beta_n l), \tag{3.15}$$

where C_1, C_2, C_3, C_4 are constants, and

$$\beta_n = \left(\frac{\rho A}{EI}\right)^{1/4}\sqrt{\omega_n}. \tag{3.16}$$

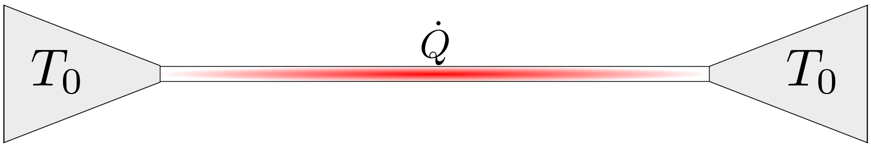

Fig. 3.4 Schematic showing a nanobeam undergoing constant thermal flux, $\dot{Q}$, coupled to two thermal baths at temperature, T_0, in the electrodes. This scheme can be used to calculated the temperature distribution across the beam.

Again, using the previously discussed boundary condition, and solving numerically the expression for the n^{th} harmonic to be

$$\omega_n = \left(\frac{\gamma_n}{L}\right)^2 \sqrt{\frac{EI}{\rho A}}, \tag{3.17}$$

where $\gamma_n = 4.73, 7.85, 10.99, 14.14$ for $n = 1, 2, 3, 4$. In reality, beam dynamics lie somewhere between these two limits. The situation here becomes rather complicated due to the tension dependence of the spring constant. The general solution to the full equation has the form

$$g_n(l) = C_1 \sinh(k_1 \frac{l}{L}) + C_2 \cosh(k_1 \frac{l}{L}) + C_3 \sin(k_2 \frac{l}{L}) + C_4 \cos(k_2 \frac{l}{L}), \tag{3.18}$$

where

$$k_{1,2} = \sqrt{\pm \frac{T_0 L^2}{2EI} + \sqrt{\left(\frac{T_0 L^2}{2EI}\right)^2 + \omega^2 L^2 \sqrt{\frac{\rho A}{EI}}}}. \tag{3.19}$$

Substituting the boundary condition yields an excellent approximation to the mode frequencies observed experimentally:

$$f_n = \frac{\pi}{8}(2n+1)^2 \frac{1}{L^2} \sqrt{\frac{EI}{\rho A}} \sqrt{1 + \frac{0.97 T_0 L^2}{(n+1)^2 \pi^2 EI}}. \tag{3.20}$$

We will use this expression to obtain estimates for the frequency of real nanomechanical devices, as well as to estimate the tension for a measured device.

3.2.2 Thermalisation of Nanomechanical Beams

When the nanobeam is driven using an oscillating current of magnitude, I, we expect the temperature of the sample to increase above that of the thermal bath.

Here we will estimate the magnitude of this rise by solving the heat equation under the boundary conditions of electrodes held at a fixed temperature. Here, we equate the uniform heat input with the heat flowing to the electrodes in the steady state (i.e $\partial T/\partial t = 0$), as shown schematically in Fig. 3.4. Beginning from the heat equation [80]

$$\nabla \cdot J = \dot{Q}, \tag{3.21}$$

where $J = \kappa \nabla T$ is the heat flux, in which κ is the thermal conductivity and $\dot{Q} = I^2 R$ is the heat input to the system. Using the Wiedermann Franz law ($\kappa = \sigma L_0 T$) the thermal conductivity can be written in terms of the conductivity, σ. Hence, in 1D:

$$\frac{\partial}{\partial x}(L_0 \sigma T \frac{\partial T}{\partial x}) = \dot{Q}, \tag{3.22}$$

where $L_0 = 2.45 \times 10^{-8}\,\mathrm{W\,\Omega\,K^{-2}}$. Integrating twice yields the expression for the temperature, given by

$$T = \sqrt{\frac{1}{L_0 \sigma}(\dot{Q}x^2 + \alpha x) + \beta}, \tag{3.23}$$

in which α and β are constant of integration. Using the boundary condition ($T(x = 0) = T_0$ and $T(x = l) = T_0$) we find that

$$T = \sqrt{\frac{\dot{Q}x}{L_0 \sigma}(l - x) + T_0^2}. \tag{3.24}$$

From this, the maximum temperature, at $x = l/2$ is given by

$$T_{\mathrm{max}} = \sqrt{\frac{\dot{Q}l^2}{4L_0 \sigma} + T_0^2}. \tag{3.25}$$

We see that for large values of $\dot{Q}$, the peak nanobeam temperature can be raised far above the electrode temperature. In Sec. 3.4, we will see that device temperature can significantly affect the device damping.

3.3 Tuning Forks

Here, we will discuss the equations which relate to the specific geometry of tuning forks (TFs). TFs are mechanical oscillators formed by two prongs (tines) formed into a U-shape such that the tines can oscillate freely. The use of quartz in TFs provides the ability of electrical driving and readout, due to its piezoelectric properties. Quartz TFs are driven by providing an alternating voltage, $V = V_0 e^{i\omega t}$, to metal electrodes on the surface of the quartz. This provides an alternating force, F, capable of driving the electrodes into motion. TFs are capable of supporting multiple oscillation modes: flexural, where the tines move inwards and outwards in antiphase, torsional, where the tines twist about their centre-of-mass, and shear, where the legs move inwards and outwards in phase with each other. Oscillatory modes on TFs generally consist of the fundamental, higher harmonics, or mixed states of the stated modes. Quartz TFs are used as frequency standards in watches, as well as force sensors in scanning optical microscopes. Quartz TFs are relatively cheap, easy to implement, do not require a magnetic field and operate in a wide frequency range. They also have very low intrinsic damping, discussed further in Sec. 3.4, making them very sensitive probes. For this reason, they have become a frequently used tool in low-temperature research. A schematic with a typical measurement scheme for a quartz TF is shown in Fig. 3.5.

Considering first the flexural oscillatory mode, the force on the TF can be calculated from purely geometrical considerations as

$$F = \frac{a_F V}{2}, \tag{3.26}$$

where we define a_F as the 'fork constant'. The fork constant is a TF specific transduction factor since it allows the conversion between electrical signals and mechanical motion. For this reason a_F is an essential parameter to be calculated for a TF acting as a probe. By equating the work done per unit time, $(F\dot{x})$, with the power supplied per unit time IV, it is clear that the fork constant also allows us to determine the velocity from the current flowing

$$I = a_F \dot{x}. \tag{3.27}$$

Geometrically, the fork constant for the flexural mode is given by [81]

$$a_F = d_{11} E \frac{TW}{L}, \tag{3.28}$$

where d_{11} is the piezoelectric modulus of quartz in the appropriate plane, T, W and L are the thickness, width and length of the fork tines respectively. Experimentally, the fork constant can be determined in terms of the Lorentzian parameters, provided the drive voltage is known, and is given by [26]

$$a_F = \sqrt{\frac{4\pi m_{\text{eff}} \Delta f I}{V}}, \tag{3.29}$$

where m_{eff} is the effective mass for the fork and Δf is the width of the Lorentzian curve. The effective mass accounts for the fact that the entire tine does not move when undergoing oscillation. I and V are the current and voltage at the maxima of the Lorentzian curve.

The motion of the torsional TF can be described by the equation of motion for a torsional oscillator [26]. From the differential equation for a driven torsional oscillator

$$\frac{d^2\phi}{dt^2} + \gamma \frac{d\phi}{dt} + \frac{G}{I_0} = \frac{\tau}{I_0}, \tag{3.30}$$

where ϕ is the angle of rotation, γ is the drag torque, G is the shear modulus, I_0 is the moment of inertia and τ is the torque. Through use of the trial solution $\phi = \phi_0 e^{i\omega t}$ one arrives at the expression for the resonant frequency, ω, in terms of the moment of inertia

$$\omega = \sqrt{\frac{\mu}{I_0}} = \sqrt{\frac{GJ}{LI_0}}, \tag{3.31}$$

where μ is the spring constant, J is the torsional constant and L is the length of the prong. J can be determined from geometrical considerations and is calculated using [81]

$$J = WT^3\beta, \tag{3.32}$$

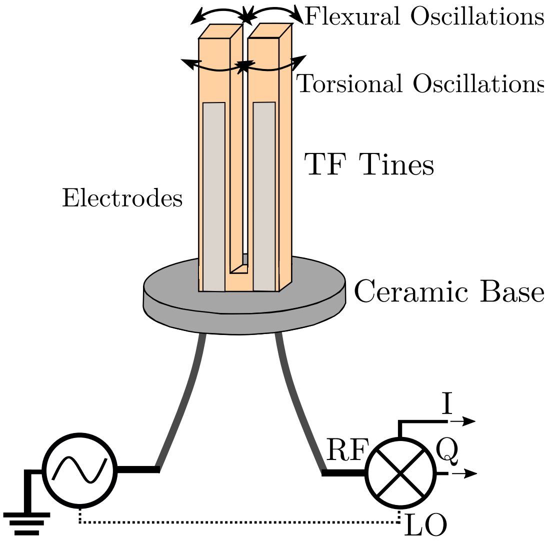

Fig. 3.5 Schematic of a typical TF package with the tines and base indicated. A typical measurement scheme is shown, where an AC voltage is applied to one electrode, and the response measured at the same frequency using demodulation - typically in the form of a lock-in amplifier.

where $\beta = 0.2$ is a constant yielding the first oscillation mode.

The torsional fork constant, a_T, can be equivalently defined for torsional motion such that the torque, τ is given by

$$\tau = \frac{a_T V}{2}, \tag{3.33}$$

The work done per unit time is now $\sim \tau\omega_T$, where ω_T is now the angular velocity, with the power applied to the fork ($\sim IV$). The measured current, I, is hence

$$I = a_T \omega_T. \tag{3.34}$$

No equivalent analytical expression to Eq. (3.28) is known for torsional oscillatory modes, hence it must be extracted by experimental means.

3.4 Dissipation in Oscillating Structures

Here we will outline the various mechanisms which contribute to the dissipation experienced by oscillating structures. By this, we mean any process which results in energy loss from the oscillator. Careful study of these mechanisms allows us to isolate dissipation due to the environment being studied, from dissipation inherent to the measurement system. In this way, oscillators can act as probes for the surrounding media. We can quantify dissipation via the quality factor $Q = \omega_0/\Delta\omega$ where ω_0 is the resonant frequency and $\Delta\omega$ is the FWHM. Hence, we can quantify the overall energy loss as a sum of the various dissipation mechanisms:

$$Q_{\text{tot}}^{-1} = Q_1^{-1} + Q_2^{-1} + Q_3^{-1} \cdots , \tag{3.35}$$

where $Q_1^{-1}, Q_2^{-1}, Q_3^{-1}$ refer to the various loss mechanisms to be outlined in the relevant sections. Damping mechanisms can be divided into two categories: intrinsic and extrinsic. As the name suggests, intrinsic damping mechanisms are internal to the device and not caused by any surrounding media or measurement. This may involve interactions between electrons, phonons and other impurities leading to dissipation. Here we will describe thermoelastic and clamping losses, as well as the role of material tunnelling two-level systems (TLS) in dissipation. For our purposes, intrinsic losses are regarded as unavoidable and present an absolute limit to the sensitivity of a given mechanical probe. Extrinsic damping mechanisms are losses that originate externally to the device itself, and may be a result of the measurement circuit, or that of the surround media. We will discuss magnetomotive damping losses in Sec. 3.4.3, and damping due the surrounding media, namely superfluid ^{4}He, in Sec. 3.5.

3.4.1 Clamping Losses

For most oscillating devices, the performance is ultimately limited by the clamping losses. Clamping losses occur due to acoustic energy propagating into the device substrate. Typically, clamping losses occurs through the device electrodes, as a result of internal acoustic waves being reflected back at the oscillator boundary. Previous work has shown that for an oscillating beam, the dissipation follows [82]

$$Q_{\mathrm{cl}}^{-1} = \frac{Ah^4}{L^5}, \tag{3.36}$$

where h and L are the height and length of the beam respectively, and A is a geometrical constant. In this way, for nanoscale devices with an extremely high aspect ratio we expect this term to become important at low temperatures. Clamping losses are expected to have no significant temperature dependence, and therefore provide an ultimate limitation on the Q-Factor of high frequency devices operating at low temperatures.

3.4.2 Thermoelastic Effect

Thermoelastic effects constitute a large part of the damping while operating at higher temperatures. Here, mechanical vibrations induce local temperature gradients requiring heat flow, resulting to energy dissipation, to equalise the temperature. Given the temperature dependence of this process we do not observe significant damping due to this effect in low-temperature work. Quantitatively, the damping due to thermoelastic effects for a nanobeam is given by [83]

$$Q_{\mathrm{Th}}^{-1} = \frac{AE\alpha^2 T}{C_p}, \tag{3.37}$$

where E is the Young's modulus, α is the thermal expansion coefficient, C_p is the heat capacity and A is a constant of the order unity.

3.4.3 Magnetomotive Damping

Magnetomotive damping affects structures which are driven using an external magnetic field, such as a nanobeam. In the low-temperature limit, the damping within the nanobeams is highly dependent on the magnitude of the magnetic field. Magnetomotive damping is a result of coherent motion of the beam leading to a back-emf. An emf will generate a corresponding current, which results in a force which always opposes the motion of the nanobeam. Such an effect can also be thought of in terms of magnetisation of the conducting material in an external magnetic field, which again generates an opposing force. For a wire moving with velocity, v, in an external circuit, the magnitude of the back-emf is given by $\epsilon = vBl$. Importantly, the size of the back-current generated by this emf depends on the impedance of the external circuit, Z_0. The 'back-current' generated is given by

$$I = \frac{\epsilon}{Z_0} = \frac{vBl}{Z_0}. \tag{3.38}$$

In reality, the total current will be a sum of the driving current and the back-current. By Lenz's law, the back-current will generate a force, F, which opposes that of the driving force:

$$F = IlB = \frac{vB^2l^2}{Z_0}. \tag{3.39}$$

Hence, the losses can be written in terms of the energy lost per cycle as a result of this opposing force as

$$Q_{\mathrm{mm}}^{-1} = \frac{1}{2\pi m f_0}\frac{dF}{dv} = \frac{B^2l^2}{2\pi m f_0}\frac{1}{|Z_0|}, \tag{3.40}$$

demonstrating the characteristic B^2 dependence. Our result implies that the damping in the circuit can be tuned by the external magnetic field. As discussed in Sec. 3.2, larger magnetic fields increase the size of our received signal, increasing the signal-to-noise ratio. Magnetic field can therefore be used as a tuning parameter, high when the system damping is high and low when the system damping is low, in order to maintain a regime where system damping is always larger than the magnetomotive damping.

3.5 Dissipation for Oscillating Structures in Superfluid ^{4}He

This section aims to quantify the various damping mechanisms present in ^{4}He for oscillators at low temperatures, such that they can be used as probes. Submerged in liquid ^{4}He, there are two key temperature regimes, over which the damping varies significantly. In the hydrodynamic regime the mean free path of the excitations is much less than that of the beam dimensions ($l_m \ll a$) such that collisions occur often and the helium exhibits macroscopic fluid dynamics. At lower temperatures, ^{4}He enters a ballistic regime whereby the mean free path is much greater than that of the beam radius ($l_m \gg a$). Here, we neglect the effects of inter-particle collisions since these events are rare, and the superfluid behaves like a weakly interacting gas of thermal excitations. The mean free path for both phonons and rotons is shown in Fig. 3.6, compared with typical nanobeam dimensions shown as the dashed black line. Acoustics also play a role in the

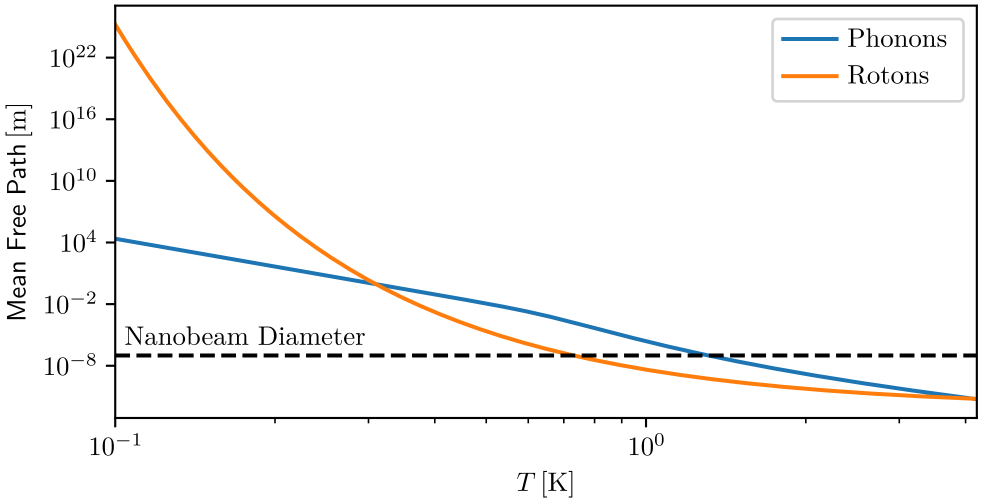

Fig. 3.6 Mean free path of phonons and rotons in liquid ^{4}He from 4.2 K to 100 mK. A typical nanobeam dimension is shown by the dashed black line. The mean free path of both quasiparticles exceeds the nanobeam dimension at ~ 0.7 K. By 100 mK the roton mean free path is comparable the observable universe. Adapted from [84].

damping, often limiting the performance of probes at the lowest temperatures. We will treat the effects of these regimes in the following sections, demonstrating the impact of different superfluid regimes on the damping experienced in nanobeams.

3.5.1 Hydrodynamic Regime

Here we consider the effect of a nanobeam operating in a viscous fluid where damping in dominated by Stokes' drag. Modelling the behavior of a beam moving in the hydrodynamic regime we utilise a theory adapted by Blaauwgeers *et. al.* [26]. We substitute the beam mass with an effective mass, m_H, which includes two additional terms: one term for the clamped fluid mass and one related to the backflow of the fluid due to displacement. An altered effective mass leads to a change in the oscillator frequency. The frequencies in vacuum and helium, f_0 and f_H, of a simple-harmonic oscillator with spring constant k are given by

$$f_0 = \frac{1}{2\pi}\sqrt{\frac{k}{m_0}}, \qquad f_H = \frac{1}{2\pi}\sqrt{\frac{k}{m_H}}, \tag{3.41}$$

where the effective mass of the oscillator in ^{4}He is given by

$$m_H = m_0 + \underbrace{A\rho_H V}_{\text{Backflow}} + \underbrace{B\rho_n S\delta}_{\text{Clamped fluid}}, \tag{3.42}$$

where ρ_H is the density of the fluid, V and S are the beam volume and surface area. A and B are fitting parameters typically close to unity and δ is the viscous penetration depth of the fluid given by

$$\delta = \sqrt{\frac{\eta}{\pi\rho_n f_H}}. \tag{3.43}$$

where η is the viscosity of the normal-fluid. Combining Eq. (3.41) and Eq. (3.42) yields the frequency shift as a function of the normal-fluid fraction,

$$\left(\frac{f_0}{f_H}\right)^2 = 1 + \frac{AV\rho_H}{m_0} + \frac{BS}{m_0}\sqrt{\frac{\eta\rho_n}{\pi f_H}}. \tag{3.44}$$

The temperature dependence arises from the rapidly changing normal-fluid fraction in the vicinity of T_λ. Below $\sim 1\,\mathrm{K}$ no significant frequency change is observed due to the vanishingly small value of ρ_n.

To model the damping on a nanobeam in helium we consider the hydrodynamic effects of the normal fluid fraction. The superfluid component does not contribute to the device damping. The Stokes' drag force for an infinitely long cylinder in the high frequency limit is given by [85]

$$F = CS\sqrt{\pi\rho_n\eta f_H}v, \tag{3.45}$$

where C is a geometrical constant, f_H, is the oscillation frequency and v is the oscillation velocity. Although our structures have finite size, the velocity at the boundaries is zero and we can therefore ignore edge effects [86]. Hence, the damping due to the fluid is given by

$$Q_{\mathrm{hy}}^{-1} = \frac{1}{2\pi m_0 f}\frac{dF}{dv} = \frac{CS}{2m_0}\sqrt{\frac{\rho\eta f_H}{\pi}}\left(\frac{f_0}{f_H}\right)^2. \tag{3.46}$$

The model has had success in describing the damping of large vibrating structures in the temperature range 4.2 K to 1 K [26, 33]. Below 1 K the mean free path of the quasiparticles becomes large, meaning interactions between quasiparticles become infrequent. In this limit, the viscosity and viscous penetration depth are not well defined. It does however have its limitations when describing the behaviour of systems where the viscous penetration depth, δ, becomes much larger than the device dimensions. In this case, the volume of displaced fluid becomes dependent on the volume of clamped fluid, typically above T_λ where the $\rho_n/\rho = 1$. For this reason, this model struggles to accurately describe the damping experienced by nanobeams in ^{4}He above T_λ due to the large volume of clamped fluid relative to the oscillator size. The model is shown schematically in Fig. 3.7(a) with the limiting case shown in Fig. 3.7(b). Although our focus has been on quantum fluids, the described model is equally valid in classical fluids such as ^{4}He-I, when ρ_n is replaced with the total density, as has been previously demonstrated [26].

3.5.2 Ballistic Regime

Here we discuss damping in superfluid ^{4}He where the mean free path of the quasiparticles exceeds that of the beam dimensions. This mechanism of damping typically dominates below 1 K, until a temperature independence mechanism takes over. Phonons and rotons are the thermal excitations of superfluid ^{4}He, introduced in Sec. 2.2.

We treat the contribution of individual quasiparticle collisions with the nanobeam to the overall damping. We will derive the general form for a distribution of particles

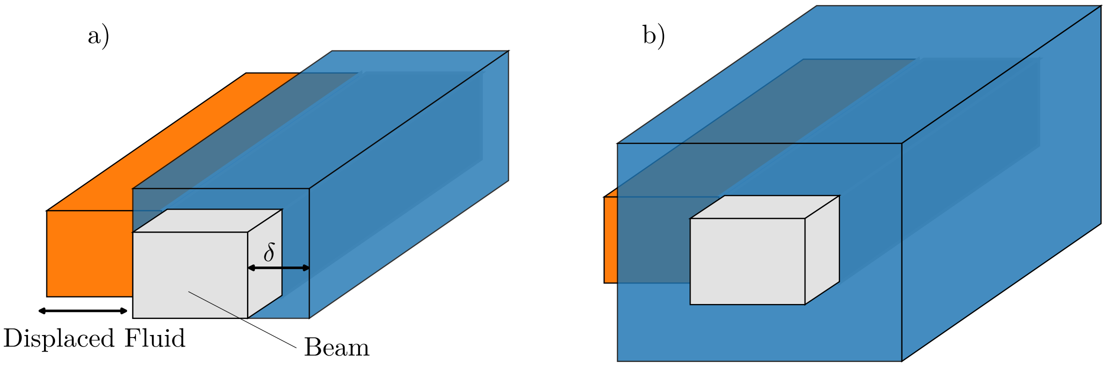

Fig. 3.7 (a) Diagram of hydrodynamic clamping to a nanomechanical beam at relatively low temperature ($< 2\,\mathrm{K}$). The clamped component is small compared to the size of the beam. (b) Hydrodynamic clamping close to T_λ. The clamped component is theoretically very large compared to the beam, and will therefore have an influence on the volume of displaced fluid. In this regime the proposed model does not fit the experiments well, since we originally assume the two components are separate.

colliding with the beam, and then finally specify the exact forms for phonons and rotons. The total momentum of quasiparticles colliding with a beam moving at velocity, v, per unit time, is given by [84]

$$F = \frac{dp}{dt} = AaLp_0n((v_F - v) - (v_F + v)) = -Anp_0vaL, \tag{3.47}$$

where a is the radius of the cylinder, L is the length and v_F is the velocity of the fluid. p_0 is the momentum of each quasiparticle and n is the number density. Here, the geometrical constant $A = 2.67$ for a cylindrical geometry [84]. For phonons, this can be rewritten in terms of the mass density of phonons such that $\rho = nm^*$. In addition, we can substitute momentum in terms of $p_0 = m^*c_{\mathrm{ph}}$ where c_{ph} is quasiparticle velocity. This yields the expression for the drag force

$$F = -Ac_{\mathrm{ph}}\rho_{\mathrm{ph}}vaL. \tag{3.48}$$

Should the cylinder move with oscillatory motion, the magnitude of the phonon damping is given by

$$Q_{\mathrm{ph}}^{-1} = \frac{1}{2\pi mf}\frac{dF}{dv} = \frac{-Ac_{\mathrm{ph}}}{2\pi^2 a\rho_\omega}\rho_{\mathrm{ph}}, \tag{3.49}$$

where the cylinder mass is given by $m = \pi\rho_\omega a^2L$. Substituting Eq. (2.30) yields the damping due to phonons given by

$$Q_{\mathrm{ph}}^{-1} = \frac{Ak_{\mathrm{B}}^4}{45f_0\hbar^3c_{\mathrm{ph}}^4a(\rho_\omega + \rho_s)}T^4. \tag{3.50}$$

The damping due to rotons is given by equating Eq. (3.47) with the definition for the Q factor as

$$Q_{\mathrm{ro}}^{-1} = \frac{1}{2\pi mf}\frac{dF}{dv} = \frac{-Ap_0}{2\pi^2 a\rho_\omega}n_{\mathrm{ro}}. \tag{3.51}$$

By substituting Eq. (2.33), the roton contribution to damping is given by

$$Q_{\mathrm{ro}}^{-1} = \frac{Ap_0}{2\pi^2 a f_0 \rho_w} \left(\frac{m^* k_{\mathrm{B}} T}{2\pi\hbar^2} \right)^{3/2} \exp\left(-\frac{\Delta}{k_{\mathrm{B}} T} \right). \tag{3.52}$$

Since the above is a microscopic theory, derived directly using Bose-Einstein statistics, these equations remain valid to arbitrarily low temperatures. In practice, measurements become limited by some additional form of damping, commonly due to acoustic emission for high-frequency devices [33].

3.5.3 Acoustic Dipole Emission

In devices with high oscillation frequencies, the effects of acoustic emission become prevalent, often dominating the damping at the lowest temperatures. Nanobeam act as dipole acoustic emitters when oscillating in a compressible media. The emission of pressure waves in superfluid ^{4}He (also known as first sound) obeys largely the same physics as classical media provided the oscillation amplitude remains small, and the temperature is low enough such that second sound corrections can be ignored, as discussed in Sec. 2.1.1.

By taking a far-field approximation, and assuming the wavelength is larger than the dipole spacing, the energy emitted per unit time for an infinitely long cylinder is given by [85]

$$P = \frac{\pi^2}{4c_{\mathrm{ph}}^2} \rho_H \omega^3 a^4 L |\mathbf{v}|^2, \tag{3.53}$$

where c_{ph} is the velocity of sound in the fluid and v is the oscillation velocity, a and L are the radius and length of the beam respectively. From the definition of the Q-factor as the average energy dissipated per cycle we can interpret this emission in terms of device damping

$$Q_{\mathrm{ac}}^{-1} = \frac{\Delta\omega}{\omega} = \frac{P}{2\pi m |\mathbf{v}|^2} \frac{1}{\omega} = \frac{\pi^2 \rho_H a^4 L \omega^2}{2c_{\mathrm{ph}}^2 m}. \tag{3.54}$$

This can be rewritten in terms of the beam density by taking $m = \rho_\omega \pi a^2 L$ giving an expression that does not depend on the beam length. Substituting $f = \omega/2\pi$ gives

$$Q_{\mathrm{ac}}^{-1} = \frac{\pi^3 \rho_H a^2 f^2}{2c_{\mathrm{ph}}^2 \rho_\omega}. \tag{3.55}$$

The implications of this result is significant for the sensitivity of nanoscale devices for fluid measurements. When the acoustic term, Q_{ac}^{-1}, begins to dominate this presents an ultimate limit for the sensitivity of a detector. It is therefore important when considering device design, to maintain the ratio $a^2 f^2$ as low as reasonably possible.

3.5.4 Acoustic Quadrupole Emission

Due to the geometry of quartz TFs, the flexural mode acts as a quadrupole acoustic source. A TF can be modelled as an arrangement of four monopoles on either side of the

TF tine, with velocity field for a monopole acoustic source is given by

$$\Phi(r,t) = \frac{Be^{i(kr-\omega t)}}{4\pi r}, \tag{3.56}$$

where r is the distance from the monopole and B is the source strength and ω is the oscillation frequency. The total velocity field, incorporating spherical harmonic identities, is given by [35]

$$\Phi(r,\theta,t) = \frac{iBke^{-i\omega t}}{2\pi} \sum_{\substack{m=0 \\ \text{even}}}^{\infty} (2m+1) P_m(\cos\theta) h_m(kr)[j_m(kd_2) - j_m(kd_1)], \tag{3.57}$$

where $P_m(\cos\theta)$ are Legendre polynomials, $h_m(kr)$ and $j_m(kd)$ are the Hankel and Bessel functions. d_1 is the distance from the origin to the inner tine edge, and d_2 is the distance from the origin to the outer tine edge. The power emitted per unit time is given by

$$P = \frac{\rho_s W^2 L^2 |v|^2}{2\sqrt{2\pi d_1 d_2}} \sum_{\substack{m=0 \\ \text{even}}}^{\infty} (2m+1)[j_m(kd_2) - j_m(kd_1)]^2, \tag{3.58}$$

where W, T and L are the width, thickness and length of the fork, and $|v|^2$ is the fork velocity. The contribution to the damping in helium is [33]

$$Q_{\text{ac}}^{-1} = \frac{\Delta f}{f} = \frac{P}{2\pi m |\mathbf{v}|^2} \frac{1}{f} = 1.961\pi^4 \frac{(T+d_1)^2}{\rho_q^2} \frac{\rho_S}{c_{\text{ph}}^5} (\frac{f_H}{f_0})^2 m_{\text{eff}} f_H^5, \tag{3.59}$$

where f_0 and f_H are the vacuum and helium frequencies, ρ_q is the density of quartz, m_{eff} is the effective mass, and the outer tine distance has been substituted as $d_2 = d_1 + T$. There is clearly a strong power law for the damping as a function of the TF frequency. High frequency oscillation modes experience very high damping as a result of acoustic emission, and therefore care must be taken for quadrupole device to maintain low-frequencies.

3.5.5 Cavitation

Cavitation is the nucleation of gas bubbles inside a sample of bulk-liquid, as a result of a change of pressure inside the liquid, typically occurring far from the thermodynamic equilibrium [87]. Here, the liquid is said to be in a metastable state. Since cavitation is a non-equilibrium process it cannot be clearly represented as an additional damping term, however its effects become important when studying oscillating devices at high velocities. Cavitation can be understood by calculating the free energy of a spherical bubble with radius R inside the metastable liquid:

$$F(R) = 4\pi R\gamma - \frac{4}{4} R^3 \Delta G, \tag{3.60}$$

where γ is the surface tension of the liquid-gas interface, and ΔG is the difference in Gibbs free energy between the two phases [88]. By minimising the free energy we can obtain both the critical radius for cavitation

$$R_c = \frac{2\gamma}{\Delta G}, \tag{3.61}$$

and the energy barrier against nucleation

$$E_c = \frac{16\pi\gamma^3}{3(\Delta G)^2}. \tag{3.62}$$

TFs typically cause cavitation in superfluid ^{4}He at velocities exceeding $\sim 1\,\mathrm{m\,s^{-1}}$, as interpreted from sharp discontinuities electrical measurements [36, 37]. Cavitation in quantum fluids has never been explicitly observed using optical methods. Cavitation manifests itself as a breakdown of the resonance response at a critical velocity, v_{cav}, when measuring the resonance curve slowly. It is typically observed at finite overpressures on the liquid, with $v_{\mathrm{cav}} \propto \sqrt{\Delta p}$, where Δp is the pressure difference applied to the liquid sample. Cavitation has so far only been demonstrated using devices with relatively low resonance frequency ($f_0 < 32\,\mathrm{kHz}$), using only macroscopic objects. The behaviour of high-frequency, nanoscale objects under high drive in superfluid ^{4}He is unknown.

3.5.6 Quantum Turbulence

When excited to sufficient velocity, mechanical oscillators can dissipate energy in the form of quantised vortices. Quantum turbulence, as introduced in Sec. 2.3, is a particularly important dissipation mechanism for TFs due to their relatively low frequency and large size. In a quantum fluid, much like a classical fluid, there are two flow regimes defined by the Reynolds number [85]

$$\mathrm{Re} = \frac{\rho_N v L}{\mu}, \tag{3.63}$$

where ρ_N is the normal fluid density, v is the tip velocity of the fork relative to the fluid, and μ is the dynamic viscosity. For low Reynolds numbers ($\mathrm{Re} \ll 1$) we expect laminar flow and for high Reynolds numbers ($\mathrm{Re} \gg 1$) we have turbulent flow. Turbulent flow is not exactly solvable within the framework of the Navier-Stokes' model, however can be empirically represented by a drag coefficient, C_D, such that the drag force

$$F_T = -\frac{1}{2} C_D A \rho_H v^2, \tag{3.64}$$

where A is the cross-sectional area of the plane perpendicular to the flow. From this, the turbulent regime is characterized by a $v \propto \sqrt{F_T}$ relationship in the force-velocity characteristics of a device. Due to the extremely low viscosity of superfluid ^{4}He at low temperatures, the Reynolds number can be extremely high. Using Eq. (3.63) at a temperature of $1\,\mathrm{K}$, and length scale $10^{-2}\,\mathrm{m}$ the Reynolds number is $\sim 10^6$, a regime that is difficult to access in classical fluids on small length scales. For this reason, small mechanical oscillators are not generally used for turbulence experiments involving viscous classical fluids.

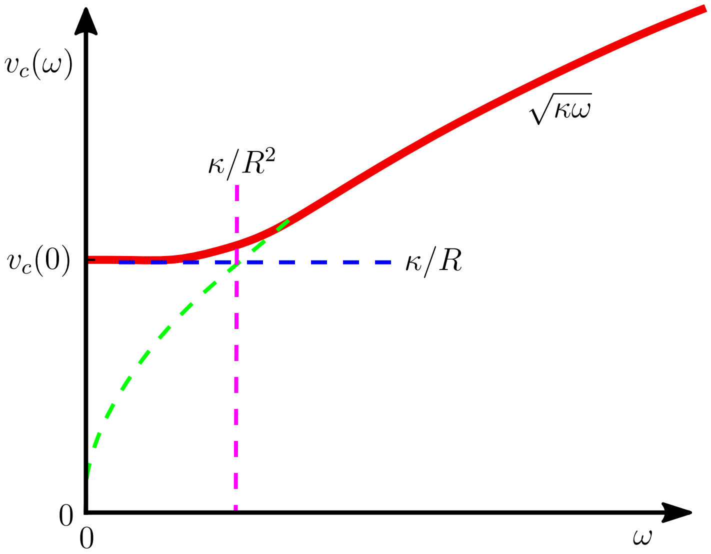

Fig. 3.8 Sketch of how the critical velocity of the onset of turbulence should behave for an object of radius R and frequency ω. $\kappa = \frac{h}{m_4}$ is the quanta of circulation. The frequency dependence is important since nanomechanical devices have high operation frequencies. Adapted from [92].

The crossover between the two flow regimes regimes occurs at a *critical velocity* given by [89]

$$v_c = \sqrt{\gamma\omega\kappa}, \tag{3.65}$$

where $\gamma \sim 1.7$ is a geometrical constant and $\kappa = h/m$ is the constant of circulation. This relationship, with the low frequency behaviour is shown in Fig. 3.8. The typical onset velocity is of the order of several $\mathrm{mm\,s^{-1}}$ [89–91] for vibrating wires, increasing to tens of $\mathrm{cm\,s^{-1}}$ for TFs. The additional damping in this regime is hence given by

$$Q_{\mathrm{T}}^{-1} = \frac{1}{4\pi m f_0} C_D A \rho_H v, \tag{3.66}$$

where m is the TF mass. Due to the velocity dependence of this damping term, as measured on a plot of driving-force against velocity, this term corresponds to a decrease in the slope. The similarities in the behaviour of quantum and classic turbulence suggest that studies of quantum vortices may contribute to improving our understanding of classical turbulence.

Due to the high frequency of oscillation and nanoscale dimension, we expect the dynamics of nanobeams nucleating quantized vortices to be highly unusual. From Fig. 3.8, we see that both the oscillation frequency and length scale play a role in determining the critical velocity for quantum turbulence production. For this reason, we might not expect to observe vortex production until velocities of the order of $\sim 1\,\mathrm{m\,s^{-1}}$, towards the limit in velocities attained by such devices. In addition, the prevalent non-linearities in nanomechanical devices make it difficult to distinguish additional damping mechanisms when the velocity is high.

However, due to their extremely high mass sensitivity it is thought that they would provide excellent detectors for vortices generated by nearby devices. It may be possible to trap a quantum vortex in several configurations with respect to a nanobeam, allowing vortices to be studied with more precision than ever before. We will discuss the effects of two such configurations in the next section.

3.6 Quantum Vortices Trapped by a Nanoscale Beam

A quantum vortex can couple to a nanobeam in multiple ways, forming several different configurations with different observed effects. The most energetically favourable result, is a single quanta of circulation trapped along the length of the nanobeam, such that the vortex-core becomes replaced with the nanobeam material. In such a configuration, the interaction of the vortex with the substrate results in an attractive force. The attractive effect can be understood in the framework of an image-vortex with opposite circulation which represents the boundary conditions imposed by the zero circulation condition at the substrate. The image-vortex will be a distance $2d$ from the real vortex, where d is the beam-substrate distance. The interaction force between two such vortices is given by [93]

$$\mathbf{F} = \rho_H \mathbf{v}_s \times \boldsymbol{\kappa}, \tag{3.67}$$

where $\boldsymbol{\kappa}$ is the constant of circulation. The magnitude of the force on a nanobeam of length L is therefore given by

$$|F| = \frac{1}{4\pi}\frac{L}{d}\kappa^2 \rho_H. \tag{3.68}$$

This force will act between the beam and the substrate and therefore add an additional tensile strain on the nanobeam. The magnitude of the tension at the clamped ends can be calculated by approximating a parabolic displacement of the structure given by

$$z(x) = \frac{1}{2}\frac{F}{E}\left(\frac{x}{t}\right)^2 \frac{(L-x)^2}{twL}, \tag{3.69}$$

where t and w are the thickness and length of the nanobeam, and E is the Young's modulus. The maxima of the displacement is at the centre, and given by

$$z_{max} = \frac{1}{32}\frac{|F|}{E}\frac{L^3}{wt^3}. \tag{3.70}$$

The effective additional tension at the clamped ends is hence given by

$$T_v = \frac{1}{2}|F|\frac{L}{t}. \tag{3.71}$$

Additional tension acting on the nanobeam will act to increase the spring constant, and therefore the resonance frequency. In this case, we would not expect a significant increase in the damping, since no additional loss mechanism arises from a vortex becoming trapped in this way.

Alternatively, a vortex may become trapped perpendicular to the nanobeam such that part of the vortex is pinned to the nanobeam, with the other ends connected or bounded to the walls. Under such a configuration, nanobeam motion could create excitations along

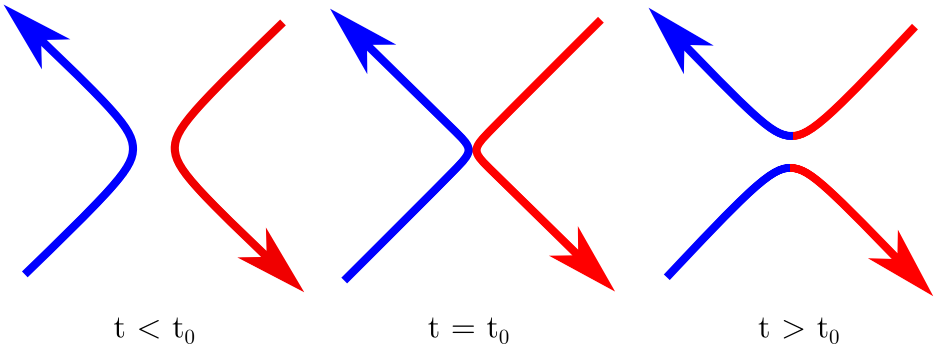

Fig. 3.9 Schematic diagram showing the process of vortex reconnection. Two anti-parallel vortices interact at $t = t_0$, resulting in two new vortices with a new orientation. Such a process may allow a trapped vortex to escape when it interacts with another nearby vortex.

the vortex, known as Kelvin waves (introduced in Sec. 2.3), which would constitute an additional damping mechanism. It is not precisely known how nanobeam kinetic energy would transfer into Kelvin waves, and what the efficiency of such a process would be. A vortex trapped in this way would not contribute significantly to the tension experienced and therefore the effect on the nanobeam frequency is expected to be minimal.

A vortex can escape a given configuration by the process of vortex reconnection. Here, a vortex with the opposite circulation interacts with the trapped vortex such to create two new vortices with a rotated orientated. This process is shown schematically in Fig. 3.9, where t_0 refers to the moment of interaction. The timescale over which reconnection occurs is related to the distance to the nearest vortex, due to the attractive force between the two vortices. The minimum distance, δ, between reconnecting vortices is related to the reconnection time, t, by $\delta \propto t^{1/2}$ [94]. Importantly, the minimum distance between vortices can be much smaller than the average inter-vortex spacing meaning reconnection can occur quickly, despite a low global vortex density.

3.7 Driving Nanoscale Beams using a Phonon Flux

We have established that a nanomechanical device should be highly sensitive to the momentum of thermal quasiparticles in ^{4}He. Sensitivity to quasiparticles in superfluid ^{4}He allows us to propose a novel driving technique for nanomechanical resonators. In this scheme temperature is transferred to the fluid via a nearby heater, creating quasiparticle excitations with some momentum. By periodically modulating the heating we can create bursts of phonons in the condensate which propagate ballistically, transferring their momentum to the detector beam. When the modulation of the phonon flux matches the resonant frequency of the detector, the nanobeam is excited into motion. The concept is similar to previous experiments where the momentum of heat flux has been measured using a suspended heater [95]. We imagine an experiment where a heater and detector nanobeam are mounted in plane, separated by some distance which is large compared to the phonon wavelength, with the temperature low-enough such that quasiparticles propagate ballistically. This section aims to present the mathematics of such a scheme, estimating the magnitude of the motion on the receiver. In addition, the effects of a number of spurious mechanisms will also be discussed.

3.7.1 Detected Power from a Phonon Flux.

To model the process by which the generated phonon flux is translated into force on the detector, we begin with the dispersion relation for the momentum carriers. This tells us the amount of quasiparticle momentum we can generate for a given input power. From Eq. (2.24), the phonon dispersion follows a linear relationship with the sound velocity in the superfluid approximately constant up to a phonon temperature approaching 10 K [3]. We therefore approximate that the temperature is low enough such that the momentum of a phonon is linearly proportional to the energy.

If we assume that all the energy dissipated in the heater generates ballistic phonons in the superfluid, the number of phonons leaving the heater per unit time, $\dot{n}_1$, is linearly proportional to the applied power, $P_{\mathcal{H}}$, *i.e.*, $\dot{n}_1 = P_{\mathcal{H}}/E$, where E is the phonon energy. In theory, this will not be the case, due to the high thermal-boundary resistance between the heater and the helium. However, the thermal boundary resistance for structures approaching the phonon wavelength have yet to be studied in detail, and it is thought that the boundary resistance could be much smaller than that of the bulk.

Assuming isotropic phonon emission from the heater into a sphere, the fraction of generated phonons that can excite the detector beam, $n_2/n_1 = \alpha tl/(4\pi r^2)$. Here, α, is a constant accounting for reflections from the substrate. Since the typical distance from the nanobeam to the substrate is much smaller than the phonon wavelength, it is thought that these reflections would remain coherent. The extent to which the phonons reflect off the substrate is governed by the specularity of the interaction, varying from fully diffuse ($\alpha = 1$), to fully specular ($\alpha = 2$). The distance between the heater and detector is given by r, while t and l are the thickness and length of the detector, respectively.

The force on the detector, F, can therefore be written as the rate of momentum exchange of phonons with the nanobeam

$$F = \alpha \dot{n}_2 p_{\mathrm{ph}} = \frac{\alpha^2 tl}{2\pi r^2 c_{ph}} P_{\mathcal{H}}, \tag{3.72}$$

where the parameter α now also accounts for the phonon scattering mechanism with the beam, again varying from 1 in the diffuse case, to 2 for the specular case. Given the simplicity of the model, we approximate the specularity of the phonon-substrate interaction to be equal to that of the phonon-nanobeam interaction.

Provided that the detector nanobeam motion is described as a harmonic oscillator to first order, the velocity amplitude is given by $v = \omega_0 x = FQ/m\omega_0$, where ω_0 is the angular resonance frequency, m is the effective mass of the beam, and x is the displacement amplitude. The power generated by a conductor moving in a perpendicular magnetic field, B, is given by $P_{\mathcal{E}} = \mathcal{E}^2/Z = (vBl)^2/Z$, where Z is the effective circuit impedance and $\mathcal{E}$ is the induced emf. For a nanobeam enclosed by a power amplifier, this value is given by $Z = 50, \Omega$. We conclude that the expected power generated by the nanobeam motion is proportional to the square of the power applied to the heater for phononic driving:

$$P_{\mathcal{E}} = \frac{1}{Z}\left(\frac{FQBl}{m\omega_0}\right)^2 = \frac{1}{Z}\left(\frac{\alpha^2 QBtl^2}{2\pi r^2 c_{ph} m\omega_0}\right)^2 P_{\mathcal{H}}^2. \tag{3.73}$$

In addition, estimates based on typical geometries for such an experiment suggest that one in $\sim 10^7$ phonons emitted by the heater would exchange momentum with the detector.

3.7.2 Noise Power from Thermal Fluctuations

When considering the process of phonon flux detection, it is important to contrast this with the power one would detect if we were simply detecting motion caused by thermal fluctuations. Here we estimate the power generated by thermal fluctuations creating Brownian motion in the beam. The power measured at the receiver beam for each mode can be written as

$$p_{\mathcal{E}} = \frac{(vBL)^2}{Z_0} = (\omega a)^2 \frac{B^2 L^2}{Z_0}, \tag{3.74}$$

where v, a and ω are the velocity, amplitude and frequency of each mode. L is the resonator length, B is the magnetic field and Z_0 is the circuit impedance. To obtain the total power measured at the detector we must integrate over the full frequency range:

$$P_{\mathcal{E}} = \int_0^\infty S_{P_{\mathcal{E}}} d\omega = \frac{B^2 L^2}{Z_0}\int_0^\infty (\omega S_{a_n})^2 d\omega, \tag{3.75}$$

the amplitude spectral density, S_{a_n} for a generic force spectral density S_{F_n} is [96]

$$S_{a_n} = \frac{1}{(\Omega^2 - \omega)^2 + (\Omega^2/Q)^2}\frac{S_{F_n}}{m^2}, \tag{3.76}$$

where Ω is the frequency of the first mode, Q is the quality factor and m is the mass. The expected S_{F_n} for a 1D harmonic oscillator undergoing Brownian motion is given by [96]

$$S_{a_n} = \frac{\Omega}{(\Omega^2 - \omega)^2 + (\Omega^2/Q)^2}\frac{2k_{\mathrm{B}}T}{\pi mLQ}, \tag{3.77}$$

where k_{B} is the Boltzmann constant and T is the temperature. We obtain the integral:

$$P_{\mathcal{E}} = \left(\frac{2k_{\mathrm{B}}T}{\pi mQ}\right)^2 \frac{B^2}{Z_0}\int_0^\infty \left(\frac{\omega\Omega}{(\Omega^2 - \omega)^2 + (\Omega^2/Q)^2}\right)^2 d\omega. \tag{3.78}$$

This result must be solved numerically, and will be used to rule out thermal excitation of a nanomechanical device.

Chapter 4

Experiments on Nanoscale Beams in ^{4}He

This chapter will present the results of experiments using doubly-clamped nanomechanical devices to probe bulk superfluid ^{4}He at low temperatures. Sec. 4.3.1 presents vacuum measurements in which fundamental nanomechanical behaviour can be observed, Sec. 4.3.2 shows measurements made from 4.2 K to 1 K in the hydrodynamic regime of ^{4}He, and Sec. 4.3.3 shows those made below 1 K in the ballistic regime of ^{4}He. These experiments will be discussed separately with comparisons made between overlapping temperature regimes. Two cryostat setups were used over the course of these experiments: a 1 K immersion cryostat for measurements above 1 K and a cryogen-free dilution cryostat for measurements down to 7 mK. We will demonstrate the effects of the different dissipation mechanisms in each temperature regime, as well as the mechanisms governing the losses at the lowest temperatures.

In Sec. 4.3.4 we will describe our pioneering experiment demonstrating a unique nanobeam driving mechanism using phonons in ^{4}He. Since several sample designs have been utilised for these investigations, comparisons will be made with the advantages of each fabrication technology discussed.

4.1 Samples

Here we will outline the details of the measured devices and discuss the advantages of each design. Two types of nanomechanical devices have been measured with different manufacturing processes: Al-on-Si beams fabricated at Lancaster University and Al-on-Si_3N_4 composite beams fabricated at Grenoble-Alpes University. The key difference between the two substrates is the internal tension in the Si_3N_4 which pulls the nanobeam taught, whereas samples fabricated on Si rely on thermal contraction for tension.

The two fabrication processes are largely similar, differing on the choice of substrate and etching procedures. The details of the two fabrication methodologies are discussed in App. B1 and App. B2. For the Al-on-Si samples, the devices have nominal thickness, $t = 100\,\mathrm{nm}$, and width $w = 100\,\mathrm{nm}$. The Al-on-Si_3N_4 are larger with nominal thickness $t = 130\,\mathrm{nm}$ and width $w = 200\,\mathrm{nm}$. Pre-stressing is performed on the Si_3N_4 by baking

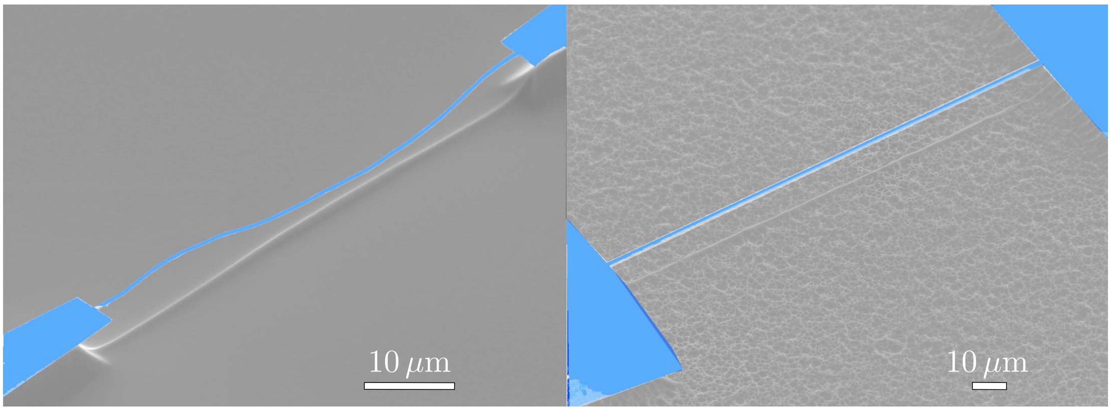

Fig. 4.1 SEM of two types of nanomechanical beam investigated in ^{4}He. Left: 50 μm Al-on-Si nanobeam fabricated at Lancaster University. Right: 150 μm Al-on-Si_3N_4 nanobeam fabricated at Grenoble Alpes University.

the substrate to a high temperature, introducing $T_0 = \sigma w t = 4 \times 10^{-5}$ N of tension on the nanobeams, where $\sigma = 0.9$ GPa is the substrate strain. The mechanical properties of the sample are defined by the Si_3N_4, with Young's modulus $E = 211$ GPa [97].

Scanning electron microscope images of the two nanobeam types are shown in Fig. 4.1. An immediate difference between these two images is the tension visible in the Si_3N_4 samples. Since these images are taken at 300 K this is not indicative of the structure at low-temperature. The Lancaster samples will stretch when cooled due to thermal mismatching and become more taught at low-temperatures, with the contraction given by $\Delta L/L = 4 \times 10^{-4}$ allowing us to estimate the tension $T_0 = wlE(\Delta L/L) = 3 \times 10^{-7}$ N, where $E = 70$ GPa is the Young's modulus for Si. The densities of the nanobeam materials are given by $\rho_{\mathrm{Al}} = 2600\,\mathrm{kg\,m^{-3}}$, $\rho_{\mathrm{Si}} = 2300\,\mathrm{kg\,m^{-3}}$, $\rho_{\mathrm{Si_3N_4}} = 3200\,\mathrm{kg\,m^{-3}}$ [97]. Conversely, in the Si_3N_4 sample, contraction due to thermal mismatching is a small contribution when compared to the pre-stressing procedure.

The samples were scribed and mounted onto a copper PCB, using vacuum grease in order to provide electrical isolation and a strong thermal connection, before aluminium wedge wire bonding is used to connect the chip to the PCB pads. The conductive pads are electrically connected to the central pin of a coaxial PCB connector. The connector ground pins are connected to the ground plane of the PCB. One PCB design used in these experiments is shown schematically in Fig. 4.2, with the first design featuring four RF (Radio Frequency) lines allowing two samples to be measured, and the second featuring six RF lines allowing three samples to be measured. The PCB was mounted inside a brass experimental cell via SMP high-frequency connectors, and to the outside of the cell by SMP feed-throughs. Further details of the cell designs is given in App. A2.

4.2 Measurement Scheme

As outlined in Sec. 3.2, the devices discussed in this work were driven magnetomotively using a perpendicular magnetic field. This was achieved by mounting the devices in a superconducting solenoid, such that the magnetic field was orientated vertically, whilst

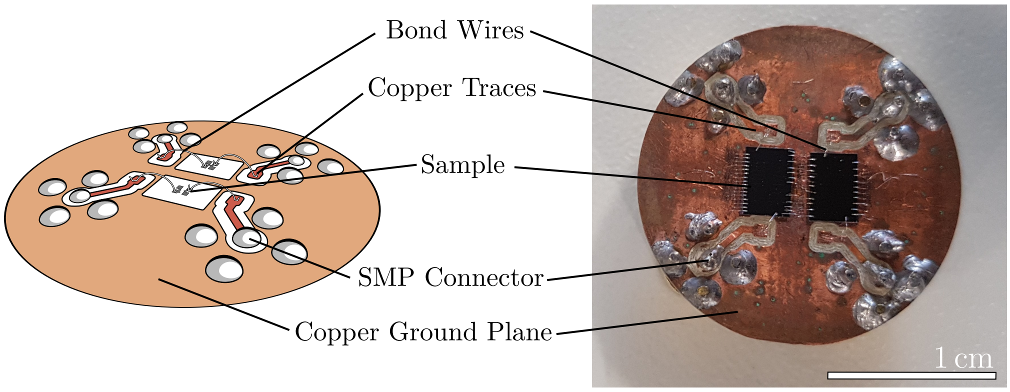

Fig. 4.2 Left: Schematic of PCB used in the investigation of nanomechanical beams in ^{4}He. Photograph of PCB design, with four SMP lines and the ability to mount two samples.

the samples were mounted horizontally. The magnets used in these experiments were able to supply a magnetic field of up to 5 T. From here, a vector network analyser (VNA) was used to supply an oscillating current of the form $I = I_0 e^{i\omega t}$. The signal was typically attenuated by 80 dB before reaching the sample, with the resultant signal amplified by a further 80 dB to improve the signal to noise ratio. The amplification is supplied by two 40 dB low-noise commercial amplifiers supplied by Femto. The high attenuation was used to protect the samples from high currents, known to be a common failure mode for nanomechanical beams. The electrical signals were then interpreted using the methods outlined in Sec. 4.2.1.

Measurements of these devices were performed from the helium condensation point using a 1 K-pot style cryostat from Oxford Instruments, with an insert developed in-house. This immersion system allows control of the temperature over the range 4.2 K to 1.5 K by reducing the vapour pressure of ^{4}He. Full experimental details of this cryostat can be found in App. A3.1, with the electrical schematic shown in Fig. A.4.

For measurements below 1 K a commercial Bluefors LD250 dilution cryostat was utilised with base temperature 7 mK. This system had been modified such that a helium cell could be mounted. Further detail of this setup is presented in App. A3.3, with the electrical setup shown in Fig. A.9.

4.2.1 2 Port Scattering Parameters

Measurements on nanobeams were often performed using a VNA, which measures the complex scattering parameters between port 1 and port 2. A schematic diagram representing the scattering matrix is shown in Fig. 4.3. A VNA directly probes this matrix by connecting the sample between port 1 and port 2. A voltage can then be applied across port 1 and the reflection, S_{11}, or transmission, S_{21}, measured. Alternatively, a voltage can be applied across port 2 and the reflection, S_{22}, and transmission, S_{12} measured. The

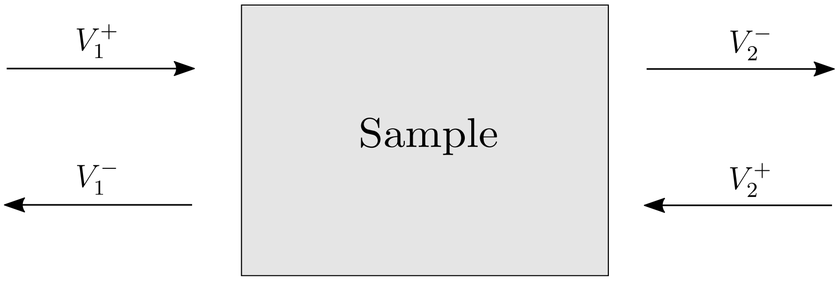

Fig. 4.3 Generic two-port scattering diagram, with a two port matrix representing the scattering of the black-box.

relationship between these parameters and the voltages defined in Fig. 4.3 is given by

$$\begin{pmatrix} V_1^- \\ V_2^- \end{pmatrix} = \begin{pmatrix} S_{11} & S_{12} \\ S_{21} & S_{22} \end{pmatrix} \begin{pmatrix} V_1^+ \\ V_2^+ \end{pmatrix}. \tag{4.1}$$

In order to probe devices, we typically probed the parameter S_{21} to measure the complex transmission through the sample. This is given by

$$S_{21} = \frac{V_2^-}{V_1^+}. \tag{4.2}$$

Both ports of the network analyser are terminated over $50\,\Omega$, meaning this quantity can be converted using $P = V^2/R$ giving

$$|S_{21}|^2 = \frac{P_2}{P_1}, \tag{4.3}$$

where P_1 and P_2 are the powers arriving at ports 1 and 2 respectively. Importantly, this quantity can be used to directly probe the power passing through a sample.

In the case of the nanomechanical beam, this allows us to estimate the peak velocity of the sample. From the definition of the quality factor as the ratio of the energy lost to the energy stored:

$$Q = \frac{P_1 |S_{21}|^2}{2\pi m v^2 f_0}, \tag{4.4}$$

where S_{21} is the value of the peak transmission, m is the mass and f_0 is the resonance frequency. Hence, the peak velocity can be written as

$$v = \sqrt{\frac{P_1 |S_{21}|^2}{2\pi Q m f_0}}. \tag{4.5}$$

In addition, since the work done per second is given by $dW/dt = Fv$, the force acting on the beam is

$$F = \sqrt{\frac{2\pi Q m f_0 P_1}{|S_{21}|^2}} = \frac{P_1}{v}. \tag{4.6}$$

From these simple kinematic considerations, the key mechanical properties of the beam can be estimated from experimental data. It is, however, difficult to obtain exact values of P_1 under real experimental conditions, due to impedance mismatching in the experimental circuit and other unknown dissipation mechanisms. The real P_1 at the resonator is typically higher than measured once amplifiers are accounted for. Velocities obtained using this method are therefore considered to be approximate. The agreement between the estimated velocity and the actual velocity will be highest for lower frequency devices due to less reflected power at interfaces.

4.3 Results

In this section we will outline the main results from experiments involving nanomechanical beams in the bulk phase of ^{4}He. The data discussed here is the result of three main experimental efforts. First, measurements of Lancaster made Al-on-Si nanobeams of varying length using an immersion cryostat, down to 1.5 K. Second, measurements of Lancaster Al-on-Si nanobeams were made in vacuum at 7 mK using our dilution cryostat. Finally, Grenoble Al-on-Si_3N_4 nanobeams were measured in the dilution cryostat, both in vacuum and ^{4}He from 4 K to 10 mK highlighting all key damping regimes. Al-on-Si_3N_4 nanobeam were further utilised to make the first measurements of the ‘phonon wind’ in bulk ^{4}He.

4.3.1 Vacuum

Initially all nanobeams were characterised in vacuum at 4 K. From these measurements the intrinsic properties of the beams can be extracted. We initially drove the beams in the linear regime, where the induced e.m.f., and therefore velocity, is linearly proportional to the force on the beam.

Figure 4.4 shows the fundamental resonance frequency for five Al-on-Si nanobeams, and two Al-on-Si_3N_4, as measured at 5 T and 4 K. It is clear that, as expected, longer nanobeams have lower frequencies for a given substrate. In addition, Al-on-Si_3N_4 nanobeams have a much higher frequency for a given length due to the inherent tension in the system. The higher frequency of the Al-on-Si_3N_4 can negatively affect sensitivity in ^{4}He at the lowest temperatures due to increased acoustic emission. The two theoretical curves are calculated using Eq. (3.20), using values from Sec. 4.1. The model gives reasonably good agreement for the fundamental modes, typically within 20%, however highlights the difficulty in accurately predicting the frequency of nanoscale oscillators. Although lithographically defined, inhomogeneous etching and material impurities become increasingly prevalent at these length scales. Even amongst samples which have undergone simultaneous fabrication the fundamental mode frequency can vary by $\sim 30\%$. These measurements were performed at low-drives, and hence in the linear regime, however at high drives non-linear effects can shift the frequencies from the stated values.

Figure 4.5 shows the frequency response of the transmission for a 150 μm Al-on-Si_3N_4 beam. At low driving powers, the sample shows the expected Lorentzian response. As the driving power is increased, the non-linear terms in the spring constant become relevant and the system behaves as a Duffing oscillator, as predicted in Sec. 3.1.1. Using 4.5, the

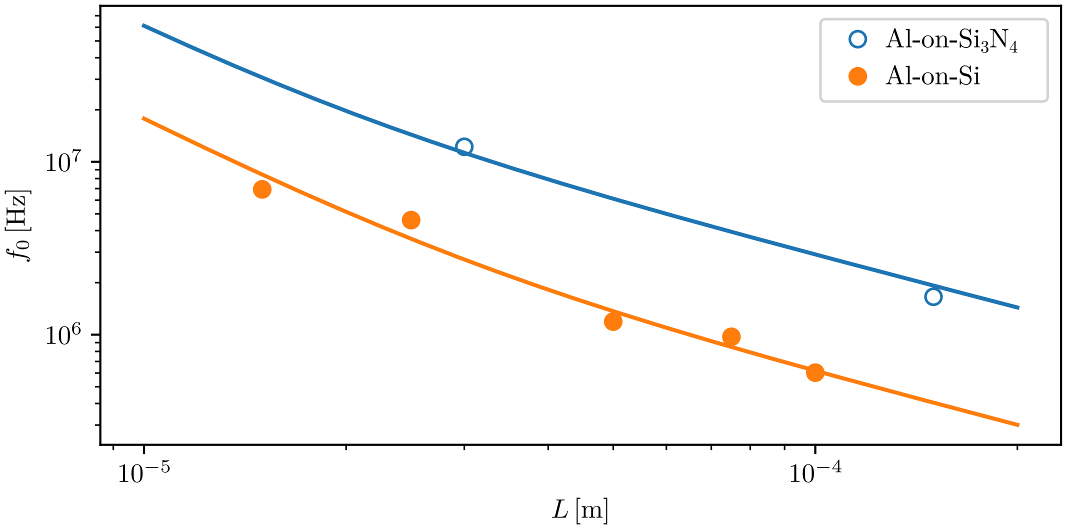

Fig. 4.4 Fundamental resonance mode for the two nanobeam design measured at 5 T and 4 K. The theoretical curves for the fundamental modes are calculated from Eq. (3.20), using the values from Sec. 4.1, and a moment of inertia $I = wt^3/12$.

transition to such the non-linear regime occurs at $v \sim 80\,\mathrm{cm\,s^{-1}}$. A Duffing-like response is characterised by an asymmetrical frequency response, with a sharp step on one side, owing to a bistable regime in the vicinity of the step. Due to the complexity of modelling such a system, it is difficult to extract meaningful experimental results for a probe in the Duffing regime; the FWHM does not accurately characterise the damping. For this reason, Eq. (4.5) no longer provides a good estimate of the nanobeam velocity. To avoid such difficulties, probes were typically operated below the point at which the Duffing-like non-linearities significant.

In the linear regime, at constant magnetic field, we observed constant damping in nanobeams. However, the damping is strongly dependent on the magnitude of the applied magnetic field, as discussed in Sec. 3.4.3. Figure 4.6(a) shows the damping as a function of magnetic field for two Al-on-Si samples in vacuum at 7 mK. It is clear that magnetomotive damping dominates for measurements performed at 5 T, with the characteristic B^2 dependence shown by the dashed-black lines. The magnetomotive damping is largest for longer samples, in agreement with the theory. At lower fields the damping plateaus for both samples due to the presence of another, field-independent damping mechanism.

The damping on the plateau region is likely governed by thermoelastic dissipation with raised temperature due to Joule heating in the beam, described phenomenologically in Sec. 3.4.2. The magnitude of this effect is larger for longer beams, due to the added difficulty in thermalisation of the nanobeam. Since Joule heating cannot occur in the superconducting state, a sharp change in nanobeam damping is observed at the transition for both samples. Both nanobeams demonstrate a superconducting transition at ∼130 mT, where the dissipation decreases. The superconducting transition is clear from looking at the off-resonance transmission as a function of magnetic field, as shown in Fig. 4.6(b).

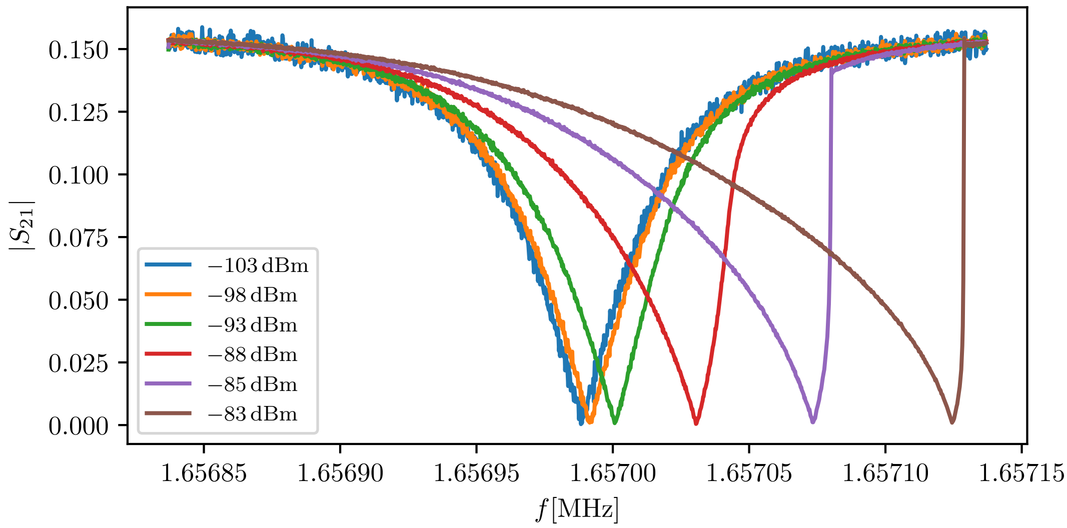

Fig. 4.5 Frequency dependence of $|S_{21}|$ for six values of driving power for a $150\,\mu$m Al-on-Si$_3$N$_4$ beam, taken at $5\,$T in vacuum at $10\,$mK.

Here, as we decrease the field, the first step corresponds to the superconducting transition in the nanobeam, H_c, with the second step corresponding to the transition in the wire-bonds. Due to the finite size of the London-penetration depth, thinner samples of a given material will have a larger critical field, consistent with our observations.

The mechanisms of damping in the superconducting regime is the source of much theoretical discussion and experimental work [98]. The damping still appears to have a strong power and field dependence, despite the fact that thermoelastic effects should be greatly suppressed due to the absence of Joule-heating.

To further investigate this phenomena, measurements of the damping in the superconducting state have been performed in vacuum using Al-on-Si$_3$N$_4$ nanobeams. Figure 4.7(a) shows the damping as a function of magnetic field for five different values of the excitation power. Figure 4.7(b) shows the off-resonance transmission to demonstrate the onset of superconductivity at $\sim$54$\,$mT.

The presence of a strong power dependence for the damping in the superconducting regime points towards variations in the occupation of two-level fluctuator systems. Similar effects have been previously observed as a function of the device temperature, with the damping demonstrating a $Q^{-1} \propto T$ at the lowest powers [98]. Temperature varies the density of states for quasiparticles in the materials, which similarly occurs with changes in magnetic field. It is therefore expected that we observe a decrease in losses at lower fields. Importantly, the highest sensitivity of our probes is achieved at low field and low driving power, however this also corresponds to the lowest signal-to-noise ratio. It is therefore important to tune these parameters, such that the damping of the medium under study remains higher than the intrinsic nanobeam damping, while simultaneously maximising the signal-to-noise ratio.

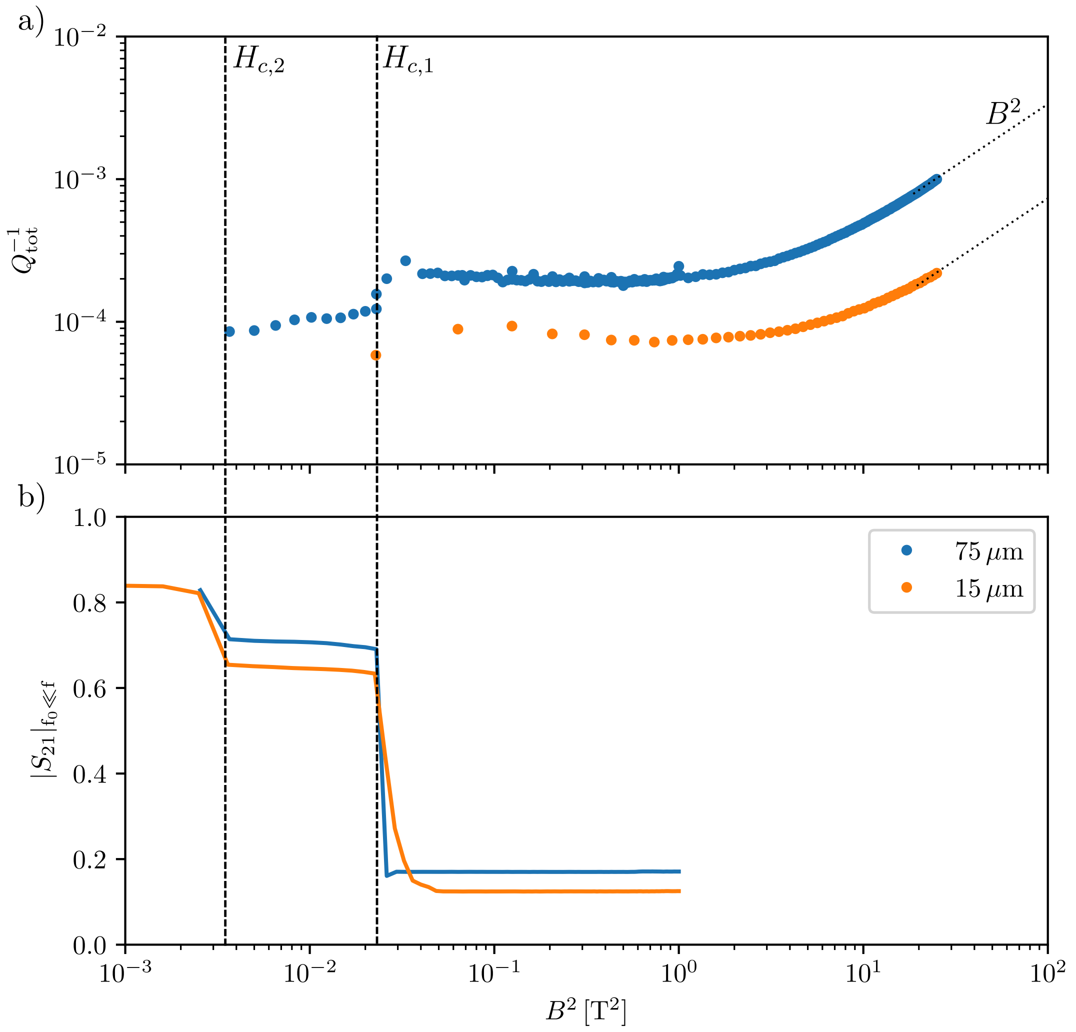

Fig. 4.6 Damping for two Al-on-Si nanobeams in vacuum as a function of the applied magnetic field. The superconducting transition in the beam is shown clearly at $B = 130\,\mathrm{mT}$. This is accompanied with a reduction in the damping in both samples. A second step is seen, most-likely corresponding to the superconducting transition in the aluminium bond wires. The labels $H_{c,1}$ and $H_{c,2}$ refer to the superconducting transitions in the nanobeam and wire-bonds respectively.

4.3.2 Hydrodynamic Regime of ^{4}He

Now that we have characterised the nanobeams in vacuum, we can investigate nanobeam sensitivity in liquid ^{4}He for different resonators lengths. Three Al-on-Si nanobeams were measured using the setup described in App. A3.1, in the bulk phase of ^{4}He. We measured the resonance properties of our devices as a function of the ^{4}He temperature, to determine which had the greatest sensitivity to the condensate.

Figure 4.8(a) presents the change in the fundamental resonant frequency of three nanobeams from $T = 4.2\,\mathrm{K}$ to $T = 1.5\,\mathrm{K}$, measured using a 5 T field. Above T_λ, the frequency of all nanobeams remains relatively constant, changing only due to temperature variations in the normal-fluid viscosity. Below T_λ however, when the helium transitions to a superfluid, a corresponding increase in frequency is observed. Our model is given

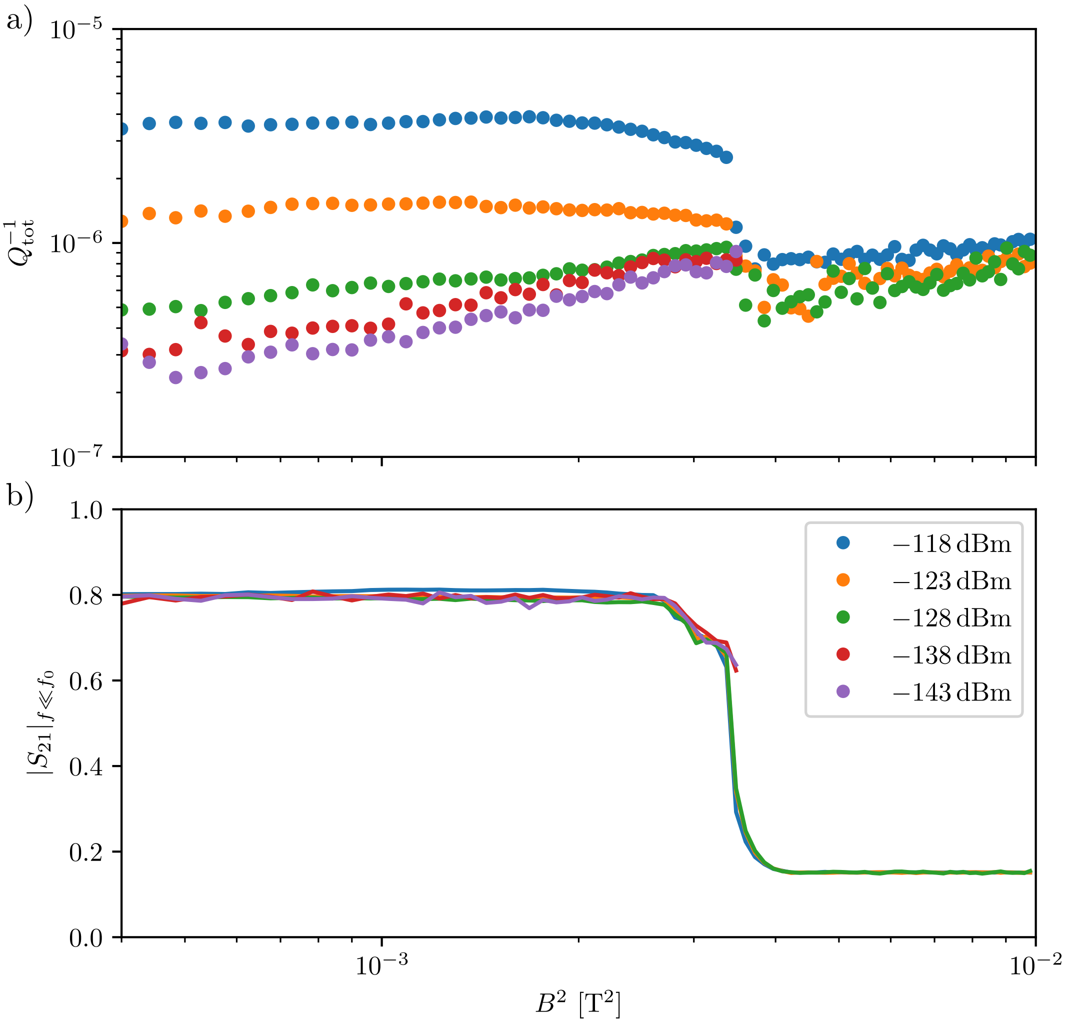

Fig. 4.7 (a) Damping for two Al-on-Si$_2$N$_3$ nanobeams as a function of the applied magnetic field. The superconducting transition is clearly visible from the sudden change in damping. The damping in the superconducting state appears to have a strong dependence on the applied power. (b) Transmission off-resonance clearly indicating the superconducting transition.

by Eq. (3.44) from Sec. 3.5.1, and incorporates the effects of the changing normal-fluid fraction in this region. Using various values for the constants A and B, the model produces an excellent fit to the data below T_λ. The fitting parameters A, B are stated in Table 4.1. Above T_λ however, the frequency dependence for all nanobeams is much flatter than the model predicts.

The large deviation from the model above T_λ can be explained by the viscous penetration depth. When the helium is in its normal-state, the viscous penetration depth is comparable to the nanobeam dimensions. For the 50 μm nanobeam, the penetration depth is $\sim w/4$ in the normal-state. For the 50 μm and 75 μm the penetration depth is approximately equal and for the 100 μm $\delta \approx 135$ nm. The penetration depth rapidly increases in the superfluid region as the normal fluid density decreases. This means the volume of the fluid displaced and volume of the penetration depth in Eq. (3.44) are

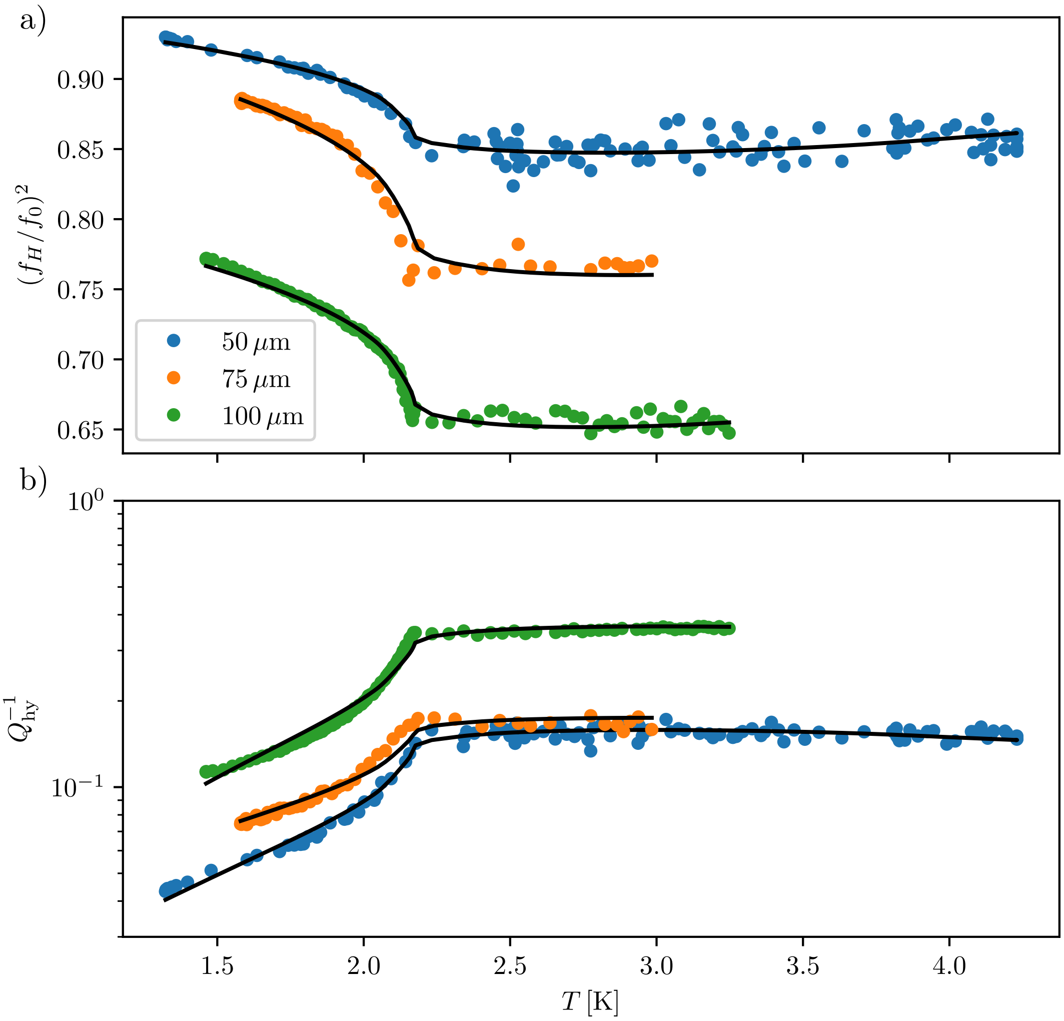

Fig. 4.8 (a) Squared ratio of resonance frequency in liquid helium and vacuum, and (b) inverse quality factor, for three nanomechanical devices of varying length from 4.2 K to 1.5 K. The black curves represent a theoretical model given by (a) Eq. (3.44) and (b) Eq. (3.46), with fitting parameters stated in Table 4.1.

equal orders of magnitude. The model treats the clamped fluid and backflow as separate terms which do not influence each other. When the volume of clamped fluid becomes comparable to the size of the nanobeam, it will influence fluid backflow and the two cannot be treated separately. Nanomechanical devices are therefore approaching the limit of the current theoretical model, which relies on an assumption of small penetration depth compared to the oscillator length scale.

Figure 4.8(b) presents the variation of the damping, $Q_{\rm hy}^{-1}$, with temperature for the three nanobeams. By comparison with Fig. 4.6, we can see that the hydrodynamic damping is far larger than the magnetomotive damping in this regime ($Q_{\rm hy}^{-1} >> Q_{\rm mm}^{-1}$). Similarly to the frequency, the damping remains relatively constant above T_λ, and decreases significantly as the normal-fluid fraction decreases. The theoretical model for the hydrodynamic damping is provided by Eq. (3.46) with parameters given in Table 4.1, providing a reasonable fit for all three nanobeams. The 75 μm sample gives the best fit,

Beam Length (μm)	A	B	C
50	1.15	0.86	2.27
75	1.29	1.61	2.08
100	4.61	1.49	4.68

Table 4.1 Fitting parameters A, B and C for the hydrodynamic model plotted in Fig. 4.8, from Eq. (3.44) and Eq. (3.46), for three different values of nanobeam length. Theoretically, A and B are constants of the order 1, and $C = 2$ for cylindrical geometry. [26].

with fitting parameter of $C = 2.08$, close to the theoretical values $C = 2$ for a beam-like geometry. Below about 1.5 K all nanobeams appear to deviate from the Stokes' drag model, despite an excellent fit work at high temperatures. The variations in the fitting parameter C among the other nanobeams is likely due to differences in surface-roughness and shape. We do not expect a significant contribution from acoustic drag due to the relatively low frequency, and very high hydrodynamic damping [33]. The deviation is likely due to the increasingly ballistic nature of the condensate at low-temperature, which will be discussed in more detail in Sec. 4.3.3.

Overall, the 50 μm seems to demonstrate the best agreement with the theoretical values of these parameters, and these values broadly agree with the expected values for cylindrical oscillators used in the past. The 100 μm geometrical values are quite far away from agreement, likely a result of the previously discussed mechanism, with the model operating outside of the assumptions as $\delta \sim w$. Despite this, the 100 μm beam demonstrated the best sensitivity to changes in the normal-fluid fraction, due to the very high aspect ratio of the sample. A comparison to more traditional probes, such as a NbTi vibrating wire, demonstrate that the nanobeams appear notably more sensitive [71]. Due to the difficulties in modelling, nanobeams are not particularly well suited for ^{4}He thermometry in the immediate vicinity of T_λ, however their real strengths lie in the sensitivity at lower temperatures, as we will show in the next section.

4.3.3 Ballistic Regime of ^{4}He

Two Al-on-Si$_3$N$_4$ nanobeams were measured in the bulk-phase of ^{4}He using the setup shown in App. A3.3. Figure 4.9(a) presents the temperature dependence of damping measured using a 150 μm beam in liquid ^{4}He from 4.2 K down to the base temperature for a range of magnetic field strengths. Larger magnetic fields produce a larger signal, at the expense of a larger magnetomotive, Q^{-1}_{mm}, contribution. For this reason, five different values of magnetic field were used to fully map-out the damping over this temperature range. In liquid ^{4}He, we can highlight two distinct damping regimes: hydrodynamic and ballistic. From 4.2 K to about 1.0 K, a hydrodynamic regime is again observed, where damping is dominated by Stokes' drag from the normal fluid surrounding the nanobeam. The data in this regime is in reasonable agreement with the model discussed in Sec. 3.5.1 and Sec. 4.3.2. However, since these measurements were performed using a cryogen-free fridge, temperature stability in this regime is fairly poor.

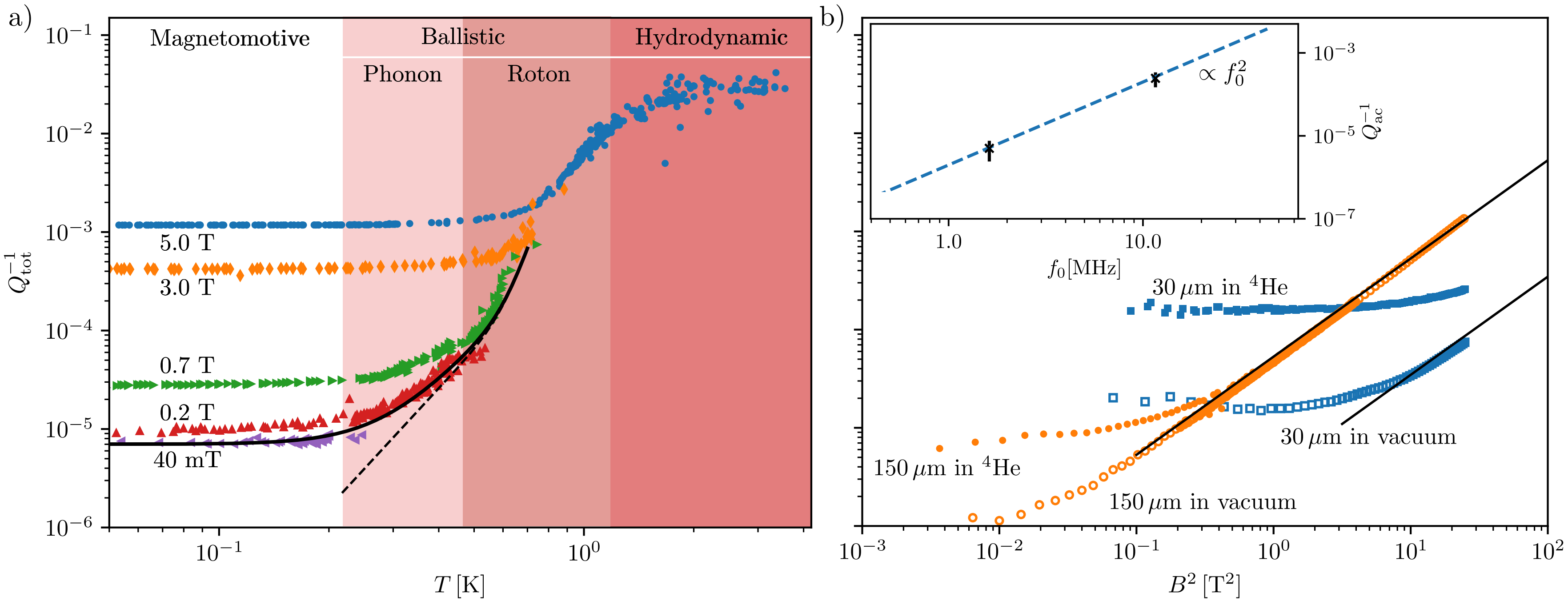

Fig. 4.9 (a) Temperature dependence of damping for a 150 μm sample in bulk liquid ^{4}He measured at a range of magnetic fields. The steep decrease of damping below 1 K is attributed to phonon and roton collisions in the ballistic regime. The dashed black line indicates the model, calculated as the sum of Eq. (3.50) and Eq. (3.52), adding a constant offset due to an acoustic emission term to obtain the solid black line. (b) Magnetic field dependence of the damping for 30 μm and 150 μm samples in vacuum and liquid ^{4}He at 7 mK. We observe a $Q^{-1} \propto B^2$ dependence at high fields, an external loading effect inherent to the measurement scheme. Notably, we observe a plateau corresponding to higher damping in low fields when ^{4}He is present. Inset: Q^{-1} for both samples as a function of frequency, with the blue dashed line showing the f_0^2 dependence as expected from the model given by Eq. (3.55), with fitting factor $A = 7.57$

Below 1.0 K damping is described by phonons and rotons ballistically colliding with the beam, as described in 3.5.2. The damping can be modelled using a sum of Eq. (3.50) and Eq. (3.52) taking the geometric constant $A = 2.67$ which assumes a cylindrical geometry. The model provides excellent agreement to the data in the temperature region $0.1\,\mathrm{K} < T < 0.8\,\mathrm{K}$, as evidenced by the dashed black line. There exists a region of temperatures $0.8\,\mathrm{K} < T < 1.1\,\mathrm{K}$ between the two regimes where the loss mechanisms are not well described by either model; the roton density dominates in the normal-fluid however interactions between rotons are infrequent but non-negligible. The lower temperature deviation from the ballistic model in Fig. 4.9(a) indicates that another, temperature independent, mechanism is present in addition to the phonon and roton damping contributions. We believe this is caused by the beam emitting sound waves in the superfluid. To demonstrate that the low temperature plateau is the results of acoustics we directly contrast the magnetomotive damping in vacuum and superfluid whilst exploring the effects of quantum turbulence on the nanobeams.

Figure 4.9(b) shows the magnetic field dependence of the damping for the two nanobeams in vacuum and superfluid ^{4}He as measured at the base temperature of the cryostat. The two solid black lines suggest that in high fields the beam damping is dominated by magnetomotive losses, which scale as B^2 as discussed in Sec. 3.4.3. The losses plateau at low magnetic field in both vacuum and ^{4}He. The saturation value for both beams in ^{4}He are nearly an order of magnitude higher as compared to the values in vacuum. The plateau of losses in vacuum indicates the presence of an intrinsic, magnetic field independent damping mechanism in both nanobeams. This intrinsic damping is presumably caused by thermoelastic effects, and is considerably reduced in the superconducting state (See Fig. 4.7). The fact that the low field damping in ^{4}He by far exceeds the damping in vacuum points to an extra dissipation mechanism in superfluid ^{4}He.

The inset of Fig. 4.9(b) demonstrates that the additional contribution to damping in helium appears to depend strongly on the resonance frequency of the beam, indicating that this effect is acoustical in nature. Strong acoustic emission has been previously observed for quartz tuning forks immersed in superfluid ^{4}He [33], due to their high operation frequency. Acoustic damping for a beam can be described within the framework of a dipole emission, as discussed in Sec. 3.5.3. The model captures the phenomenological behaviour of the devices, but requires a fitting parameters $A = 7.57$. Such a disagreement could be explained by a slightly larger effective radius, non-cylindrical geometry, or an additional damping term related to remnant vortices pinned to the nanobeam. Damping due to trapped vortices will be explored in detail in Chapter 5, where we will discuss if the disagreement can be explained these effects. It is clear that systematic study with a greater distribution of device frequencies is needed to draw further conclusions.

By adding a constant offset from the measured acoustic emission, the sum of acoustic, phonon and roton contributions to damping produces an excellent agreement to the data (the solid black line in Fig. 4.9(a)) at temperatures approaching $\sim 1\,\mathrm{K}$, above which the superfluid enters the hydrodynamic regime. The level of acoustic emission is the

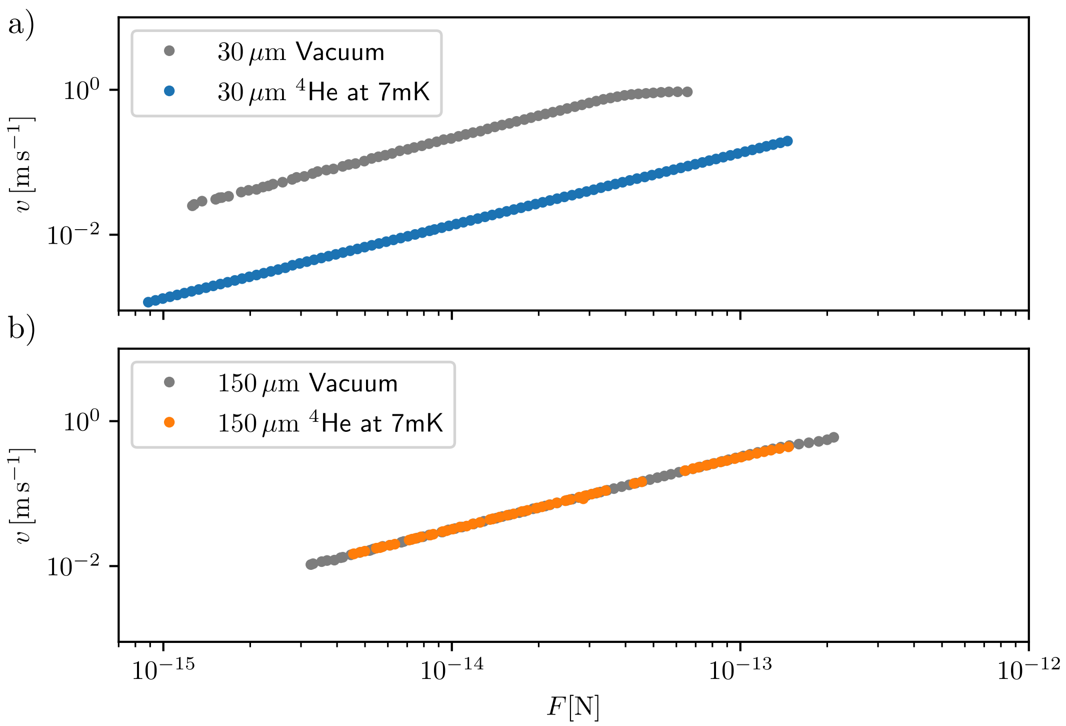

Fig. 4.10 (a) Force-velocity relation for a 30 μm Al-on-Si_3N_4 beam both in vacuum and superfluid ^{4}He at 7 mK, taken at 1 T. A linear response up to $\sim 1\,\mathrm{m\,s^{-1}}$ is seen in vacuum, where a transition to a Duffing regime is seen. No Duffing or turbulent transition is seen in ^{4}He since the velocities achieved were too low. (b) Force velocity relationship for a 150 μm long Al-on-Si_3N_4 nanobeam, in vacuum and liquid ^{4}He, at a 1 T field. The lines overlap due to magnetomotive damping being dominant in this sample. Duffing-like behaviour is seen at high velocities in both vacuum and ^{4}He, but no turbulent transition is seen in ^{4}He.

only required fitting parameters, demonstrating that the beam is an excellent probe of superfluid excitations.

To explore the effects of quantum turbulence on the system, the effects of nanobeam velocity were investigated. Figure 4.10 shows the dependence of the peak beam velocity on the force applied for both the 30 μm and 150 μm in vacuum and ^{4}He at 10 mK. The data presented is taken at 1 T to preserve the signal-noise ratio and achieve large velocities.

For a system with a turbulent regime, with critical velocity v_c, we would expect to observe a transition from a linear dependence to a quadratic dependence at v_c, as was discussed in Sec. 2.3. Given our length scale and frequencies, we estimate the critical velocity to be of the order of $0.5 - 1\,\mathrm{m\,s^{-1}}$. We measured the linear dependence of the peak driving force as a function of peak velocity and saw no evidence for turbulence creation up to velocities of tens of $\mathrm{cm\,s^{-1}}$ for either nanobeam. For the 150 μm nanobeam, the vacuum and ^{4}He results look very similar, due to the large magnetomotive damping at this field. For the 30 μm nanobeam a clear distinction is seen between vacuum and ^{4}He measurements, however no deviation from a linear dependence is seen for any force. The plateau seen in vacuum is caused by intrinsic, Duffing-like non-linearities in the system.

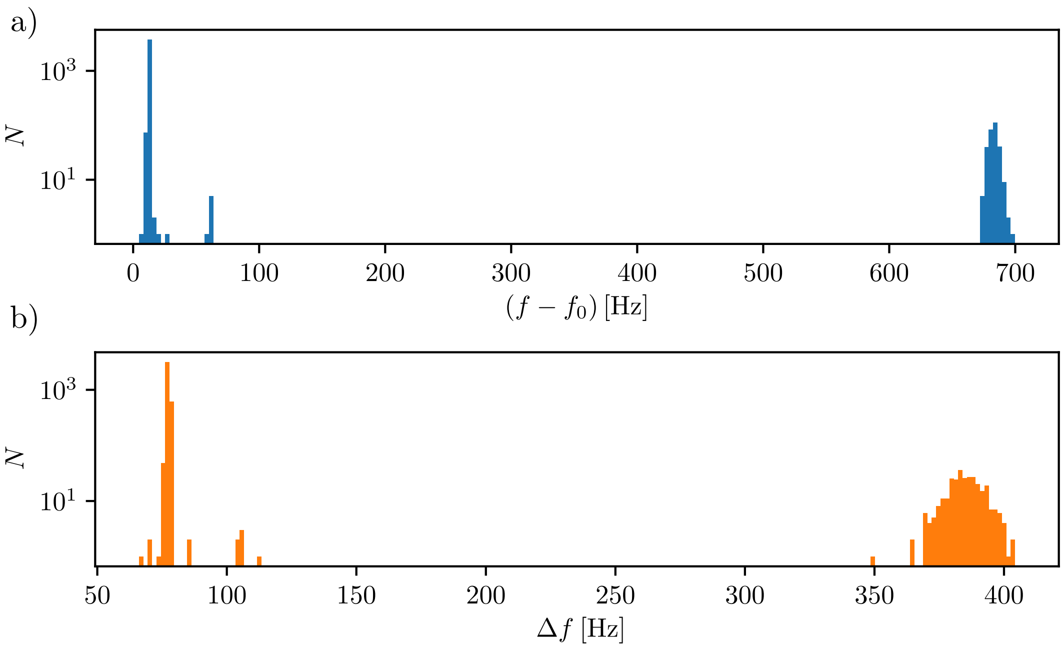

Fig. 4.11 Histograms of the (a) resonance frequency, and (b) width, of 3500 frequency sweeps taken for a 150 μm nanobeam in superfluid ^{4}He at 10 mK, taken at 1 T. The majority of events occur at the expected frequency and width predicted by magnetomotive damping, however $\sim 1\%$ of events transition to a region of higher frequency and damping. This is likely some manifestation of quantum turbulence. The resonance frequency is given by $f_0 = 1.62211$ MHZ.

Despite no obvious emission of vortices, time dependent measurements of the resonance properties of the nanobeam over several hours produced an unexpected result. Figure 4.11 presents a histogram of the resonance properties for 3500 measurements of the 150 μm taken at 1 T. The majority of results fall close to the usual resonance frequency ($f_0 =$ 1.6221 MHz), however a small number of events are shifted upwards in frequency, at a rate of $\sim 1\%$. These transient effects were not visible in previous measurements due to the relatively low sampling rate. The increase in frequency is coupled with a corresponding increase in damping experienced by nanobeam, with the frequency width, Δf, increasing from 70 Hz to around 380 Hz.

One possible mechanism for such an increase, is a quantized vortex becoming trapped between the nanobeam and the substrate, such that Kelvin-wave excitations can cause dissipation. In addition, the additional energy required to stretch the vortex contributes to the spring constant, hence the frequency increase. In Chapter 5, we will demonstrate the effects of quantized vortices on nanobeams using a separate generator. In this experiment however, we do not have a separate vortex generator, therefore any vortices in the fluid are likely remnant vortices in the fluid, produced by the Kibble-Zurek mechanisms when cooling. Although speculative, these results are the first signs that nanobeams may be used as detectors of single quantum vortices in the fluid, something we go on to explore in detail in Chapter 5.

4.3.4 Driving a Nanobeam with a Phonon Flux

Since nanobeams are such sensitive detectors of thermal excitations in superfluid ^{4}He, we were able to use them to demonstrate a new quasiparticle driving mechanism. Using the setup shown in App. A3.3, two Al-on-Si_3N_4 were utilised in the bulk-phase of superfluid ^{4}He at 10 mK to demonstrate the thermomechanical phenomena, coined the 'phonon wind'. To do this, the two nanobeams were mounted in-plane, on the same chip, separated by a distance of ~ 5 mm. The shorter, $30\,\mu$m-long beam was utilised as a heater, whilst the longer $150\,\mu$m-long beam was utilised as a detector. The $30\,\mu$m heater was driven off-resonance using an AC-current, with frequency $f_0/2$, where f_0 is the resonance frequency of the detector beam. Since the power dissipated in the heater goes as I^2R, where R is the heater resistance, this process generates modulated flux of phonons is generated at the frequency of the detector beam.

The phonons emitted in the direction of the detector propagate ballistically towards to the detector, due to an absence of scattering mechanisms in this temperature regime. Due to a short heater-to-substrate distance of $\sim 3\,\mu$m, phonons that are emitted towards the substrate and reflected do not acquire any significant phase-delay. The scattering mechanism occurring at the substrate will lie somewhere between complete reflection, and complete absorption, as discussed in Sec. 3.7. Phonons that reflect off the walls of the experimental cell are assumed to lose coherence, and simply contribute to the thermal background. Upon reaching the detector, phonons scatter off the beam and resonantly exchange momentum, a process capable of driving the detector beam into motion. A perpendicular magnetic field of $B = 1.3$ T was used to convert this motion into an electrical signal, which was then amplified through 80 dB at room temperature and detected using an SA, as shown in Fig. 4.12.

The power spectral density (PSD) of the measured emf signal from the detector is shown in Fig. 4.13(a) for three values of the applied heater power. A peak is observed at $f_0 = 1.62211$ MHz, in clear agreement with resonant driving of the detector. The width to the observed PSD implies there is some additional off-resonance driving occurring, an effect we attribute to any decoherence of the phonon flux. Additionally, the observed linewidth in this case would be limited by the quality factor of the resonance. Given the large magnetomotive damping expected at an ambient field of $B = 1.3$ T, the measured $Q = 9300$ is in good agreement the measurements presented in Fig. 4.9.

It is remarkable that the thermal time-constants in the system allow for such a process to occur. In order to generate a modulated phonon at a frequency of 1.6 MHz, the thermalisation time between the nanobeam phonons and the helium phonons must be $\sim 1\,\mu$s. Passing a current through the heater generates thermal phonons in the heater, however in order to generate a phonon flux in helium these phonons must pass through the Al-He boundary. For bulk-structures this effect should be slow, due to the large difference in the speed of sound in the two materials, resulting in a large acoustic mismatch and therefore inefficient energy exchange [99] [100]. In the heater however, the phonon wavelength is comparable to the size of the nanobeam, effectively increasing the probability of energy transfer by increasing the rate of interactions at the boundary, as

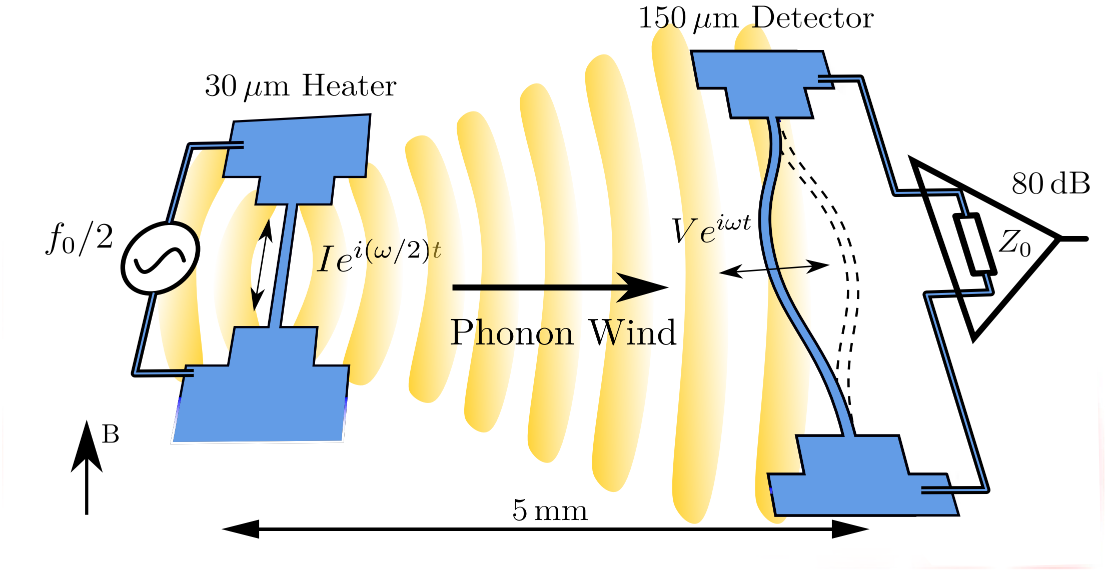

Fig. 4.12 Schematic of the experimental setup for detecting a phonon flux in liquid ^{4}He at 7 mK. A 30 μm and 150 μm nanobeam are separated by roughly 5 mm; the shorter beam is heated using an AC current creating periodic waves of phonons. The response from the second beam was monitored by a spectrum analyser.

has been observed in previous pulsed measurements performed in ^{4}He [101]. This result open a new avenue for high frequency transport and detection measurements in ^{4}He using nanoscale heaters.

The total detected power, $P_{\mathcal{E}}$, was calculated by integrating the experimentally measured PSD curves presented in Fig. 4.13(a). The dependence of the measured $P_{\mathcal{E}}$ as a function of the applied $P_{\mathcal{H}}$ is shown in Fig. 4.13(b), with the experimental uncertainties represented by the orange colour band. Our data qualitatively confirms that at low powers the detected signal is indeed proportional to the heater power squared within the accuracy of the measurement, as was expected from Sec. 3.7. Above an applied heater power of $P_{\mathcal{H}} \sim 1\,\mu$W the detector response deviates considerably from the predicted quadratic dependence and tends to saturate at higher powers. We attribute the observed deviation to the substantial overheating of the surrounding liquid, measured as a temperature increase at the mixing chamber. The dashed line inside the blue colour band shows the dependence predicted by Eq. (3.73) in the diffuse case, when ($\alpha = 1$), and assuming ideal impedance matching. The upper bound of the band corresponds to the specular case, whilst the lower bound accounts for possible impedance mismatching, as discussed in Sec. 3.7.

The agreement with the theory is remarkable given the simplicity of the model, and provides strong evidence that the described mechanism is actually exciting the beam. The weakness of the model lies largely in the efficiency of the phonon flux generation. We have no reliable method for accurately calculating the amount of power which directly generates phonons in the condensate. We can rule out direct excitation of the detector via electromagnetic cross-talk by the fact we excite at half the detector frequency. Separate characterisation of the signal-generator used to excite the heater confirms that there are

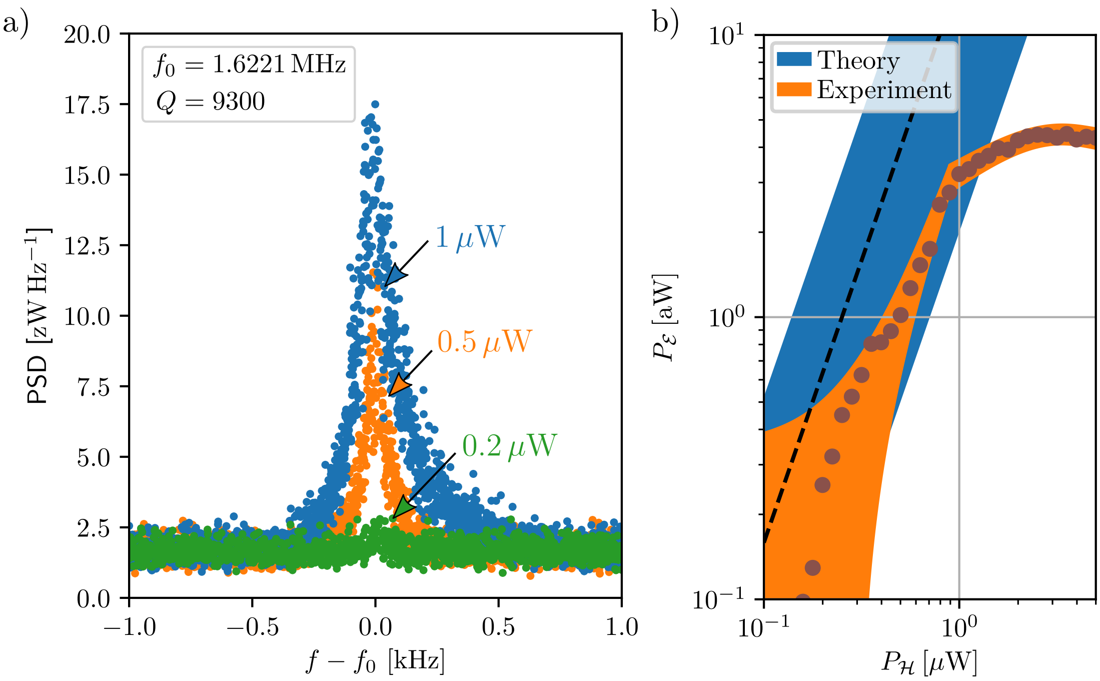

Fig. 4.13 (a) Power spectral density of the detector beam measured using a spectrum analyser at 1.3 T for three different values of the heater power, $P_{\mathcal{H}}$. The total received power corresponds to the area under these curves. (b) The total integrated power measured at the spectrum analyser from the detector as a function of emitter nanobeam power at 1.3 T. The black-dashed line shows a model given by Eq. (3.73), with the blue band accounting for uncertainty in the scattering mechanism $1 < \alpha < 2$, and impedance mismatching.

no significant overtones generated, and therefore the detector cannot be directly excited in this way.

We can also confidently rule out incoherent thermal excitation of the beam using the theory introduced in Sec. 3.7.2. The integral part of Eq. (3.78) can be solved numerically giving $= 1.84013 \times 10^{-7}$ Hz. With $Q = 10^4$, $M = 1.58 \times 10^{-14}$ kg and $\Omega = 1.62211$ MHz, the total expected power is given by

$$P_{\mathcal{E}} \sim 10^{-39}\,\mathrm{W}, \tag{4.7}$$

which is far less than the measured power, $P_{\mathcal{E}}$. It seems that despite the high sensitivity of the nanomechanical devices, they cannot directly probe thermal motion.

4.4 Conclusions and Outlook

The work presented in this chapter demonstrates the remarkable versatility of nanomechanical devices as probes for quantum fluid systems. We have presented measurements over a large temperature range in liquid ^{4}He, both in the hydrodynamic regime from 4.2 K to 1.2 K, and in the ballistic regime from 1 K to 10 mK. In the hydrodynamic regime, the temperature dependence of three nanobeams of varying length were measured.

Below T_λ, all three beams demonstrated excellent agreement with a theoretical model based upon normal-fluid clamping to the nanobeam, as discussed in Sec. 3.5.1. Above T_λ, the model was less successful, likely due to the volume of clamped fluid becoming comparable to the beam size. In this limit, the additional mass is dominant, rather than a small correction to the initial mass. Therefore in the direct vicinity of T_λ nanobeams are not as well suited for such measurements as conventional probes. As expected, the highest sensitivity to changes in the mass came from the $100\,\mu$m nanobeam, which was the longest tested.

Two nanobeams have been successfully measured in the ballistic regime of ^{4}He, demonstrating a striking ability to continuously operate despite environmental damping varying over six orders of magnitude. From 0.8 K to 300 mK the damping closely follows the damping model discussed in Sec. 3.5.2, a sum of the contribution of the the thermal quasiparticles, phonons and rotons, colliding the nanobeam. Below this, damping saturates due to the contribution of acoustic emission, as outlined in Sec. 3.5.3, limiting the ultimate sensitivity of the probes. In the future, designing longer nanobeams and therefore lower frequency nanobeams, would result in reduced acoustic emission thereby increasing the sensitivity. Fabricating extremely long doubly-clamped nanobeams without sacrificing structural rigidity remains a technical challenge. One solution is to fabricate cantilever-paddle style resonators, which have lower frequencies for a given dimension. Alternatively, embedding the nanobeams inside a cavity could suppress the number of acoustic modes available for energy transfer, reducing the losses by this mechanism. The results of this work are presented in publication I.

The nanobeams measured at the lowest temperatures in superfluid ^{4}He were utilised to demonstrate a unique thermomechanical phenomena, called the ‘phonon wind’. Here, two nanobeams are used, one operated as a heater and one as a detector. The heater is used to generate a modulated phonon flux in ^{4}He, and when the modulation frequency matches the resonance frequency of the detector beam it is able to excite motion. The signal from the phonon wind has been measured for the first time, demonstrating a phenomena that has never before been conceived. In doing so, nanobeams have demonstrated extremely fast thermal time constants, much faster than that seen in bulk materials, opening the door to new experiments involving high-frequency thermomechanics in quantum fluids. The results of this work are presented in publication II.

Overall, the experiments presented here have firmly pushed nanomechanical beams from a novel experimental device, to an integral element of several current, planned, and future experiments. Whilst the initial sections did not introduce any new physics, but demonstrated excellent agreement between the data and known theory, the final section utilised nanobeams to demonstrate an entirely new physical phenomena. Nanomechanical devices are now being utilised for the next generation of low-temperature experiments including, but not limited to, single-vortex detection, ^{3}He quasiparticle probing and integration with quantum circuits. The first results of single-vortex detection using a nanomechanical device are presented in the next chapter.

Chapter 5

Experiments on Vortex Dynamics probed by Nanoscale Beams

In this chapter we describe experiments utilising nanobeams as real-time detectors, and traps of quantised vortices in ^{4}He, using a submerged TF as a source of turbulence in the condensate. Our work draws inspiration from the pioneering experiments of Joe Vinen [20], who made the first observations of a quanta of circulation in ^{4}He, as introduced in Sec. 2.3, however utilising a modern methodology.

We will introduce two sets of experimental results. First, we will present experiments probing the dynamics of propagating vortex rings interacting with a nanobeam using a novel multi-frequency lock-in amplifier technique to track the resonance properties on the order of milliseconds. Such real-time vortex detection has never before been demonstrated, and has potential to greatly improve our current understanding of vortex emission and detection in fluids. Second, we show experiments using nanobeams to engineer trapped vortex configurations which can persist indefinitely, allowing the fundamental study of ^{4}He vortexes. These experiments may shed light on the microscopic processes by which energy is dissipated from quantized vortices in a superfluid, a topic of much interest in the physics community [102, 103].

5.1 Samples

The detectors used in the subsequent experiments consist of Al-on-Si_3N_4 nanobeams fabricated at Moscow-State University, using nominally similar fabrication procedures as those discussed in App. B2. The devices have lithographically defined thickness, $t = 130\,\text{nm}$ and length $L = 70\,\mu\text{m}$. Each chip consists of four devices of varying width, $w = 100, 200, 400, 800\,\text{nm}$, as shown in Fig. 5.1. For the discussed experiments, a nanobeam with width $w = 200\,\text{nm}$ was used (labelled ‘A’ Fig. 5.1). The device had a fundamental mode frequency $f_0 = 2.146\,\text{MHz}$. Using Eq. (3.20) the strain is estimated to be $\sigma = 0.2\,\text{GPa}$, lower than the devices discussed in Chapter 4. The resultant tension is therefore $T_0 = \sigma wt = 5.6\,\mu\text{N}$. For further details about the mechanical properties of such devices, see Sec. 4.1. In addition to the nanomechanical device, a flexural TF was also mounted in the cell, suspended $\sim 2\,\text{mm}$ above the nanobeam. The TF has tine length

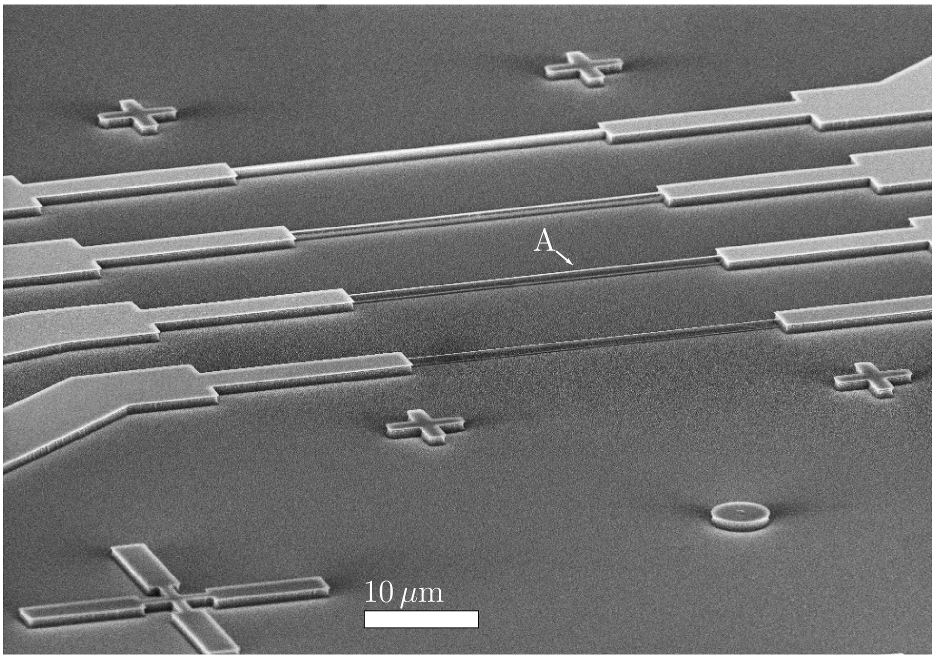

Fig. 5.1 An SEM of a chip containing four 70 μm Al-on-Si_3N_4 nanobeams of varying width. 'A' labels the $w = 200$ nm wide nanobeam used for the discussed experiments. The thinner 100 nm wide nanobeam was bonded however was not functional upon cool-down.

$l_F = 3.5$ mm, thickness $t_F = 250\,\mu$m and width $w_f = 650\,\mu$m, yielding a fundamental mode frequency of $f_f = 32.7$ kHz. TFs of this type are known emitters of quantized vortices in superfluids, making them an ideal source for studying the interaction of a nanomechanical device with quantum turbulence.

The nanobeams were bonded onto a copper PCB with the TF suspended in-plane above, as shown in Fig. 5.2. Two nanobeams were bonded, however only the 200 nm appeared to be properly suspended once measured. This was most likely due to over-etching leading to nanobeam collapse.

5.2 Measurement Scheme

All measurements were performed in bulk superfluid ^{4}He at mK temperatures using the setup described in App. A3.3. In order to study such a system several electrical measurement schemes were utilised. Firstly, the resonance properties of the nanobeam were resolved on slower time-scales using the spectroscopic approach of a VNA to supply an AC current in a perpendicular magnetic field. The back-emf was then measured as a drop in the transmission as a Lorentzian curve, similar to the methods used in Chapter 4.

In order to resolve faster changes in the resonance properties, continuous downconversion at a single frequency was performed, using a separate signal generator and IQ-mixer. This method allows changes of the order 100 μs to be resolved, limited by the transience of the resonator.

To implement the advantages of both previous methods, we went on to demonstrate a novel readout technique using a multi-frequency lock-in amplifier (MLA). Using a

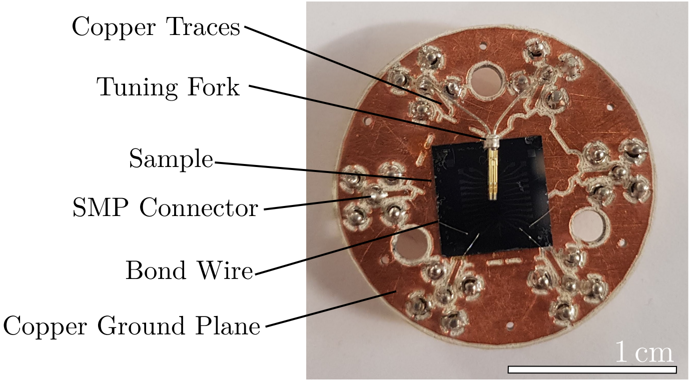

Fig. 5.2 PCB showing the setup for studying vortex dynamics using a nanobeam. A TF is soldered such that it is suspended $\sim 2\,\mathrm{mm}$ above a nanobeam chip. Two nanomechanical devices were bonded however only one was functional.

combined multi-frequency drive and multi-frequency demodulation, we were able to extract 41 frequencies signals simultaneously whilst maintaining a time resolution of 1 ms. The time resolution is ultimately limited by fourier mixing of nearby tones, meaning frequency spacing must be sacrificed for improved time resolution. Electrical schematics of the setup are shown in App. A3.3. MLA measurements have been used previously to measure TF turbulence in ^{4}He at lower sample rates [104].

When resolving fast changes in the resonance properties, it was necessary to use triggering functionality to distinguish between interesting events and the normal background. To do this, a feedback loop output the magnitude of the downconverted signal at the resonance frequency to an oscilloscope. When the signal fell below the trigger value, a trigger pulse was sent to the MLA to record data for a specified length before resetting. The properties of the TF were measured using a VNA to extract the Lorentzian curve, before fitting to extract the force-velocity characteristics using the method proposed in Sec. 3.3.

5.3 Results

The main results will be split into three sections. Firstly, the characterisation of both the nanobeam and TF in both vacuum and ^{4}He, similar to those discussed in Chapter 4. Secondly, the time-domain response of the nanobeam under bombardment with vortex-rings emitted by the TF. Lastly, the carefully measured properties of the nanobeam coupled to a trapped vortex under several configurations.

5.3.1 Characterisation

Figure 5.3(a) shows the force-velocity relationship for the nanobeam, taken at 5 T both in vacuum and in superfluid ^{4}He at 10 mK. The data was taken using a VNA to measure the Lorentzian, and analysed using the method introduced in Sec. 4.2.1. In superfluid ^{4}He at 10 mK the nanobeam frequency is given by $f_H = 2.116\,\mathrm{MHz}$, meaning an effective mass increase of 3%. For the nanobeam, force and velocity remain linear to each other which

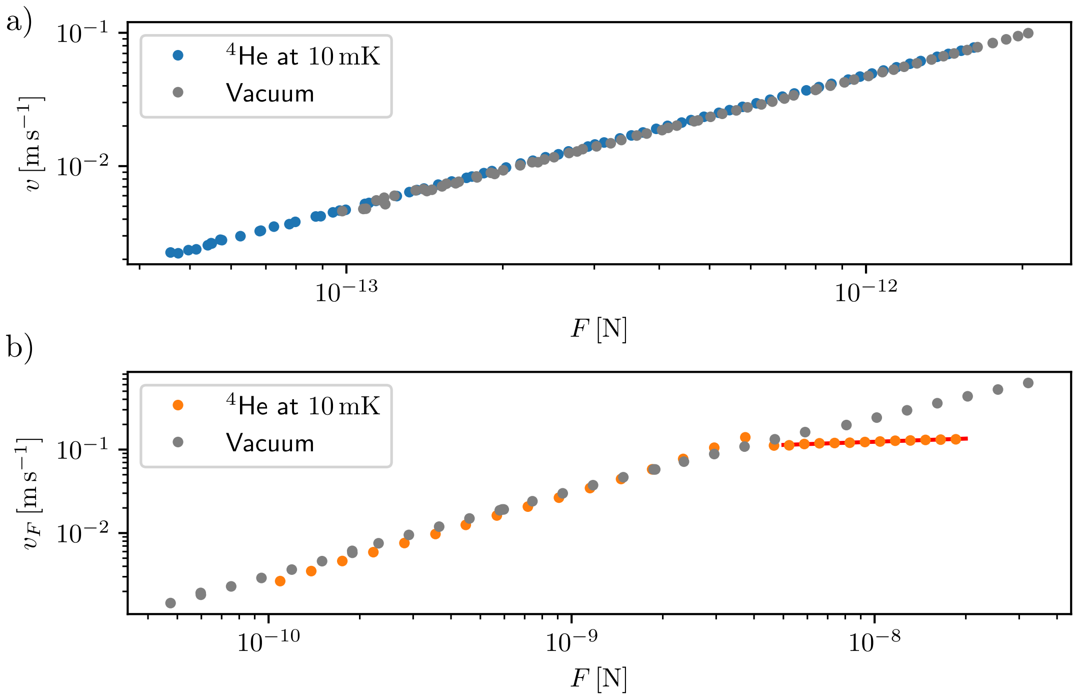

Fig. 5.3 Force-velocity relationship, in both vacuum and superfluid ^{4}He at 10 mK, for a: (a) 70 μm nanobeam at 5 T, showing no transition to a turbulent regime, (b) quartz TF, with the transition to a turbulent regime shown clearly by a characteristic 'kink' at $F = 4 \times 10^{-9}$ N. The orange fit line corresponds to the function $v = A\,F^B$, with $A = 1.08\,\mathrm{kg^{-1}\,s}$ and $B = 0.125$.

implies constant damping. Since measurements are performed at 5 T magnetomotive damping is dominant, so the damping in vacuum and ^{4}He are equal.

The TF, however, demonstrates a transition in gradient at $v_c = 11\,\mathrm{cm\,s^{-1}}$, corresponding to the onset of quantum turbulence, as shown in Figure 5.3(b). The red line represents a fit to the turbulent data, using a function of the form $v = AF^B$, yielding fit parameters $A = 1.08\,\mathrm{kg^{-1}\,s}$ and $B = 0.125$. Although turbulence is typically characterised by a $F \propto v^2$ ($B = 0.5$) relationship (see Sec. 2.3), at the lowest temperatures steeper gradients have been seen for TFs in previous experiments. Such an observation is evidence that the majority of the additional energy above v_c goes to creation of vortices. Since the nanobeam velocity has a linear relationship with the driving force, it can be used as a detector for quantized vortices created by the TF operating above the critical velocity. By running the TF above the critical velocity we can create propagating vortex rings in the condensate which can be detected by the nanobeam.

5.3.2 Real-Time Vortex Dynamics

No significant difference in the nanobeam response was detected as measured with a VNA when the TF was above v_c, to when it was below v_c. On short time-scales (~ 0.01 s), sudden events corresponding to short increases in the nanobeam frequency were observed, only seen when the TF was operating with $v_F > v_c$ in superfluid ^{4}He. Figure 5.4 shows a colour-map representing two consecutive events, as measured using

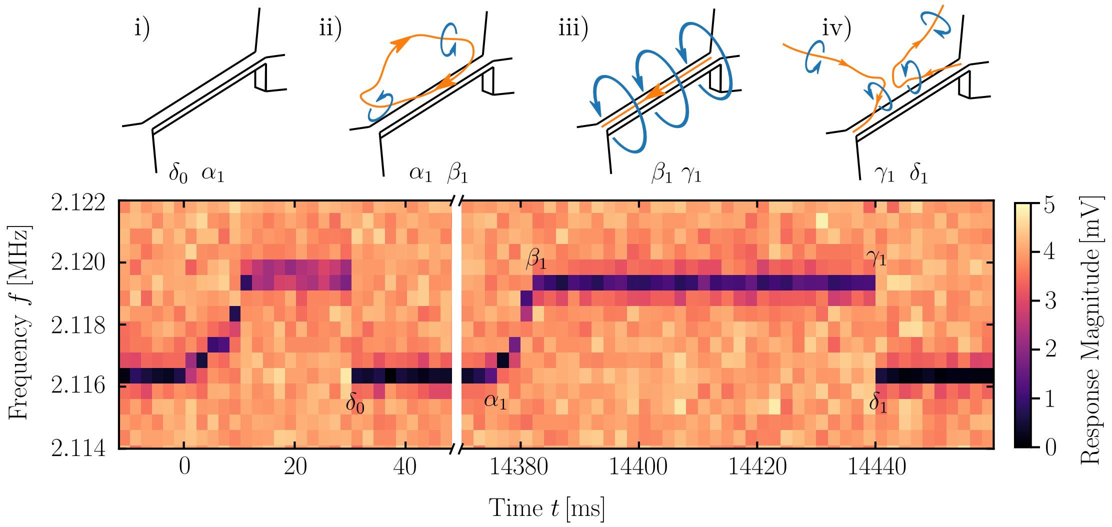

Fig. 5.4 Time dependence of MLA nanobeam response at a lock-in amplifier time constant of 2 ms. Two nanobeam events are shown, with the main features labelled. The 40 measurement frequencies were separated by 500 Hz with one frequency driving the NEMS. This event was recorded in a 5 T magnetic field, with nanobeam velocity $v = 3.5\,\mathrm{mm\,s^{-1}}$. Time is recorded relative to the trigger signal. The diagrams show our interpretation of the vortex state in each region.

an MLA simultaneously driving the nanobeam at 40 frequencies with 500 Hz spacing, at 5 T magnetic field, with nanobeam velocity $v = 3.5\,\mathrm{mm\,s^{-1}}$. The lock-in time constant for these measurements was $t_c = 2\,\mathrm{ms}$. Here, $t = 0$ corresponds to the trigger time, and the length of one event, $\beta_1\gamma_1 = 0.06\,\mathrm{s}$. The TF was being continuously driven with an AC force of magnitude force $F = 4 \times 10^{-8}\,\mathrm{N}$. Strikingly, there is a clear transience observed on the rise-side ($\alpha_1\beta_1$) whereas the fall-side transition is much faster ($\gamma_1\delta_1$). The frequency of the plateau region is at $f_v = 2.119\,\mathrm{kHz} = f_0 + 3\,\mathrm{kHz}$. The described features are repeated across a very large number of similar events, with variations only occurring in the length of the transience and the plateau regions.

The measured frequency shift of 3 kHz is extraordinarily robust to changes in experimental parameters. Over a range of nanobeam velocities $(1 < v < 4)\,\mathrm{mm\,s^{-1}}$, cryostat temperatures $(10 < T < 700)\,\mathrm{mK}$, magnetic fields $(2 < B < 5)\,\mathrm{T}$, and TF driving forces $(10 < F < 100)\,\mathrm{nN}$, the measured frequency shift varied just $\sim 1\%$. This is significant, since it implies that the observed state is strongly defined by the geometry of the system, and not by the oscillator mechanics.

Another clear feature is that the damping does not appear to change significantly in the higher-frequency state. The damping between the higher-frequency and normal state agree within 2 % of each other. However, since the majority of measurements were performed at 5 T significant magnetomotive damping may make it difficult to resolve small changes. Similar measurements performed at 2 T, where the magnetomotive damping should be six times smaller, reported similar agreement two states.

We believe that the measured behaviour can be explained by a single quanta of circulation becoming trapped along the length of the nanobeam, as is described in Sec. 3.6. The initial interaction gives us the rise time ($\alpha_1\beta_1$), shown in Fig. 5.4(ii), with the fully trapped state given by $(\beta_1\gamma_1)$, shown in Fig. 5.4(iii). The boundary condition due to the substrate will create an attractive force on the trapped vortex, increasing the effective tension felt by the nanobeam. Using Eq. (3.71), with a nanobeam-substrate gap of $1\,\mu$m, we estimate the additional tension at the clamps to be $T_v = 2.2\,$nN. If we consider the total beam tension to be $T = T_0 + T_v$, using Eq. (3.20) we find the nanobeam frequency in liquid to be $f_v = 2.117\,$MHz, an increase of $\sim 1\,$kHz. A vortex trapped along the nanobeam would also not contribute significantly to the damping, consistent with our observations. Considering the simplicity of the model it provides reasonable agreement, suggesting that our picture is at least partially correct. The model depends strongly on the nanobeam-substrate distance, a quantity that varies significantly across the substrate and across samples, due to anisotropic etch performed of the substrate. The mechanism by which the vortex initially becomes trapped is not yet well understood.

The relaxation of the nanobeam back to the non-trapped state is then explained by vortex-reconnection, as described in Sec. 3.6, shown in Fig. 5.4(iv). A vortex trapped along the nanobeam can escape when bombarded with another vortex ring, with the two meeting and then separating into a different configuration. Such a process may allow a trapped vortex to detach itself on a time-scale related to the inter-vortex spacing.

To clarify our picture, we aimed to investigate how the vortex-line density affected the rate of measured frequency-shift events. Normalised histograms of the ‘wait time’ as a function of the applied drive to the TF is shown in Fig. 5.5(a). The data is collected using a single-frequency drive and demodulation on the resonance frequency, with a time constant $t_c = 300\,\mu$s, and nanobeam velocity $v = 3.5\,\mathrm{mm\,s^{-1}}$. The wait time is calculated as the time between subsequent triggers, minus the time taken to save the data. At low TF drives the wait time can be very long, approaching infinity at the lowest drives, implying that the vortex line density in the cell can be very low. At higher drives the events are much more rapid, implying high vortex line density, however the difference is diminishing with higher drive. Such an effect points towards potential saturation of the vortex line density in the experimental volume.

The inset of Fig. 5.5(a) shows the fit constant τ as a function of the TF velocity, when the previous histograms are fitted $\propto e^{-\tau t}$. The orange line indicates the force value equivalent to the turbulent transition, v_c. It is clear that the event rate is closely tied to the TF drive, with higher drives meaning more energy going towards increasing the vortex line density, and therefore a greater interaction rate. Interestingly, the event rate falls to zero at a slightly higher value than v_c, which implies an additional energy cost associated with the emission of a vortex ring from the TF surface to the bulk. Two critical velocities have been previously observed in low temperature experiments involving TFs [105].

If reconnection from nearby vortexes allows the trapped vortex to escape, we might expect to observe some dependence of the event length on the vortex line density. Figure 5.5(b) shows probability histograms of the plateau length for several values of the TF drive. Clearly longer events are less likely for all powers, evidenced by a decreased probability for longer plateau lengths, however, longer plateaus appear to be equally

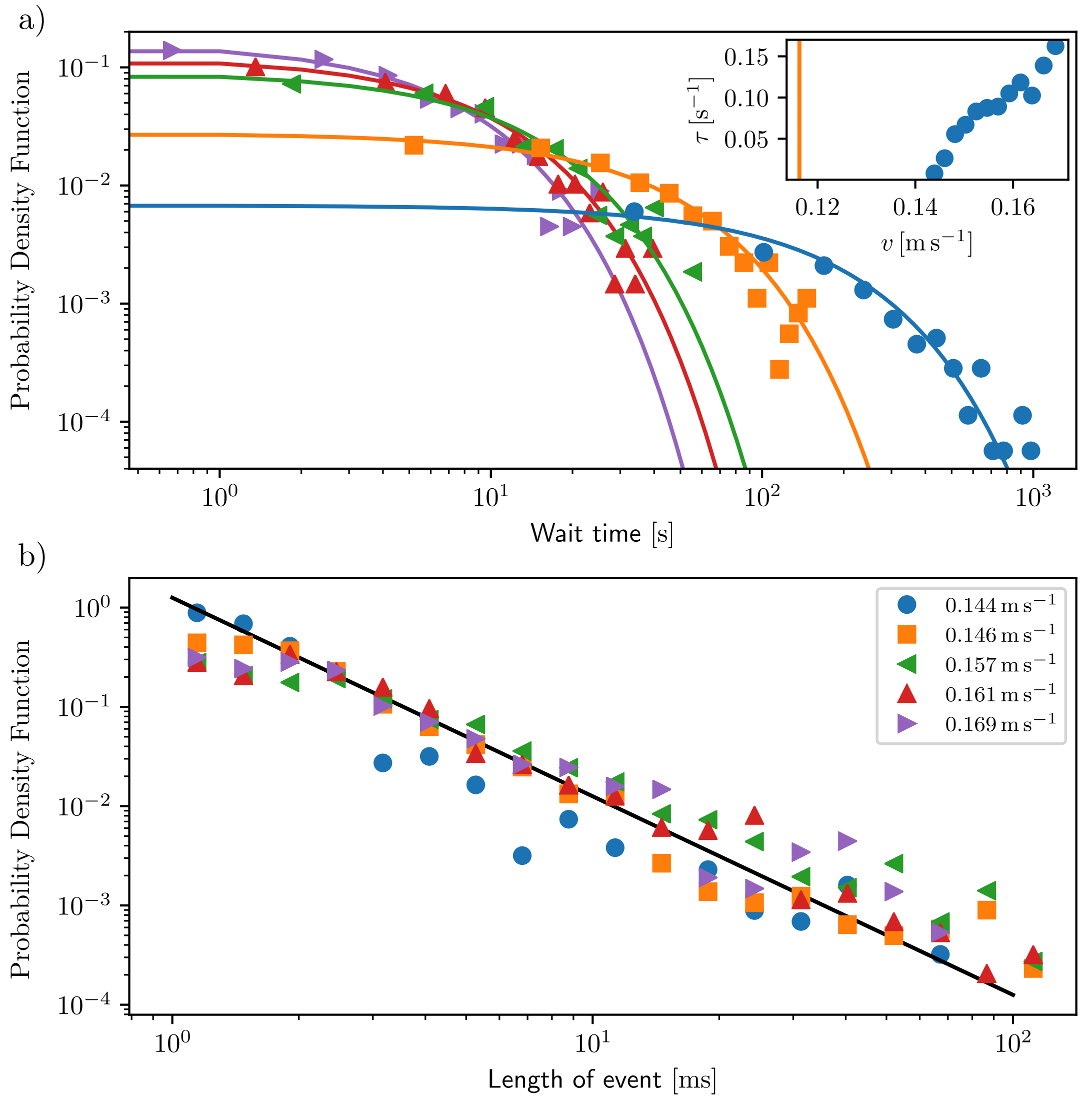

Fig. 5.5 (a) Normalised histograms for the wait time ($\delta_0\alpha_1$) frequency-shift events for several TF drives. The fit lines correspond to the function $\propto e^{-\tau t}$, where t is the wait time. Inset: Fitted τ as a function of the TF velocity. The orange line corresponds to the turbulent transition shown in Fig. 5.3. The event rate is clearly dependent on the TF drive, however does not intercept the x-axis at exactly the TF critical velocity. This implies that the TF experiences damping due to vortices before vortex emission is observed. (b) Normalised histogram of event length ($\beta_1\gamma_1$) for five values of the TF drive. There appears to be no significant difference in the event length distribution, with longer events less likely for all drives. The solid black line indicates a Density $\propto L^{-1/2}$, consistent with the idea that reconnection time depends on the distance to the nearest vortex, as discussed in Sec. 3.6.

likely for all TF powers. Since vortex reconnection by another vortex collision ends the event, it is logical to think that a lower vortex-line density would reduce the probability of this occurring. There appears to be a significant asymmetry between the time between events, and the length of events, i.e. despite the event rate decreasing to nearly zero, we do not have long-term stable vortex configurations whilst the TF is above v_c.

One interpretation of this inconsistency is that it is relatively unlikely for a passing vortex ring to become pinned, whereas the annihilation process can occurs more easily, possibly due to relative orientations of the vortex rings. Since we expect there to be an attractive force between nearby vortices (see Eq. (3.67)), this provides a potential mechanism for the asymmetry. An incoming vortex has to overcome a potential barrier to become pinned, however a pinned vortex will attract nearby vortexes for reconnection. In that case, event length is determined by the distance to the nearest vortex, rather than the global vortex line density. The solid black line indicates the model Density $\propto L^{-1/2}$, as discussed in Sec. 3.6, indicating that the distance to the nearest vortex remains relatively independent of TF drive. Such a result points towards significant inhomogeneity of the vortex tangle in the cell.

Using the fit presented in Fig. 5.3, we can estimate the power going to create vortex rings as $\dot{Q} = (dF/dv)(v^2/f_f)$, with the energy per unit length of a vortex is given in Eq. (2.39). The expected rate of vortex rings reaching the beam is therefore given by

$$\dot{N} = \left(\frac{dF}{dv}\right) \frac{r_r \rho_s \kappa^2 v^2}{8\pi f_f} \ln\left(\frac{2b}{\xi}\right) \frac{wt}{d^2}, \tag{5.1}$$

where d is the distance from the TF to the nanobeam, and r_r is the vortex ring radius. At the lowest TF power, given a ring radius $r_r = 50\,\mu\mathrm{m}$, we would expect to see an event rate of $\sim 10^{-3}\,\mathrm{s}^{-1}$, comparable to what is seen. However, at high TF power we would expect to see a rate $\sim 10^{-2}\,\mathrm{s}^{-1}$ however the observed rate is much higher. Such an observation implies that other processes contribute significantly to the event rate, not simply TF power. Since there is significant remnant vortices in the cell, the injected energy simply acts to destabilise existing pinned vortices, allowing the propagating vortex energy-density to significantly exceed that of the injected power. The picture is therefore complex and difficult to model precisely. Additional theoretical work in the area of vortex emission and propagation would prove invaluable in understanding our system.

5.3.3 Properties of Trapped Vortices

Since subsequent vortex ring collisions allow a trapped vortex to escape, in order to achieve a stable trapped vortex the TF must be off, however there must initially be significant vortex ring density in the fluid. After cooling the cryostat and running the TF above v_c, the TF was then switched off. A small mechanical disturbance to the cryostat then allowed a vortex to become trapped, and since the TF was off it could not escape. The mechanical disturbance pulses the system, destabilising existing vortices and creating a burst of vortex rings, but no continuous supply. The described method does not allow 100% reproducibility but appeared to allow the creation of novel vortex states which

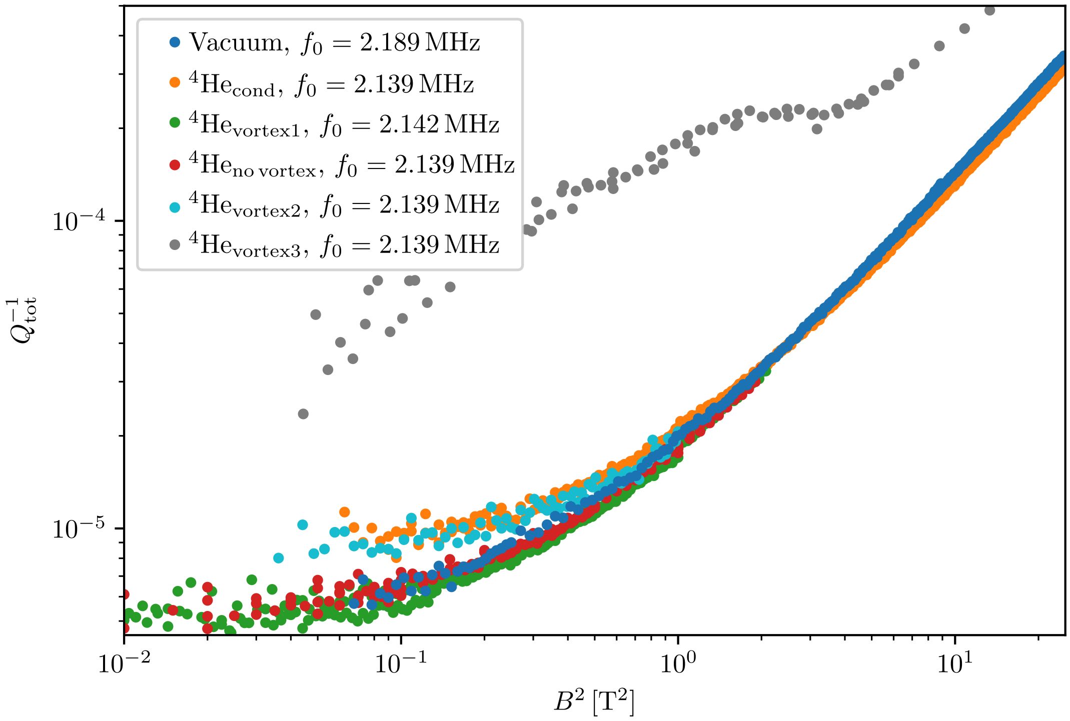

Fig. 5.6 Inverse Q-factor as a function of magnetic field for a 70 μm nanobeam, both in vacuum and under several vortex configurations. The key shows our interpretation of the vortex state, along with the fundamental mode frequency in such a configuration.

could exist indefinitely. The trapped vortex could then reliably be removed by further excitation of the TF, likely causing a vortex ring with opposite circulation to annihilate with the trapped vortex.

The measurements presented here were taken after a further thermal cycle from the previous data. Thermal contractions mean the fundamental frequency was shifted to $f_0 = 2.189\,\mathrm{MHz}$ in vacuum, and 2.139 MHz in ^{4}He. The frequency in the parallel trapped vortex state was found to be $2.139\,\mathrm{MHz} + 3\,\mathrm{kHz} = 2.142\,\mathrm{MHz}$.

To observe the fundamental dissipation in a given vortex configuration, we need to operate in a regime where the magnetomotive losses are low ($Q_{\mathrm{tot}}^{-1} > Q_{\mathrm{mm}}^{-1}$). Figure 5.6 shows the magnetic field dependence of the damping for the nanobeam operating in vacuum, and under several vortex configurations. The fundamental mode frequency in each state is shown in the legend. At high magnetic fields, all configurations converge to the same B^2 dependence, as expected from dominating magnetomotive damping, previously introduced in Sec. 3.4.3. The damping in vacuum is shown by the dark blue circles, reaching the level $Q_{\mathrm{int}}^{-1} = 8 \times 10^{-6}$ at the lowest fields, characterising the internal damping. The damping in vacuum is likely due to the thermoelastic effect, or possibly due to clamping losses.

The orange circles show the damping on the nanobeam in ^{4}He immediately after condensing, before the TF has been switched on. The damping in ^{4}He plateaus at a higher level than in vacuum, $Q_{\mathrm{cond}}^{-1} = 10^{-5}$, an effect we would typically attribute to simple dipole acoustical emission, as seen previously in Chapter 4, and initially introduced

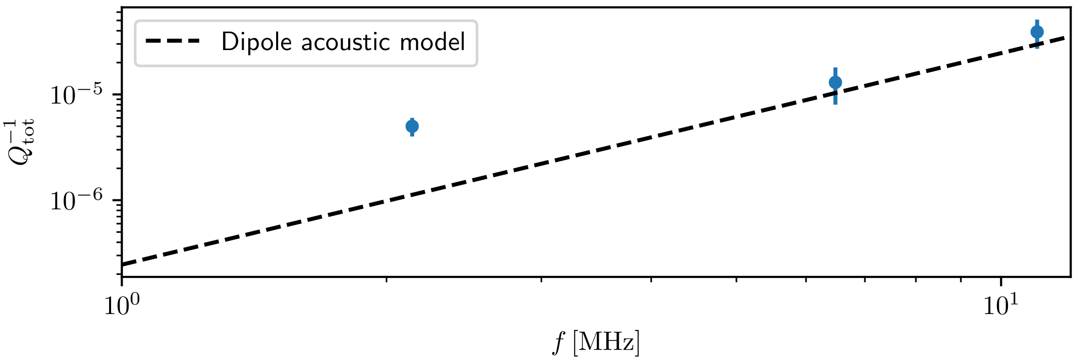

Fig. 5.7 Damping as a function of the resonance frequency for the 1st, 3rd and 5th harmonics in ^{4}He for a 70 μm nanobeam. The presented data was taken after annihilation of remnant vortices after the initial condensation. The dashed black line shows the theoretical fit using the dipole acoustic emission model presented in Eq. (3.55).

in Sec. 3.5.3. At this stage in the experiment, the only vortices in the cell should be remnant vortices produced by the Kibble-Zurek mechanism.

Upon performing the above procedure to trap a vortex along the nanobeam, by exciting the TF and mechanically disturbing the system, the field dependence was again measured, producing the green circles. Note, that the fundamental mode frequency in this state is that of the vortex state (2.142 MHz). Bizarrely, the damping in this state mimics that of the vacuum state suggesting that the acoustic emission is somehow reduced with the trapped vortex when compared with the initial condensation. The picture becomes even more curious upon annihilation of the trapped vortex state by excitation of the TF. Once the trapped vortex has been removed, we return to the fundamental frequency in ^{4}He (2.139 MHz), however the damping remains at the level seen in vacuum and in the parallel trapped vortex state, as shown by the red circles. This is a fascinating result, and implies a significant change to the nanobeam state from the initial condensation to after vortex annihilation.

Through successive vortex trapping procedures, with some quite low probability, we are able to recreate the conditions of the initial condensation as shown by the cyan circles. In this state, we observe a significant change in the damping however no significant change in the fundamental frequency. We therefore suggest that the additional damping observed initially after condensation is influenced by the presence of remnant vortices in the cell.

The reduced damping after annihilation is also seen in the nanobeam harmonics. Figure 5.7 shows the low magnetic field damping for the 1 st, 3rd and 5th harmonics as a function of their frequency, measured after trapping and removing a vortex from the surface. The dashed-black line shows a theoretical fit using Eq. (3.55) with the relevant parameters. The 3rd and 5th harmonic damping is now fairly well explained by the theoretical model, agreeing within 30% of each other. For the 1 st harmonic, the predicted damping from the mode is less than the intrinsic damping, and therefore not resolvable. This data is in direct contrast with the results presented in Chapter 4, Fig. 4.9(b), where same acoustic model appeared to significantly underestimate the damping. The presence of remnant vortices pinned to the nanobeam appears to significantly alter the damping experienced by the nanobeam. Such an effect could be related to additional acoustic emission due to the extra clamped mass, or potentially related to Kelvin-wave excitations on pinned vortices, as discussed in Sec. 3.6.

In some rare cases, we are able to generate highly usual trapped vortex states where the damping is much larger than due to the remnant vortices, as shown by the grey circles in Fig. 5.6. The field dependence of this state does not converge to the typical B^2 dependence at high field, suggesting that the additional damping due to the vortices is very large. In addition, several interesting features are present, including an apparent plateau at $\sim 1.5\,\mathrm{T}$. It is possible to imagine that such a state could involve multiple trapped vortices in a complex configuration. Further theoretical work is needed to fully understand the plethora of possible vortex trapping configurations that could exist in the condensate.

5.4 Conclusions and Outlook

We have demonstrated the use of a nanomechanical device as a high-speed detector for quantum rings in ^{4}He. Using a TF as a nearby source of turbulence we are able to demonstrate short frequency shifting events, which only occur when the TF is operating above its critical velocity for turbulence production. Using a novel MLA technique we were able to track the shift in frequency space, whilst maintaining time resolution. Using a theoretical model, we have shown that it is likely that such events correspond to the short term trapping of a single quanta of circulation along the length of the beam. The event ends when a vortex rings with opposite circulation interacts and annihilates. Our advanced method for detecting vortices could allow careful study of different vortex producers, or allow time-of-flight measurements to study propagation. By utilising a 2D array of nanomechanical devices, real-time images of turbulent tangles could be produced, a technique which could help bridge the theoretical gap between single vortices and large scale tangles.

By generating a large vortex line density but not operating the TF continuously, we were able to trap a single vortex to study its properties on longer timescales. We have demonstrated a significant difference in the damping experienced by the nanobeam from the initial condensation, to when a vortex is trapped along the beam, and after a vortex is released. Curiously, the damping in the vortex state and after the vortex release mirror that of the vacuum, whilst the initial condensation demonstrated higher damping. We believe this is the result of remnant vortices formed by the Kibble-Zurek mechanism contributing to the damping, a state we were able to recreate later in the experiment. As well as this state, several other configurations with extremely unusual damping properties were observed.

Our experiment demonstrates the ability to trap and study a single vortex in a multitude of configurations, some of which do not have a clear physical picture. Further work is needed to fully characterise all the different states which are observed, along with the probability of occurrence. Importantly, study is needed to fully understand how such states are created, and determine a reproducible method for creation of a desired vortex state. It is also clear that further theoretical study of the possible trapped vortex states is needed, which, combined with experiment results, has the potential to revolutionise our current understand of quantum turbulence.

Chapter 6

Experiments on Multimode Torsional Tuning Forks in ^{4}He

This chapter will discuss experiments probing superfluid ^{4}He using TFs with two well defined oscillation modes, demonstrating the potential advantages of these devices over conventional ^{4}He probes. Typical experiments involving oscillators utilise the same oscillation mode for both the emission and detection of the phenomena under study; the oscillator creates the excitation with the response measured by the same mode. Traditional quantum turbulence measurements using wires provide an example of this, where the velocity is increased until a characteristic increase in damping is observed. One advantage of this scheme is a spatial one, where vortices created by the oscillator are measured in the same location they are created, therefore maximising probe sensitivity. The disadvantage lies in the use of a single mode for detection. The force-velocity must first be characterised in vacuum to ensure signals are not a result of intrinsic effects. Using two modes on the same TF this problem can be bypassed by driving one mode to create vortices, while directly probing on the second mode. In this way, no calibration is needed since one can measure the absolute value of the damping using the second mode, while varying the velocity of the first mode.

This chapter describes experiments probing quantum turbulence, demonstrating the sensitivity of the torsional mode to excitations created by the flexural mode. We also investigate the unique acoustic properties of high frequency torsional TFs, accessing a new regime of sound-mode study in ^{4}He. Furthermore, we investigate torsional TFs and their quantum vortex production properties, determining their future potential as vortex ring emitters. Using two TFs mounted on the sample PCB we investigate whether the torsional mode could be used as a detector for vortices generated by another TF.

6.1 Samples

The devices measured in this experiment are commercially available quartz TFs with prong length $l = 1.61\,\text{mm}$, width $w = 0.22\,\text{mm}$ and thickness $t = 0.14\,\text{mm}$. The forks have a tine mass of $1.37 \times 10^{-7}\,\text{kg}$. An SEM of one such device is shown in Fig. 6.1. The devices have a well defined torsional oscillation mode at $393\,\text{kHz}$ and a flexural mode

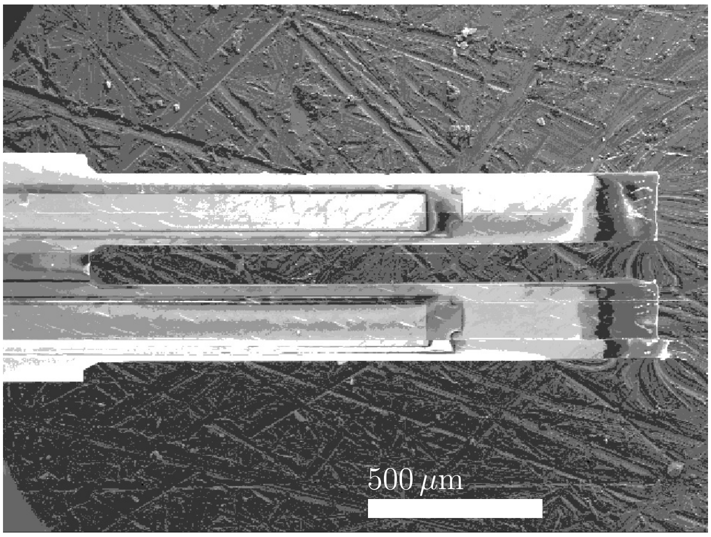

Fig. 6.1 SEM of a 76 kHz, 393 kHz, multimode quartz TF showing the two tines in detail, with corresponding scale bar shown.

at 73 kHz in vacuum. Quartz crystals are grown synthetically and then cut to yield the required geometry. The TFs tested were specially cut to yield a well defined, high Q torsional mode. Whilst typical 32 kHz TFs have a torsional mode, this is not well defined by the geometry and can vary significantly between samples.

6.2 Measurement Scheme

Two identical multimode TFs were investigated, both mounted on the same PCB, in order to investigate interactions between them. The TFs were mounted facing inwards into a metal casing to maximise the interaction strength between them, as shown in Fig. 6.2, with the distance between the opposing TF tines $\sim$ 5 mm. The devices are driven piezoelectrically, using an AC voltage supplied by a VNA, the response is recorded on the second port of the VNA as a function of frequency. The resultant Lorentzian is fitted to give the frequency, width and amplitude. By extension, two VNAs can be used to independently probe two modes on the same fork. Here, the velocity of one mode can be increased while independently monitoring the velocity of the second mode, allowing separation of the driving and probing data. A 5 dB summing amplifier was used to combine the signals and increase the drive we could supply to the forks. A detailed schematic is shown in Fig. A.6.

The experiments described in this chapter were performed in a custom-built glass cryostat with a base temperature of 1.2 K. The temperature was controlled by pumping on the helium bath, reducing the vapour pressure. In this way, the temperature was inferred via the pressure in the bath, converted using ^{4}He saturated vapour pressure data [106]. Further details of the cryostat used for these measurements can be found in App. A3.2.

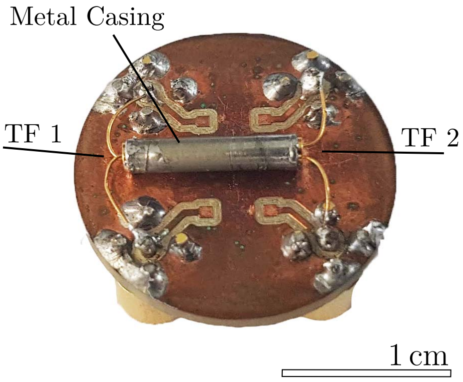

Fig. 6.2 Copper PCB with mounted TFs shown. Two forks were measured, mounted inside a metal casing such that interactions between them can be investigated.

6.2.1 Calibration using using Doppler Vibrometry

The measurement system was first calibrated so that the velocity of each oscillation mode could be independently calculated. This involves the measurement of the TF fork constant for each mode, as was introduced in Sec. 3.3 along with the equations of motion. Calibration was performed using a Laser-Doppler vibrometer (LDV) to optically measure the velocity, v, of the tine for a range of drive voltages, V. At the same time, the current, I, was measured as a function of drive voltage. The data is shown in Fig. 6.3. The calibration data for current and velocity remained linear over a large range of drive voltages allowing a linear fit to be performed, as indicated by the black-solid lines. The two datasets allowed us to convert between measured current and velocity by taking the product of the two fit gradients. This allowed the fork constant for the flexural mode to be determined as $a_f = 2.81 \times 10^{-6}\,\mathrm{C\,m^{-1}}$. For the torsional mode, the linear velocity projections as recorded by the Doppler-vibrometer were converted to an angular velocity using an effective radius, $r = \sqrt{t^2 + w^2}/2$, yielding a fork constant $a_t = 7.51 \times 10^{-10}\,\mathrm{C\,rad^{-1}}$. Electrical and optical measurements of the flexural fork constant have been previously shown to agree within 10% of each other [107], however such a comparison has never been performed for torsional modes. The peak velocity was also measured at several distances from the tip to study the way the probe interacts with the fluid. It was shown that the peak velocity for the flexural mode varies quadratically with distance from the tip, whereas the torsional mode varies linearly. It is thought that this may lead to a more uniform interaction with the fluid, as opposed to the flexural mode where the interaction is dominated by the high velocity of the tip.

The VNA used was calibrated by first replacing the TF with a $R = 38.2\,\mathrm{k\Omega}$ resistor, and the power output at the VNA set to $-20\,\mathrm{dBm}$, with this value of S_{21} set to $0\,\mathrm{dB}$. Since the current in this system is known, and $38.2\,\mathrm{k\Omega}$ is comparable to the fork resistance, this allows the current for any Lorentzian amplitude, A to be calculated as

$$I = \frac{V_{[-20\,\mathrm{dBm}]}}{R} 10^{\frac{(P_{\mathrm{out}}+20)}{20})} A, \tag{6.1}$$

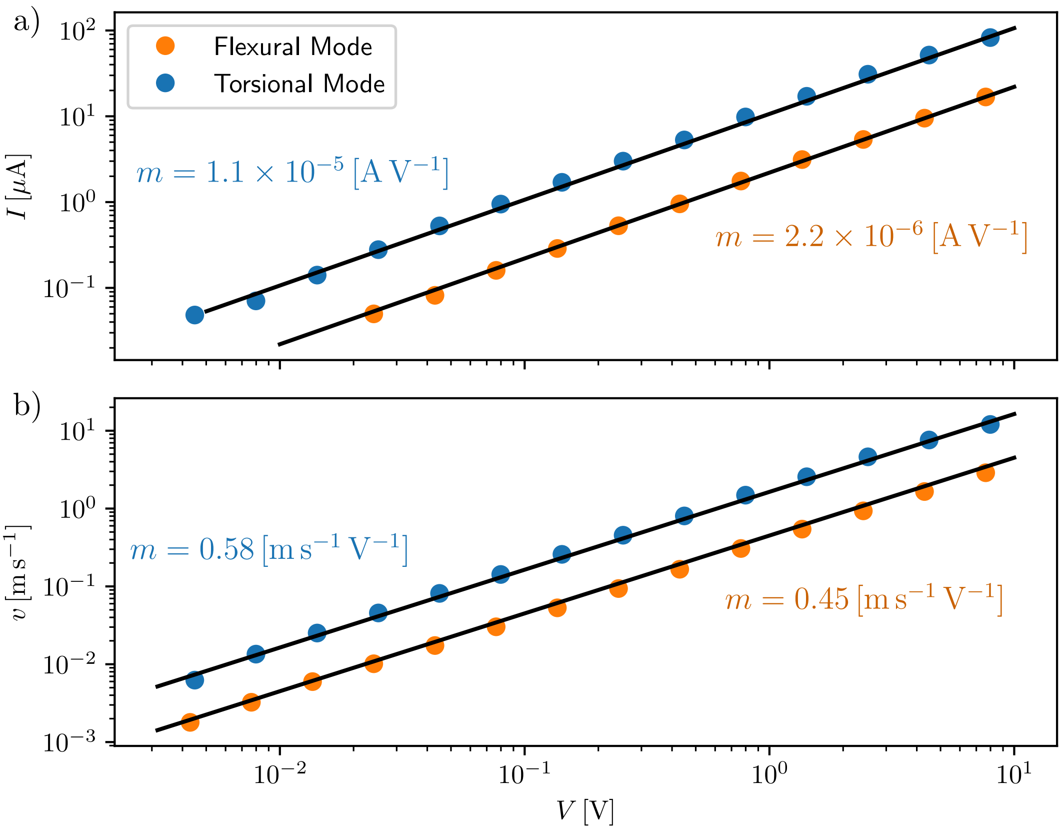

Fig. 6.3 (a) Voltage-current characteristics measured electrically, and (b) voltage-velocity response measured optically using a laser-Doppler vibrometer, for two modes of a quartz TF. m refers to the gradient of the fit lines indicated. Using these fits, the fork constant for each mode can be calculated.

where $V_{[-20\,\mathrm{dBm}]}$ is the voltage output from the VNA at $-20\,\mathrm{dBm}$ and P_{out} is the power output for this measurement in dBm. The velocity can then be calculated for any current by comparison to optical measurements. The method described takes into account all attenuators and amplifiers, as well as impedance mismatches in the measurement circuit, making it a versatile method for current calculations.

6.3 Results

Here we outline the main results obtained using torsional TF as probes of superfluid ^{4}He. The results include the first measurements operating a torsional TFs in both normal and superfluid ^{4}He, with the drawbacks of the probe highlighted. We present a novel detection scheme, using two modes on the same TF, one mode as an actuator and one mode as a detector.

6.3.1 Vacuum

The TFs were first measured in vacuum at room temperature to characterise their intrinsic damping. These measurements yielded the Q-factor of the flexural and torsional mode

	Vacuum f_0 [kHz]	Vacuum Δf [Hz]	^{4}He f_0 [kHz]	^{4}He Δf [Hz]
Flexural	76.197	2	74.802	4
Torsional	393.063	7	388.26	70

Table 6.1 Table showing vacuum and ^{4}He at 1.2 K values for the flexural and torsional modes of a multimode TF. Vacuum values are taken at 300 K.

to be 3.7×10^4 and 5.5×10^4 respectively. In this regime, the damping is governed by thermoelastic losses as described in Sec. 3.4.2. Measurements at low temperatures in vacuum would likely reach the limit imposed by clamping losses, however this measurement was not performed. Figure 6.4(a) shows the peak velocity as a function of the driving force for the flexural mode, while Fig. 6.4(b) shows angular velocity as a function of the torque for the torsional mode. Both modes demonstrate a linear response up to several $\mathrm{m\,s^{-1}}$ in vacuum, with the torsional mode deviating slightly above this due to inherent non-linearities. A table summarising the values in vacuum and in ^{4}He is shown in Table 6.1.

6.3.2 Response of Multimode Fork in ^{4}He

Upon submerging the oscillators in ^{4}He at 1.2 K the damping on the torsional mode increased significantly with the Q-Factor decreasing to 10^3. High frequency oscillators have been previously shown to emit acoustic waves in ^{4}He. The acoustic emission for TFs follows $Q_{\mathrm{ac}}^{-1} \propto f_0^5$ where f_0 is the central frequency, described in detail in Sec. 3.5.4. Due to the relatively high frequency of the torsional mode we should observe strong acoustic emission leading to increased damping when submerged in ^{4}He. In addition, due to the unique geometry of the torsional mode it may act as an octupole acoustic emitter, with an even steeper power law.

We therefore attribute the significant increase in the damping of the torsional mode to this effect. In addition, sidebands are observed in the frequency response, as shown in Fig. 6.5. The sidebands result from the presence of acoustical modes in the experimental volume, leading to standing resonances of acoustic waves. The scale of these modes can be calculated from the frequency and speed of sound in ^{4}He using $c = \nu\lambda$. Estimations put λ at the order of 0.4 mm which is comparable to the spacing between the fork legs. For this reason, conventional confined geometries, such as an enclosed cylinder [108], would not fully suppress these high frequency modes. Furthermore, with knowledge of the inter-prong spacing $d = 113.5\,\mu$m, this allows the calculation of the first-sound velocity to a precision of $0.1\,\mathrm{m\,s^{-1}}$.

The flexural mode also saw an increase in damping of a factor of ~ 2, and otherwise behaved as expected, demonstrating a transition to a turbulent regime at a velocity of $70\,\mathrm{cm\,s^{-1}}$, characterized by a ‘kink’ on a force-velocity plot, as shown in the solid orange points in Fig. 6.4(a). The behaviour of a TF in the turbulent regime is described in Sec. 3.5.6, and the value of the critical velocity is consistent with that measured in previous turbulence experiments involving TFs [89]. Despite moving at a velocity of several tens of $\mathrm{cm\,s^{-1}}$ the torsional mode had no obvious transition to a turbulent regime,

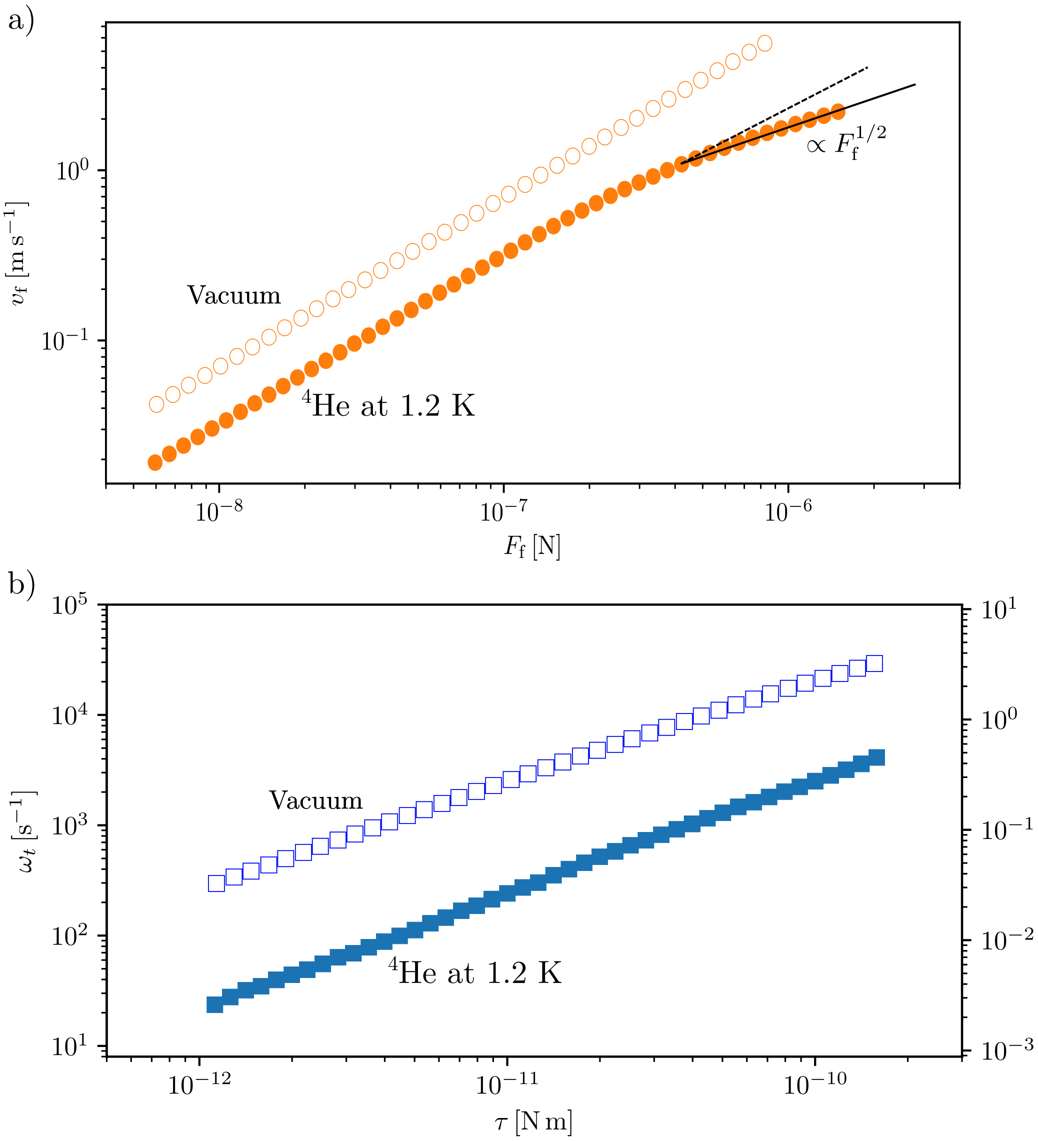

Fig. 6.4 (a) Peak prong velocity as a function of driving force for the flexural mode of a TF in vacuum and ^{4}He at 1.2 K. In vacuum the TF demonstrates linear behaviour with the damping dominated by internal losses. In ^{4}He at 1.2 K losses are higher due to additional damping in the fluid. The transition to the turbulent regime is demonstrated by the change in gradient occurring at 70 cm s^{-1}. (b) Peak prong velocity as a function of torque for the torsional mode of a TF in vacuum and ^{4}He at 1.2 K. The high damping in ^{4}He is a result of strong acoustical (first-sound) emission in the liquid, due to the high frequency of this mode. No turbulent transition is observed up to an angular velocity of 3×10^3 rads^{-1}.

as shown in solid blue squares in Fig. 6.4(b). The lack of a turbulent transition could be due to the higher damping reducing the attainable velocity, or alternatively the high frequency of the torsional mode may be suppressing the critical velocity. Previous work has shown the critical velocity for the onset of turbulence to scale with $\sqrt{f_0}$, suggesting that the critical velocity for turbulence production may be close to 1 ms^{-1}. Given the limits on the applied torque, these high velocities were not achieved in these measurements.

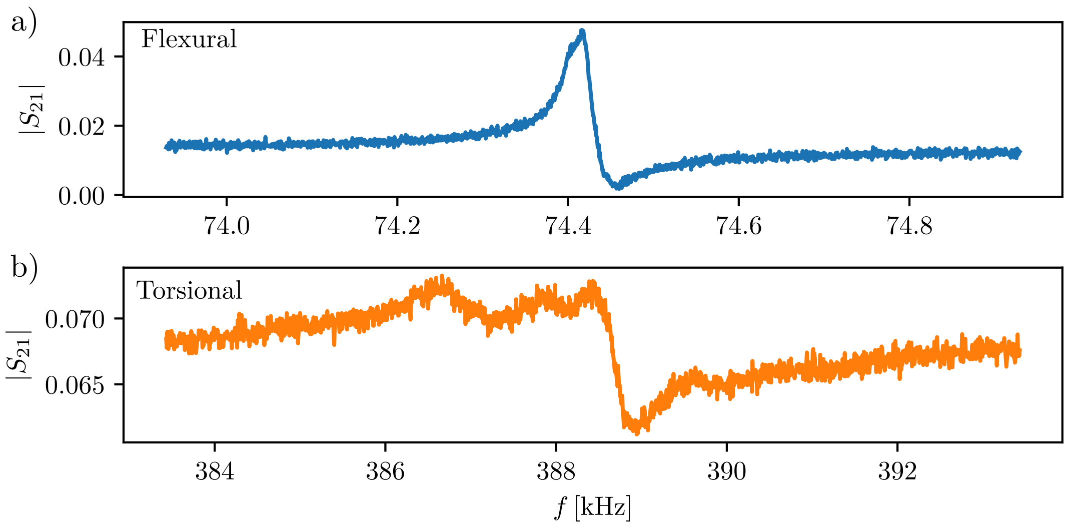

Fig. 6.5 Frequency response at 1.5 K in bulk ^{4}He for the torsional mode of a quartz TF. The Q-factor is of the order 10^3 due to dominating acoustic emission in the condensate. In addition are the presence of acoustical sidebands due to cavity resonances set up in the experimental volume.

The inherent linearity present the torsional mode as an ideal detector for excitations produced by the flexural mode. The results of this are discussed in the next section.

Due to the varying speed of sound in ^{4}He, as discussed in Sec. 2.1.1, the previously discussed acoustic sidebands have significant temperature dependence, shown in Fig. 6.6. As the temperature is varied around the T_λ the sideband resonances shift from high frequency to low frequency. The high number of acoustic modes is indicated by the number of diagonal lines moving through the TF response. This is a result of the complex geometry of the TF. A comparison is shown to the flexural mode where a single resonance moves to higher frequency below the T_λ, accurately described by Sec. 3.5.1. The flexural mode demonstrates the characteristic response of a resonator where the effective mass is decreasing due to the reducing normal fluid fraction, as has been demonstrated in numerous previous experiments. The sensitivity of the torsional mode to superfluid excitations is limited due to high acoustic damping, however the presence of sidebands pose a more significant technical challenge for using the torsional mode for detection. By operating at the lowest temperatures 1.2 K we can tune the acoustic sidebands away from the resonance frequency, opening the possibility for turbulence detection.

6.3.3 Multimode Detection of Quantum Turbulence

A TF with two well defined modes with a large frequency separation opens the possibility for separating the driving and detection between the modes. This idea was implemented as a detection mechanism for quantum turbulence produced in superfluid ^{4}He at 1.2 K. Experiments already presented with the flexural mode of the TF demonstrated a clear transition to a turbulent regime at 70 cm s^{-1}, shown again by the orange circles in Fig. 6.7. Monitoring the torsional mode whilst performing the same measurements demonstrated

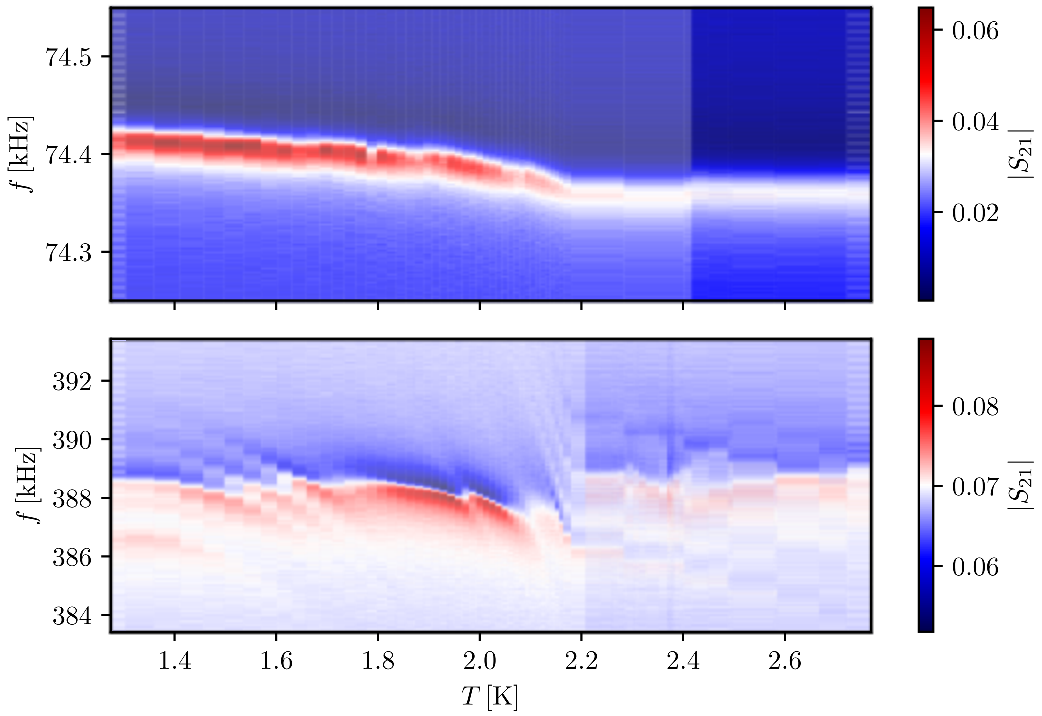

Fig. 6.6 (a) Temperature dependence of the frequency response for the flexural mode in the vicinity of T_λ. The colour axis represents $|S_{21}|$ transmission measurements. The response follows the expectation for an oscillator with a decreasing effective mass due to the decreasing normal-fluid fraction below the T_λ. (b) Temperature dependence of the frequency response for the torsional mode. The peak is significantly broadened when compared with vacuum and off-resonance sidebands are present. The additional damping is evidence for acoustic emission as a result of high frequency oscillations. The sidebands move with temperature due to the varying speed of sound in ^{4}He, made apparent from the presence of diagonal lines representing resonances moving from high to low frequency.

that the torsional mode was indeed sensitive to the fluid flow from vortices generated by the flexural mode. The data from this experiment is shown in Fig. 6.7, where F_f refers to the force being applied to the flexural mode.

The transition to turbulence is evidenced by the shift from constant velocity to a decreasing velocity as the amount of drag on the TF increases. Importantly, the transition occurs at the same force corresponding the onset of turbulence in Fig. 6.7. Measurement of this type have the advantage that they do not rely on a previous calibration of the detection mode. Our approach encounters difficulties at very high drives due to a transition away the linear regime. Here, cross-talk between different resonant modes become non-negligible, preventing this type of experiment.

6.3.4 Coupling two Tuning Forks with Quantum Turbulence

To investigate coupling between the two TFs, the velocity of the first TF was increased and the response of the second TF was measured. Previous measurements showed that the torsional mode did not appear to nucleate turbulence. Here we aimed to demonstrate turbulence nucleation by the torsional mode by bombardment with vortex rings created

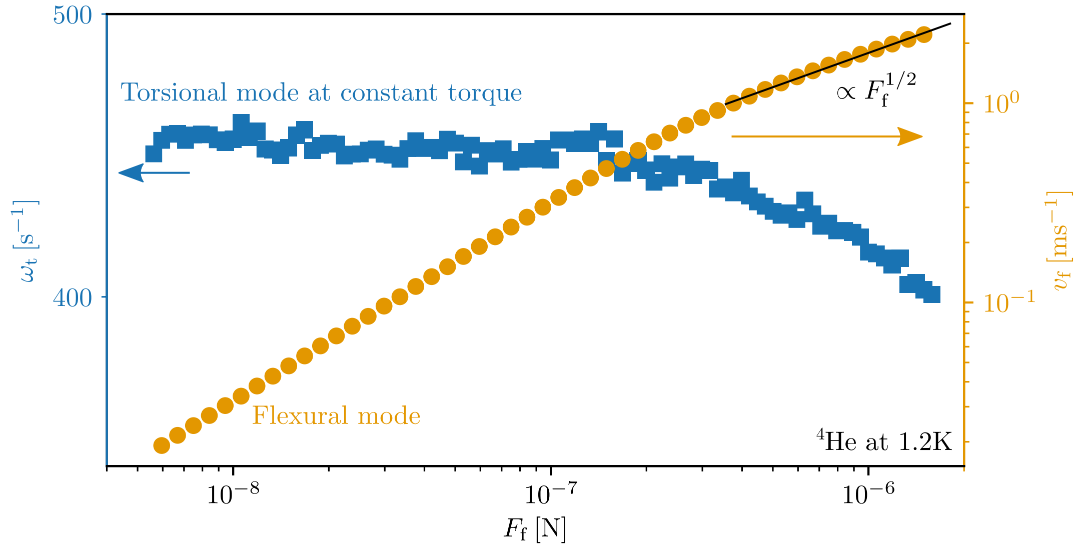

Fig. 6.7 (Orange) Force response for the 76 kHz flexural mode in bulk ^{4}He at 1.2 K. A clear transition to a turbulent regime is observed where the slope decreases, corresponding to increased damping. (Blue) The velocity of the torsional mode as a function of the force on the flexural mode. At the same value of force corresponding to the critical velocity on the flexural mode a transition to higher damping occurs on the torsional mode. It is apparent that the torsional mode is sensitive to the flow from vortices generated by the flexural mode.

by the flexural mode of another TF. It was thought that if the torsional mode was operating in a metastable regime at high angular velocity that nearby vortices can trigger production. Such effect have been previously observed in vibrating wires, which were operated as a single-shot detector for vortices [32]. Our results demonstrated no significant change in the torsional resonance even for very large drives on the other TF, suggesting that even in the presence of significant vortex-line density, the torsional mode does not nucleate turbulence. Alternatively, our results suggest damping on the torsional mode was too large meaning subtle effects could not be resolved.

6.4 Conclusions and Outlook

Our work presents the first measurement of torsional TFs in bulk liquid ^{4}He from 4.2 K to 1.2 K. Notably, the torsional mode experienced high damping in liquid compared to vacuum as a result of acoustic (first sound) emission. This is further evidenced by the presence of sidebands in the frequency response, a product of internal acoustic resonances in the sample space. High levels of acoustic emission could be addressed through the development of lower frequency torsional modes, by using longer forks or more flexible materials. It has been demonstrated that the high oscillation frequency leads to a high critical velocity for the onset of turbulence; the turbulent transition was not observed in the torsional mode up to an angular velocity of 3×10^3 rad s^{-1}, corresponding to a linear velocity of 70 cm s^{-1}.

The torsional mode has been operated as a detection mode for turbulence created on the flexural mode, a useful technique since it allows uncalibrated probing without the introduction of spatial separation. The torsional mode velocity was demonstrated to decrease at the same point at which the flexural mode transitioned to a turbulent regime, suggesting that the detection mode is sensitive to the flow from vortices created by the generator mode. The method presented could be further improved by using a detection mode with lower acoustic damping, whilst maintaining the large frequency separation. Finally, using two TFs separated in space, we show that the torsional mode did not appear to be sensitive to vortices created by a nearby fork. To a degree such a result is not surprising since, until now, similar experiments have only been demonstrated where the detector is operating in a metastable turbulent regime operating as a latching switch [32].

The experiments shown here thrust high-frequency torsional oscillators from a novelty, into the realm of useful low-temperature probes. However, our results further highlight the limits imposed from using high-frequency devices in liquid ^{4}He due to dominant acoustic emission in the liquid, ultimately limiting the device sensitivity. The results from this chapter are presented in publication IV.

Part II

Field-Effect in Superconducting Nanoconstrictions

Chapter 7

Introduction

Superconductors are fascinating materials which exhibit zero electrical resistance, and perfect diamagnetism, when cooled below a certain temperature. The microscopic mechanism by which superconductivity can occur was first put forward by Bardeen, Cooper and Schrieffer, and is known as BCS theory [109]. Conventional BCS theory predicts the behaviour of a piece of superconducting metal to be independent of the applied electrostatic field. This is due to the exponential suppression of the electric field inside a superconductor over a length scale, known as the London Penetration depth [110]. However, some very recent publications claim that an electric field *can* penetrate into superconductors with clear, measurable effects [111–114], which we will call the 'superconducting field-effect'. The authors claim that, under certain conditions, electrostatic fields can influence the pairing mechanism in a superconductor, in direct contrast to BCS theory [114]. In this part, we will attempt to understand how the alleged superconducting field-effect can be reconciled with conventional BCS theory.

The publications ([111–113]) have shown field-effect control of supercurrent, along with full supercurrent suppression in all-metallic 1D channels. The studies have also utilised this effect to realise an all-metallic Josephson field-effect transistor (JoFET) consisting of a gated Dayem bridge, and to demonstrate a field-effect superconducting quantum interference device (SQUID). Despite these developments, a mathematical description pointing to the source of the field-effect remains elusive. It has not been confirmed whether this effect is an intrinsic property of the superconductor, or some known phenomena manifesting as a field-effect in specific geometries. The cited work has demonstrated this effect in several different superconductors (Al, V, Ti) and multiple substrates (Si, SiO_2, Al_2O_3) [111–113].

The realisation of entirely metallic, tunable, Josephson junctions elements could have significant implications for the field of quantum technology. Existing superconducting qubit technology relies on shadow deposition of metal to form tunnel junctions, also known as the Dolan-bridge technique. Typically, a layer of resist is used as a mask, with two deposition layers at opposing angles to form the overlap, with an in-situ oxidisation in-between. Tunable non-linear inductors in the form of gated-Dayem bridges could greatly simplify fabrication procedures, since only a single lithography step would be required. In addition, if modulation could be performed at GHz frequencies, one could realise all-metallic parametric amplification, attenuation and generation. Slower tunability would be useful in the field of single-photon detection, for the ability to use a high quality, narrow band detector over a larger frequency range.

We will present a new approach to investigate the origin of the apparent superconducting field-effect, by coupling a gated-Dayem bridge Josephson junction, to a superconducting resonator operating at GHz frequency. Until now, measurements have been performed in the quasi-DC limit, measuring the differential resistance across a single sample. Fast readout at a single-frequency allows the investigation of the field-effect phenomena at much shorter time-scales than previously possible. Furthermore, a single feedline with multiplexed resonators allows the characterisation of multiple samples on a single chip.

Chapter 8 will introduce the fundamental properties of superconductors, as well as the Josephson effect, formalise transmission line theory and introduce our measurement principles. Chapter 9 presents our investigations into gated-Dayem bridges, and conclude by proposing a physical consistent theory to the origin of the superconducting field-effect, without recourse to any new physics.

Chapter 8

Superconductivity

Superconductivity is the name given to the extraordinary phenomena in which a current is able to flow through a material without any electrical resistance. Superconductivity was first observed in 1911 by H.K. Onnes when he cooled mercury to liquid helium temperatures and noticed a sharp drop in the DC electrical resistivity [115]. He called the temperature at which this occurred the critical temperature, T_c. It quickly became evident that the resistance does not just drop, it completely vanishes, something that theoretical physics was unable to explain at the time. As cooling techniques improved, superconductivity was observed in many other materials, including vanadium, niobium and lead.

In 1933, the first observations of the Meissner effect were observed, where a material is able to completely expel an external magnetic field from its interior, when cooled through the superconducting transition [116]. In this state, the material is acting as a perfect diamagnet, in which the magnetic susceptibility, $\chi = -1$. At first, this was thought to be an unrelated phenomena however, it was shown to be another manifestation of the same process. The Meissner effect clearly distinguishes between a perfect conductor and a superconductor, as shown in Fig. 8.1.

Superconductivity can be destroyed by a large magnetic field, known as the critical field, H_c, where the relationship between the critical quantities given by

$$H_c(T) = H_c(0)\left[1 - \left(\frac{T}{T_c}\right)^2\right], \tag{8.1}$$

where, T, is the temperature, and $H_c(0)$ is the critical field at zero temperature.

The first theory attempting to describe the process of superconductivity was put forward by Ginzburg and Landau in 1950 [117]. Using a macroscopic approach, they predicted the quantization of magnetic flux, and calculated the length scale over which a magnetic field can penetrate into a superconductor - known as the London penetration depth, λ, which will be discussed more in Sec. 8.1. The first microscopic theory of superconductivity was not put forward until 1957, when Bardeen, Cooper, and Schrieffer published what became known as BCS theory. In BCS theory, the charge carriers are not individual electrons as in conventional materials, but pairs of electrons known as Cooper pairs [109]. It was understood that superconductivity was likely related to Bose-Einstein

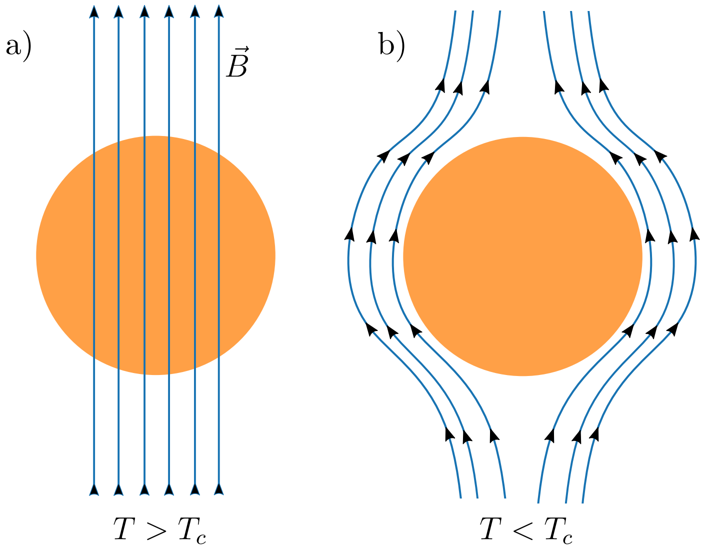

Fig. 8.1 (a) In a perfect conductor, a magnetic field can penetrate into the material. (b) When cooled through the superconducting transition, the applied magnetic field is completely expelled due to the Meissner effect.

condensation – similar to what was observed in superfluid ^{4}He – however due to the Pauli exclusion principle, with electrons being fermions, it was known that they could not simply condense.

To resolve this, a Cooper pair is formed consisting of two electrons which are attracted as a result of the electron-phonon interaction. They then act as a composite boson with integer quasi-spin allowing a condensate to form. When the Cooper pairs condense, they form a single quantum state with wavefunction $\psi = \sqrt{n}e^{i\varphi}$, where n is the Cooper pair density and φ is the superconducting phase. The observable of the system, the Cooper pair density, is then given by $n = \psi\psi^*$. In this configuration, the density of states gives rise to an energy gap, 2Δ, between the condensate and single particle excitations, as shown in Fig. 8.2. The superconducting energy gap is formed symmetrically in 3D k-space around the Fermi energy, E_F, and at $T = 0$ is related to the critical temperature by the pre-factor $\Delta_0 = 1.76k_\mathrm{B}T_c$. At higher temperature, the energy gap decreases becoming zero at the critical temperature, qualitatively consistent with Eq. (8.1). At any finite temperature, there exists a population of thermally excited quasiparticles which result in AC impedance in the superconductor. The thermal quasiparticles in a superconductor can be considered analogous to the normal-fluid fraction in a superfluid.

8.1 Surface Impedance

Here we will consider the behaviour of superconductors under the influence of electromagnetic fields, in order to understand their role in quantum circuits. In a normal metal, the relationship between the current density, $\mathbf{J_n}$, and an AC electric field, $\mathbf{E}$, can be expressed by the local Ohms law, where the conductivity for electrons is given by Drude's model [118]

$$\mathbf{J_n} = \sigma(\omega)\mathbf{E} = \frac{\sigma_\mathrm{dc}}{1 + i\omega\tau}\mathbf{E}, \tag{8.2}$$

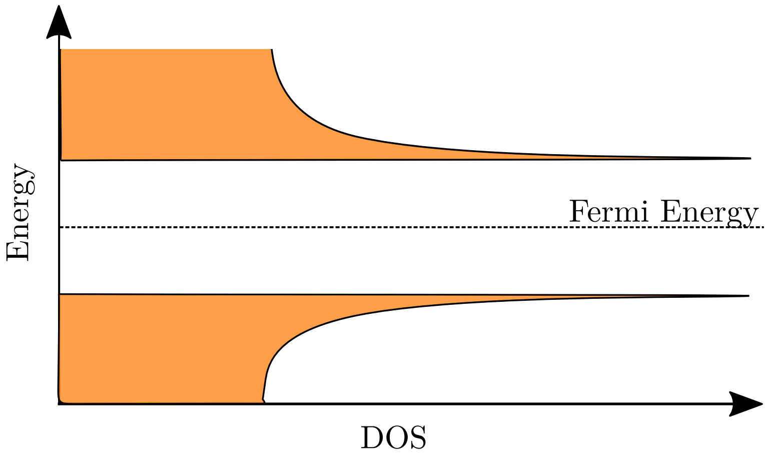

Fig. 8.2 Density of states (DOS) for a superconducting material, with the Fermi-energy shown. The gap is given by $E = 2\Delta$.

where σ_{dc} is the DC conductivity, ω is the AC field frequency and τ is the scattering time. The second term in the denominator arises from the phase lag between the current and electric field due to the inertia of the charge carriers. In normal metals, the scattering time is very small resulting in largely resistive behaviour. In this form, Ohm's law can only be used when the mean free path is short enough such that the electric field can be considered approximately constant in this region. Expressions which require such an approximation are known as 'local' relationships. The generalised non-local relationship was proposed by Chambers [119]

$$\mathbf{J_n} = \frac{3\sigma_{\mathrm{dc}}}{4\pi l} \int_V \frac{\mathbf{R}\left[\mathbf{R} \cdot \mathbf{E}\right] e^{-R/l}}{R^4} d\mathbf{r}, \tag{8.3}$$

where l is the mean free path, and the V represents the entire volume of the sample. Therefore $\mathbf{R}$ is a vector from the current location to the field-location, with differential $d\mathbf{r}$. Chambers used this to explain the anomalous skin depth in normal metals, the observation of an increased skin-depth in metals with very long mean free paths.

Superconductors demonstrate zero DC resistance due to the ability for Cooper pairs to move though the material without scattering ($\sigma_{dc} = \infty$), however demonstrate non-zero AC impedance due to the Cooper pair inertia [120]. As previously introduced, an electromagnetic field can penetrate into a superconductor over the London penetration depth, λ. Using a superfluid analogy, the current in a superconductor can be thought of as a sum of the surface normal currents, and the bulk supercurrent ($\mathbf{J} = \mathbf{J_n} + \mathbf{J_s}$). The relationships between the electromagnetic fields and the supercurrent densities were famously expressed by London [121] in his two local equations:

$$\frac{\partial \mathbf{J_s}}{\partial t} = \frac{\mathbf{E}}{\mu_0 \lambda^2}, \tag{8.4}$$

$$\nabla \times \mathbf{J_s} = -\frac{1}{\lambda^2}\mathbf{H}, \tag{8.5}$$

where **E** and **H** are the vectors representing the electric and magnetic fields respectively. The mean free path can depend strongly on the purity of the superconductor, with higher-purity samples having considerably longer mean free paths. A large mean-free path reduces the accuracy of local relationships, such as the London equations. This led Pippard [122], inspired by the work of Chambers, to propose the generalised non-local relationship for the supercurrent density

$$\mathbf{J_s} = -\frac{3}{4\pi\xi_0\lambda^2}\int_V \frac{\mathbf{R}\left[\mathbf{R}\cdot\mathbf{A}\right]e^{-R/\xi}}{R^4}d\mathbf{r}, \tag{8.6}$$

where **A** is the magnetic vector potential, ($\mathbf{H} = \nabla \times \mathbf{A}$) and ξ is the superconducting coherence length. The zero temperature coherence length is given by

$$\xi_0 = \frac{\hbar v_F}{\pi\Delta_0}, \tag{8.7}$$

where Δ_0 is the superconducting gap at zero temperature and v_F is the Fermi velocity. The coherence length is often thought of as the minimum size of a Cooper pair as allowed by the uncertainty principle, an important quantity in the construction of quantum limited devices shown in the next section.

8.2 Josephson Effect

In 1962, 51 years after the discovery of superconductivity, Brian Josephson made the theoretical prediction that two superconductors coupled by a ‘weak link’, would allow a zero-voltage current of Cooper pairs to flow between them [123]. Such a structure is known as a Josephson junction. He noted that the weak link in this system must be such that the quantum mechanical wavefunctions of the two superconductors overlap in their exponential decay. In reality, this requires the separation to be comparable to the superconducting coherence length, ξ_0, given in Eq. (8.7). The weak link forming a Josephson junction can take several forms. The most commonly used configuration is the superconductor-insulator-superconductor (SIS), however superconductor-normal metal-superconductor (SNS), superconductor^1-superconductor^2-superconductor^1 (SS’S), and superconductor-constriction-superconductor (ScS) have also been demonstrated. A Josephson junction consisting of a constriction less than the coherence length is also known as a *Dayem bridge.*

The tunnelling phenomena in such a system gives rise to two effects, known as the DC and AC Josephson effects. The DC Josephson effect states that the tunnelling current, I, through the weak link depends on the phase difference between wavefunctions of the two superconductors, φ, such that

$$I = I_c \sin\varphi, \tag{8.8}$$

where I_c is the maximum supercurrent that can flow through the junction, known as the critical current. Above this current, the junction switches to the resistive branch where no supercurrent flows. The AC Josephson effect relates the voltage across the junction

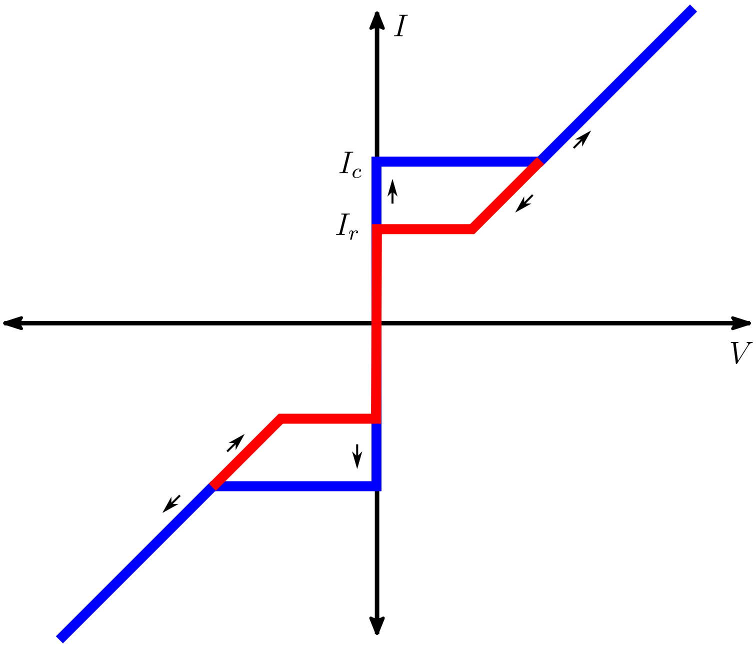

Fig. 8.3 Current-Voltage characteristics of a typical Josephson Junction. There is a zero voltage supercurrent branch, and a resistive branch above I_c. Decreasing from the resistive branch requires a lower current of I_r before transitioning to the supercurrent branch due to thermal effects.

to the time derivative of the phase by

$$V = \frac{\hbar}{2e}\frac{d\varphi}{dt}. \tag{8.9}$$

Importantly, a Josephson junction accumulates energy from the tunnelling Cooper-pairs, known as the Josephson energy, and is given by

$$E_{\mathrm{J}} = \frac{\Phi_0 I_c}{2\pi}(1-\cos\varphi), \tag{8.10}$$

where $\Phi_0 = h/(2e)$ is the flux quanta. This results in a non-linear Josephson inductance, L_{J}, obtained by differentiating Eq. (8.8), given as

$$L_{\mathrm{J}} = \frac{\Phi_0}{2\pi I_c \cos\varphi}. \tag{8.11}$$

The current-voltage characteristics for a Josephson junction are shown in Fig. 8.3. A zero voltage supercurrent branch is observed, extending to a maximum of the critical current, I_c. Above I_c, the junction becomes normal, and exhibits resistive behaviour. Decreasing the current from the resistive branch, one must reach a lower current, known as the retrapping current, I_r, to return to the supercurrent branch. The disparity between I_c and I_r is the result of thermal effects caused by driving a current in the normal-state resistance.

Due to changes in the superconducting gap with temperature, $\Delta(T)$, the critical current of a Josephson junction also depends on temperature as [110]

$$I_c(T) = \frac{\pi}{2}\frac{\Delta(T)}{eR_\mathrm{N}}\tanh\left(\frac{\Delta(T)}{2k_\mathrm{B}T}\right), \tag{8.12}$$

where R_N is the normal-state resistance of the Josephson junction. The strong dependence of the critical current on temperature is important, since any measured field-effect must be distinguished from simple changes in temperature.

Two Josephson junction can be combined into a loop geometry, such that an area is enclosed by the superconductor. Such a device is known as a Superconducting Quantum Interference Device (SQUID), and creates interference between the tunnelling supercurrents through the two junctions. The total supercurrent through such a device is then a function of the magnetic field in the area enclosed by the loop.

8.3 Superconducting Transmission Lines

To study the high-frequency behaviour of electrical elements, such as Josephson junctions, distributed microwave transmission lines are typically used. Transmission lines can take several geometries: microstrips, where the ground plane is below the structure, and coplanar waveguides (CPW), where the ground plane and centre conductor are in the same plane. A schematic of a CPW with the equivalent electrical representation for a single unit, is shown is Fig. 8.4.

Similar to a coaxial cable, microwave frequency photons give rise to transverse electromagnetic (TEM) waves and can be represented by infinitesimally short segments ($dz \to 0$), each with a distributed resistance (Rdz), inductance (Ldz) and capacitance (Cdz). The voltage, V and current, I at a position, z, along the transmission line can be written as

$$V(z) = V^+e^{-\gamma z} + V^-e^{\gamma z}, \tag{8.13}$$

$$I(z) = I^+e^{-\gamma z} + I^-e^{\gamma z}, \tag{8.14}$$

where $V^\pm$ and $I^\pm$ represent the forward and backward components of the propagating voltage and current components. Here, γ is the complex propagation constant

$$\gamma = \sqrt{(R + i\omega L)(i\omega C)}. \tag{8.15}$$

The propagation constant tells us the rate at which phase changes occur along the transmission line. The complex impedance of the transmission line, $Z = V/I$, is

$$Z = \sqrt{\frac{L}{C}}, \tag{8.16}$$

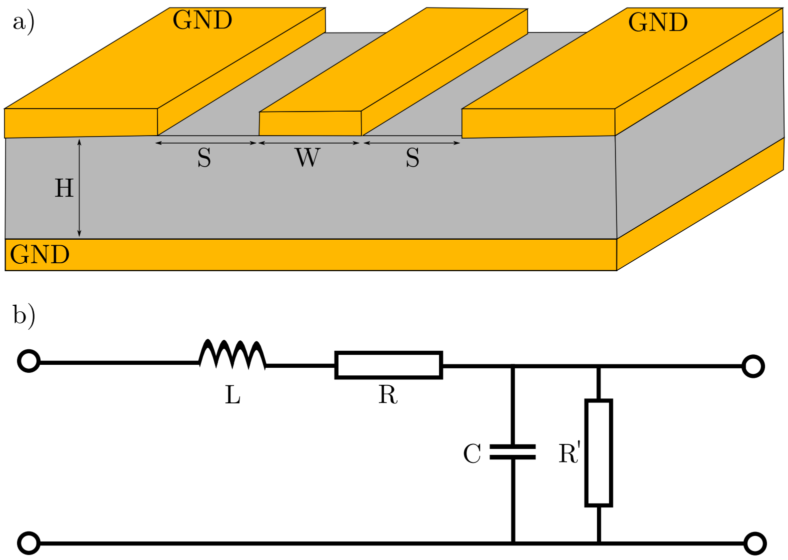

Fig. 8.4 (a) Schematic of CPW geometry with conductors shown in orange, and substrate shown in grey. (b) Equivalent electrical circuit of a single infinitesimal element of a CPW.

with the phase velocity of a propagating wave on a transmission line given by

$$v = \frac{1}{\sqrt{LC}}. \tag{8.17}$$

Two terms contribute to the total inductance of the transmission line: a magnetic term due to the co-propagating conductors, and a kinetic term due to the inertia of the moving Cooper pairs. For a superconductor, due to the presence of the Meissner effect, the contribution of the kinetic inductance term is much larger than is typical in normal-metals.

8.3.1 Quarter Wavelength Resonator

In order to investigate electrical elements such a Josephson junctions, we typically couple them to electrical resonators, such that the resonance provides a probe of the inductance, capacitance and losses. This work employs the use of shorted, transmission lines, of length l, capacitively coupled to a main transmission line known as a feedline. A quarter wavelength ($\lambda/4$) resonator is formed by shorting the far end of a capacitively coupled resonator to ground. According to theory, the input impedance of a shorted transmission line of length l is given by [120]

$$Z_{in} = Z_0 \tanh(\gamma)l, \tag{8.18}$$

where Z_0 is the characteristic impedance of the transmission line. Shorted transmission lines acts as resonators, with a fundamental mode given by

$$f_0 = \frac{1}{2\pi\sqrt{LC}} = \frac{c}{4l\sqrt{\epsilon}}, \tag{8.19}$$

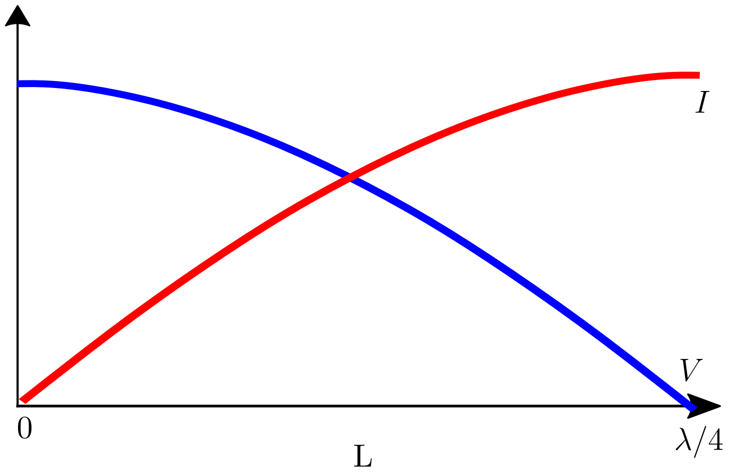

Fig. 8.5 Voltage and current distributions in a $\lambda/4$ resonator showing the fundamental mode resonance.

where ϵ is the dielectric constant, and c is the speed of light in a vacuum. The current and voltage distributions along the length of a shorted $\lambda/4$ resonator are shown in Fig. 8.5. Where the resonator is capacitively coupled to the feedline is the voltage maxima, shown in red at $L = 0$. By shorting the other end to ground, a current maxima is achieved, shown in blue at $L = l$. When the driving voltage is equal to λ, resonance is achieved, and the wavelength of the driving signal is four-times the resonator length, shown by the $\pi/2$ change in phase along the length of the resonator. The presence of a current maxima at the end of the resonator makes this the most sensitive place to couple inductive components, for example Josephson junctions or SQUIDs. Capacitively coupled components are typically coupled close to the feedline to maximise sensitivity. How the losses in a resonator coupled to a feedline can be extracted is discussed in Sec. 9.2.1.

Chapter 9

Experiments on JoFETs Coupled to Microwave Cavities

This chapter will describe our experiments investigating the origin of the previously observed superconducting field-effect. Our aim was to measure the properties of a gated Josephson junction (in the form of a Dayem Bridge) shorting a quarter wavelength resonator to ground. Two main result sets will be introduced. First, low frequency measurements of the full resonance such that the frequency and damping could be extracted. We used the resonance frequency as a direct probe for changes of inductance in the Josephson junction, using the theory introduced in Chapter 8. Second, high frequency measurements at a single frequency allowed us to measure the noise properties of the signal, and use this to characterise the likely origin of the superconducting field-effect.

9.1 Samples

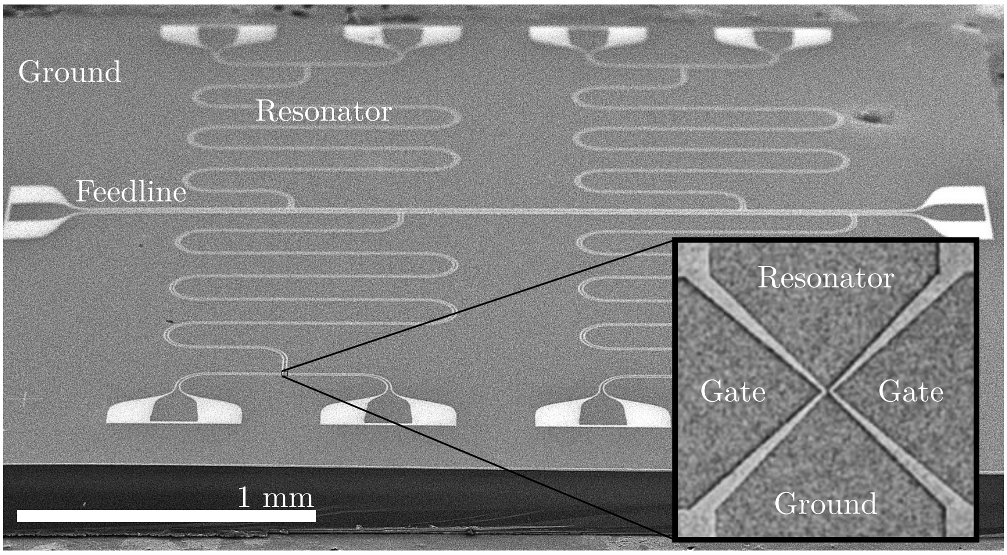

Fig. 9.1 SEM of a chip for measuring JoFETs coupled to superconducting resonators. The complete chip features a single feedline (centre), with four coupled resonators with varying frequency.

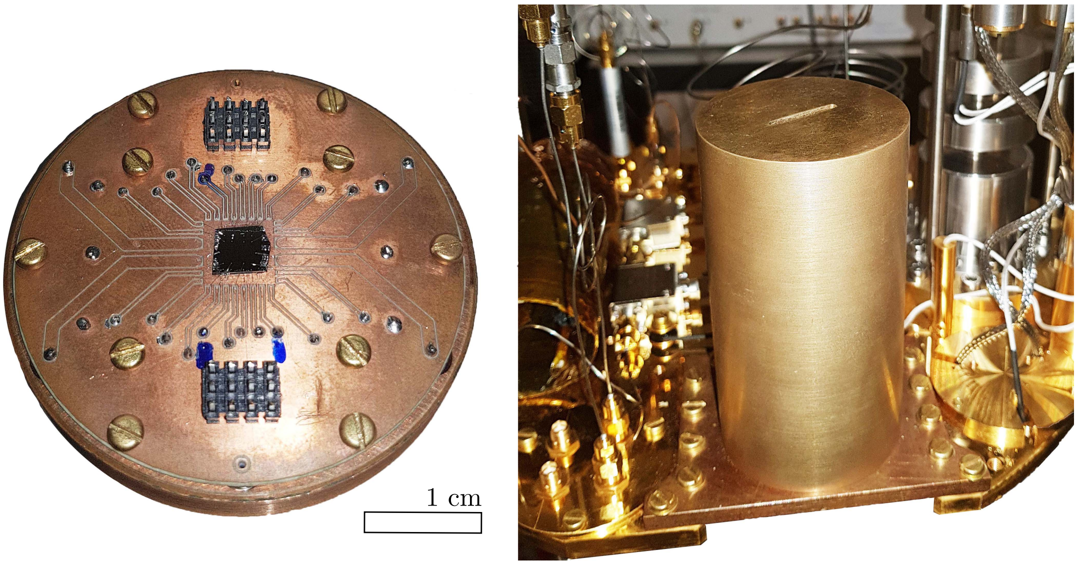

Fig. 9.2 Left: Copper PCB with bonded sample showing 6 high frequency lines, and 24 DC lines allowing four samples to be measured simultaneously. Right: Electrically shielded sample holder into which PCB is mounted. The sample holder is anchored to the mixing chamber of a cryogen-free dilution refrigerator.

The measured devices consisted of a central, microwave feedline with four quarter wavelength resonators capacitively coupled. At the shorted end of each resonator, a Dayem bridge formed a constriction to ground. An SEM of the chip layout is shown in Fig. 9.1. The Dayem bridge was gated on both sides, and an external electric field could be applied to either, with the properties of the junction read-out by the resonator. The samples were fabricated in a cleanroom environment, with details of the fabrication procedure found in App. B3.

Four resonators were coupled to a single feedline on one chip. The length of the quarter-wavelength resonator was continuously varied from 4.5 mm to 5.5 mm for effective frequency-domain multiplexing. The width of the constriction was varied from 40 nm to 120 nm for different coupled resonators. The coupling to the feedline was optimised through simulation and experiment, such that the coupling losses were less than the internal losses, resulting in maximum signal-to-noise ratio without a significant reduction in the total Q. The samples were then wire-bonded and mounted to the PCB, which is then housed inside a shielded sample holder mounted to the mixing chamber, as shown in Fig. 9.2. The sample package contained six high-frequency SMP lines, and 24 DC connectors, allowing all resonators to be measured simultaneously.

9.2 Measurement Scheme

It is proposed that an electric field can significantly modulate the critical current of the Dayem bridge. A modulation of the critical current could cause changes in the Josephson inductance, which would modify the resonance frequency by Eq. (8.19). In addition, overall weakening of the superconductivity could cause an additional damping mechanism.

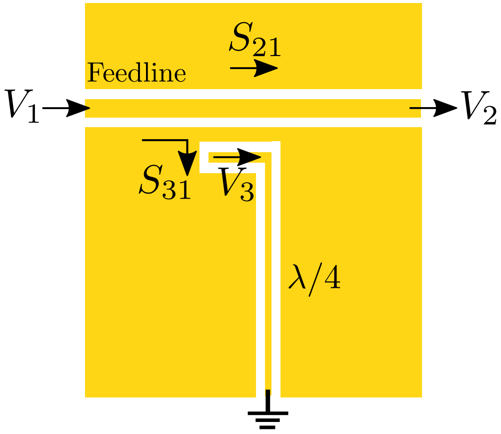

Fig. 9.3 Simplified three-port scattering diagram, showing a feedline capacitively coupled to a quarter-wavelength resonator.

Several different schemes were utilised to characterise this. For measurements of the resonator properties, a VNA was used to supply an RF signal to the transmission line and measure the scattering parameters. By varying the RF frequency a Lorentzian curve could be obtained, and fitted to obtain the frequency, f_0, as well as the internal and coupling losses, Q_i^{-1} and Q_c^{-1}. The details of this approach are described in Sec. 9.2.1. Using a VNA, modulations in the inductance can only be read-out as fast as the frequency can be varied through resonance - typically 1 s for a full frequency sweep. To perform faster readout, continuous downconversion at a single frequency can be performed using an IQ-mixer, allowing readout as fast as $10\,\mathrm{kSa\,s^{-1}}$, limited only by experimental noise. In addition, the current-voltage characteristics of the gated structure were measured using a current-source to determine the gate leakage. All measurements were performed in a cryogen-free dilution cryostat at low temperatures. Further details of the cryogenic setup can be found in App. A3.3.

9.2.1 3 Port Scattering Parameters

Measurements on JoFETs coupled to microwave cavities were performed using a VNA. By utilising a generalised three-port scattering system, as shown in Fig. 9.3, with the 3rd port grounded, we will show how the internal, Q_i, and coupling, Q_c, quality factors can be distinguished. Here we consider a feedline capacitively coupled to a quarter wavelength resonator, shorted to ground at length L. The three ports are defined as the input to the feedline, output of the feedline, and input to the resonator - with the nine component scattering matrix defined as S_{ij},

$$\begin{pmatrix} V_1^- \\ V_2^- \\ V_3^- \end{pmatrix} = \begin{pmatrix} S_{11} & S_{12} & S_{13} \\ S_{21} & S_{22} & S_{23} \\ S_{31} & S_{32} & S_{33} \end{pmatrix} \begin{pmatrix} V_1^+ \\ V_2^+ \\ V_3^+ \end{pmatrix} . \tag{9.1}$$

We assume that the coupling between the resonator and the feedline is small compared with the total transmission ($S_{21} \approx 1$). By symmetry, it is clear that the energy input to the resonator from the feedline must equal the energy leaking back from the resonator to the feedline ($S_{13} = S_{31}$). Importantly, this means a high Q system must have weak coupling between the feedline and the resonator, and therefore a small measured signal amplitude. When characterising the system, as previously discussed, the transmission through the feedline, t_{21}, is measured. Since one must account for energy reflected at load resonator ($\Gamma = -1$ for a $\lambda/4$ resonator), the total transmission is given by

$$t_{21} = S_{21} - \frac{S_{31}^2}{e^{2\gamma l} + S_{33}}, \tag{9.2}$$

where γ is the attenuation coefficient in the line of length, l. From an understanding of the power flow within the resonator, since energy is lost via S_{31} twice per cycle, the losses due to the coupling is given by

$$Q_c^{-1} = \frac{\text{Energy leak from port 3 to port 1 and 2 per cycle}}{\text{Energy stored in the resonator}} = \frac{2|S_{31}|^2}{\pi}. \tag{9.3}$$

The reflectance from the coupling end of the resonator can be expressed as $S_{31} = \sqrt{1 - 2|S_{21}|^2}e^{i\phi}$, where ϕ is the phase acquired at the reflection. The total transmission is hence given by

$$t_{21} = 1 - \frac{Q_c^{-1}}{(Q_c^{-1} + Q_i^{-1}) + 2i(\frac{f-f_r}{f_r})}, \tag{9.4}$$

where f is the measured frequency, and f_r is the resonance frequency. Using this expression, with knowledge of the transmission background, Q_c^{-1} and Q_i^{-1} can be independently extracted by fitting the circle formed by in-phase and out-of-phase components of t_{21}. The circle-fitting procedure utilised here was part of the Qkit software library [124].

9.3 Results

Here we introduce two main sets of experimental results. First, we consider how the full transmission properties vary in spectroscopy measurements using a VNA, for different values of the applied electric field. Due to the time taken to record a complete curve, these measurements are comparatively slow, and demonstrate good agreement with previous observations in the literature. Second, we perform continuous downconversion at a single frequency and demonstrate the non-equilibrium nature of the field-effect phenomena. We will focus on the results for a single gated structure, with resonator length 5.4 mm, constriction size 80 nm and gate separation 100 nm, however other devices demonstrated qualitatively similar results.

9.3.1 Spectroscopy Measurements

Upon applying large gate voltage, changes in the resonance properties were immediately observed. Figure 9.4 shows the fundamental resonance curve of a shorted quarter-wavelength resonator terminated with a gated-Dayem bridge at $T = 10\,\text{mK}$, for four different values of the gate voltage, V_G, applied between a single gate and ground. Below

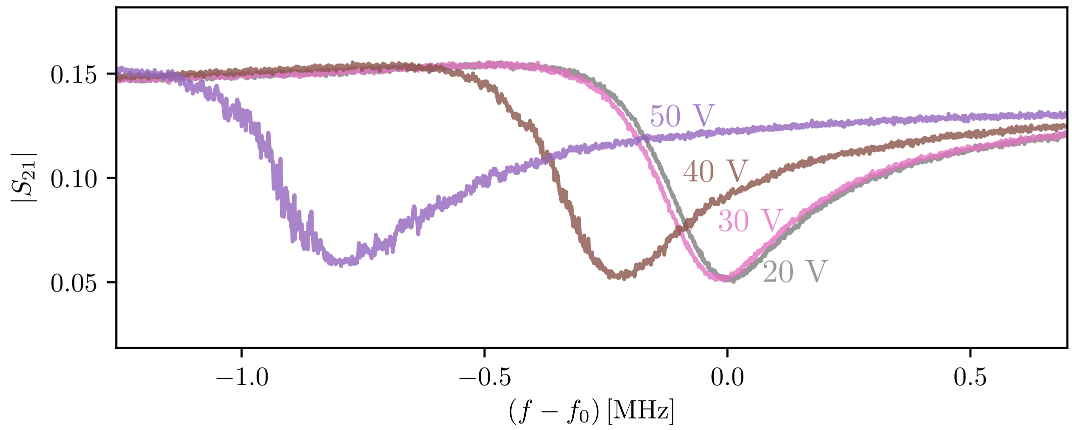

Fig. 9.4 Resonance curves taken for an $f_0 = 3.31\,\mathrm{GHz}$ quarter wavelength resonator, shorted to ground through a gated-Dayem bridge, for four different values of gate-voltage, V_G. Increasing V_G causes a decrease in the resonance frequency, an increase in the resonance width, and a decrease in the signal-to-noise. Results are taken at $T = 10\,\mathrm{mK}$.

$V_\mathrm{G} = 20\,\mathrm{V}$ no change in the resonator properties are observed, however at higher values of V_G a shift to lower frequency, and increased damping is observed. In addition, we note a decrease in the signal-to-noise ratio at higher gate voltages, an effect that will be investigated in more detail in Sec. 9.3.2. All curves shown here were recorded with the same lock-in time constant, and without averaging. It is important to note that the gate voltages used here are extremely large compared to those typically discussed in nanoelectronic experiments.

The ability to tune the resonance frequency using an external gate is useful in applications such as single-photon detection. At $V_\mathrm{G} = 50\,\mathrm{V}$ the frequency shift was $0.8\,\mathrm{MHz}$, or 0.25% of the fundamental, which is quite poor compared to what is currently achievable though the use of external magnetic fields. Tunability could be greatly improved by decreasing the ratio of the kinetic inductance to Josephson inductance, given by Eq. (8.11), since we are only able to tune the latter.

Figure 9.5(a) shows the extracted resonator frequency, f_0, as extracted using the method discussed in Sec. 9.2.1, for $-50 < V_\mathrm{G} < 50\,\mathrm{V}$, and a range of cryostat temperatures. The curves at different temperatures have been manually offset by $0.2\,\mathrm{MHz}$ for clarity. The shift to lower frequency at $V_\mathrm{G} > 30\,\mathrm{V}$ is clear from these measurements, and appears to persist up to temperatures up to $1.7\,\mathrm{K}$. At higher temperatures, the shift in frequency for a given V_G is lower, decreasing to just $0.15\,\mathrm{MHz}$ at $V_\mathrm{G} = 50\,\mathrm{V}$ at $1.7\,\mathrm{K}$.

The results obtained in this way are seemingly consistent with the field-effect presented in the literature, where some modulation of the pairing-mechanism changes the critical current, I_c. It is clear that a decrease in the critical current would increase the inductance (Eq. (8.11)), reducing the resonance frequency (Eq. (8.19)). The field-effect appears to persist up to $T = 1.7\,\mathrm{K}$, however becomes less pronounced. In addition, since the kinetic inductance increases at higher temperatures, we could expect the field-effect to reduce at high temperatures due to the increased kinetic to Josephson inductance ratio.

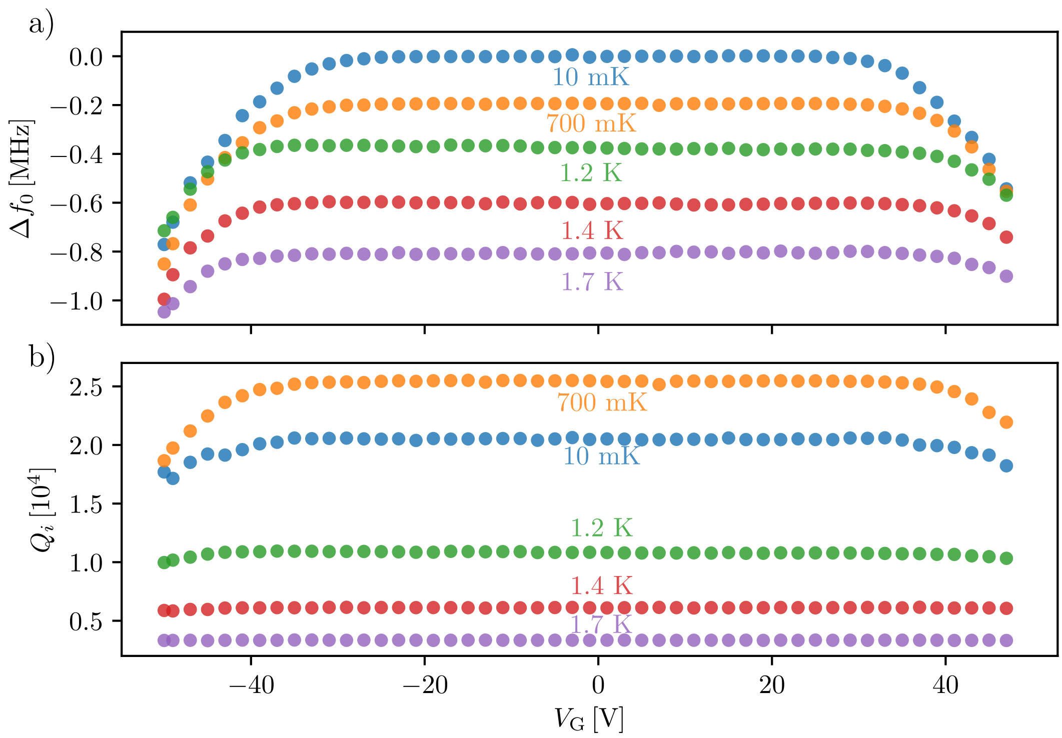

Fig. 9.5 (a) Frequency shift, Δf_0, offset by 0.2 MHz for each temperature, and (b) internal quality factor, Q_i, for an $f_0 = 3.308$ GHz quarter wavelength resonator, shorted to ground through a gated-Dayem bridge, at five different temperatures. As seen previously, increasing V_G leads to a decrease in the resonance frequency, and decrease in the quality factor, above $V_\mathrm{G} = 30$ V. At higher temperature, the quality factor decreases due to thermal effects, meaning the losses due to the field-effect are less pronounced.

The inconsistency between these measurements and the literature arises however, when looking at the damping, Q_i, as a function of V_G as shown in Fig. 9.5(b). Increasing $V_\mathrm{G} > 30$ V causes Q_i to drop, associated with an increase in the losses in the sample, an effect that wasn't presented in the literature, due to the differing methodology used. Previously presented measurements of the critical current dependence on electric field were performed in the DC limit, and therefore could not resolve circuit losses in the same way [113, 114]. It is not immediately clear how a simple modulation of the pairing-mechanism would lead to an additional loss mechanism in the superconductor. It certainly appears that the critical current suppression is associated with an overall weakening of the superconductivity, leading to an additional dissipation channel.

9.3.2 Noise Measurements

Figure 9.4 presented an associated decrease in signal-to-noise ratio with increasing gate-voltage, an unexpected effect to result from a simple change in critical current. An increase in the signal noise points towards a non-equilibrium state on the time-scale of our measurements. To further investigate this phenomena, time-series measurements were performed at a single-frequency for improved time resolution.

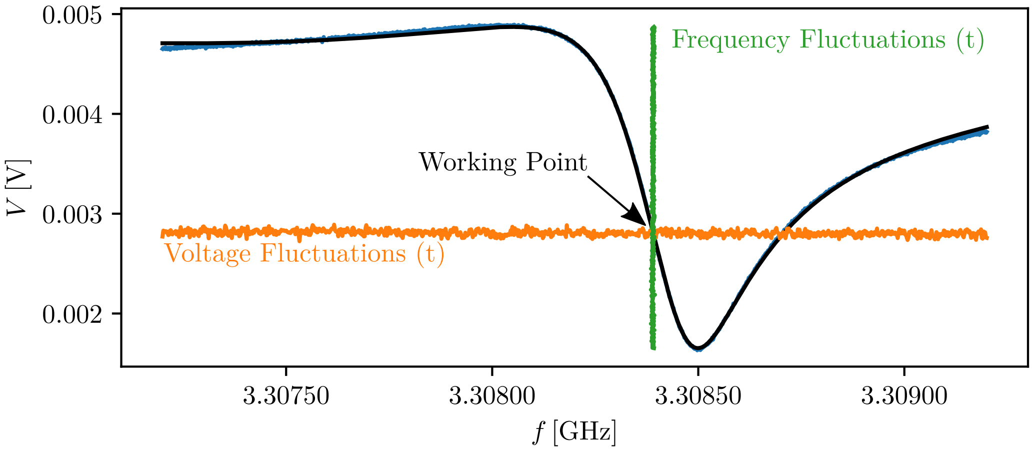

Fig. 9.6 Schematic showing the translation of a fluctuating time-series voltage signal at a single frequency (orange) to a fluctuating time-series frequency signal (green). Measurements were performed at the steepest point on the fitted Lorentzian (black) to maximise the sensitivity to fluctuations.

All voltage noise measurements were converted to frequency noise for more meaningful representations. Figure 9.6 shows schematically the conversion of a voltage-domain signal (orange) to a frequency-domain signal (green) at a working point using the measured Lorentzian (blue) as a transfer function. The frequency was chosen to maximise the sensitivity, by using the steepest point of the Lorentzian curve. Since gate-voltage caused a modulation of the resonance frequency and width, the steepest-point had to be continuously adjusted with the gate-voltage.

Figure 9.7(a) presents the power-spectral-density (PSD) as calculated from the fast-fourier-transform (FFT), of time-series data taken at a range of V_{G} values at 10 mK. The data at $V_{\mathrm{G}} = 0\,\mathrm{V}$ was collected at a single-frequency $f = 3.3084\,\mathrm{MHz}$, with a sample rate of $4096\,\mathrm{Sa\,s^{-1}}$, and a total trace time of 1024 s per voltage. Below $V_{\mathrm{G}} = 20\,\mathrm{V}$ the observable noise increase is very low, with a flat frequency dependence. The increase in signal-noise with V_{G} is shown clearly by the increasing amplitude of the signal spectra. In addition to an increase in the noise amplitude, a clear change in the noise character is observed through the change in gradient. To represent this changing gradient, the spectral density curves were fitted according to the function $\mathrm{PSD} = Af^{-k}$, where A and k were fitting parameters.

Figure 9.7(b) shows the fitted k values as a function of V_{G}, at multiple temperatures, offset by 0.2 for clarity. At low V_{G}, the spectra is flat, corresponding to thermal-noise ($k = 0$) at all temperatures [125]. With increasing V_{G}, the change in k tends towards 1 for low temperatures, with the transition voltage increasing with temperature. Because of this, the magnitude of the change appears to decrease with temperature, with the highest measured temperature $T = 1.7\,\mathrm{K}$ only transitioning to $k = 0.26$. $k = 1$ corresponds to so-called ‘flicker-noise’, typically related with a distribution of two-level fluctuators, each with an associated time constant for relaxation. At high V_{G}, the system therefore

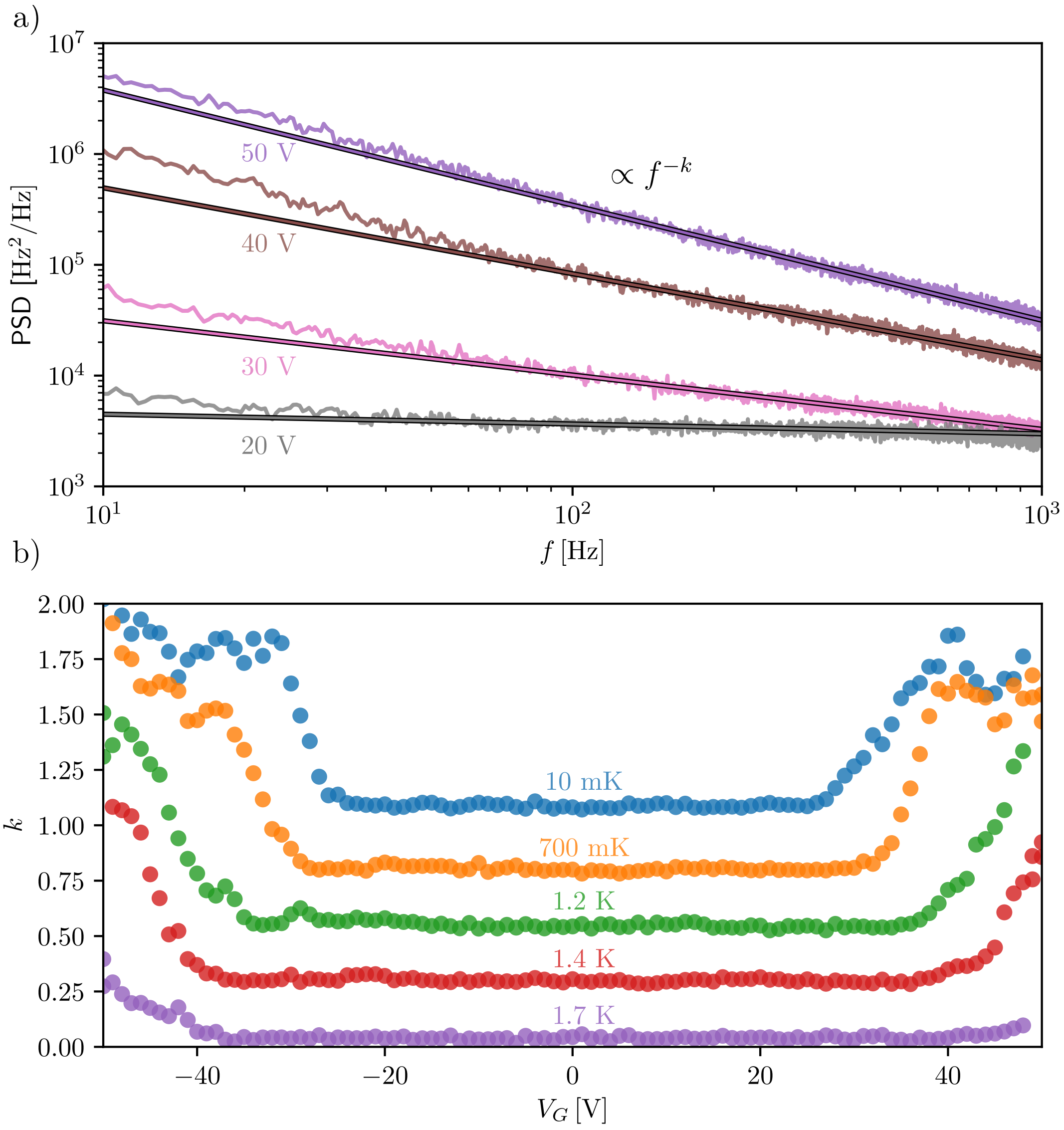

Fig. 9.7 (a) Power spectral density of the resonance signal for a gated-Dayem bridge coupled to a quarter wavelength resonator, for four different values of the gate voltage, V_G. The data is taken with a sampling rate of 4096 Sa s^{-1}, for a total time of 1024 s. The spectra presented here is taken at 10 mK. The spectra are fitted with according to the function PSD $= Af^{-k}$. (b) Fitted k as a function of gate voltage for five different temperatures. The curves are offset by $k = 0.25$ for clarity. For all temperatures, thermal noise dominates at low V_G. At high V_G, low temperatures transition to $k = 1$, whereas for high temperatures the transition is less clear.

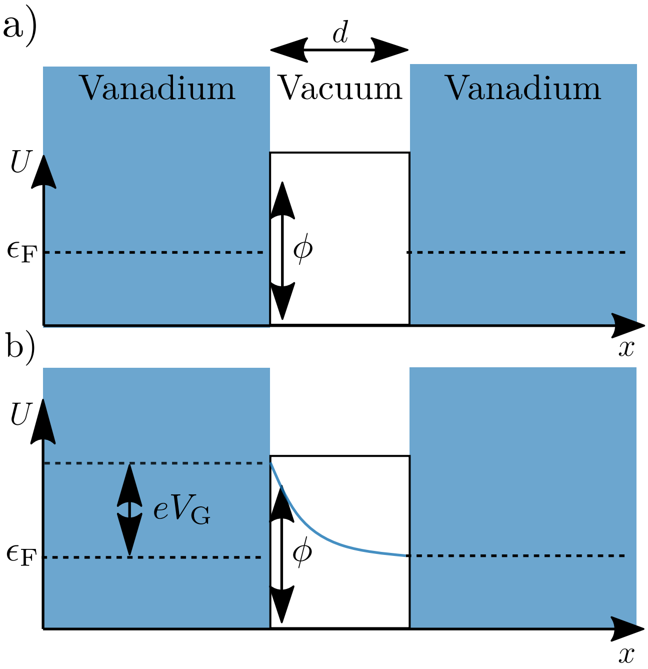

Fig. 9.8 Schematic showing the electrical potential across a dielectric gap of thickness d, in (a) no applied electric field and (b) a strong perpendicular electric field. At large values of the electric-field electrons can quantum-mechanically tunnel across the gap in a process known as field-electron emission. ϕ is the work function of the barrier, and d is the distance across the gap. The Fermi energy is denoted by ϵ_{F}.

appears to be switching between some excited state, and the relaxed state with a random distribution of time constants.

These high-frequency noise measurements point toward a system that is far out of equilibrium, defined a continuous spectra of fluctuations above a minima. In addition, the relaxation rate for the fluctuator spectra increases with increasing temperature, indicating a system that is out of *thermal* equilibrium at high values of V_{G}, but well thermalised at low V_{G}. Weak electron-phonon coupling provides a clear mechanism for this dependence with the coupling between the two ensembles becoming very weak at low temperatures. A locally elevated quasiparticle temperature would be far slower to relax at lower temperatures due to the strong coupling dependence. From these assertions, we postulate that the source of the elevated local temperature is related to parasitic quasiparticle transport from the gate to the constriction or vice-versa. We will show that this hypothesis does not rely on any unknown physical mechanism, and is able to unambiguously explain the origin of the superconducting field effect.

9.4 Field-Electron Emission

Field-electron emission is the spontaneous transmission of electrons in a strong electrostatic field, though a weak dielectric media. Considering a system of two conductors separated by a dielectric, applying an electric field, E, perpendicular to the material-dielectric interface, the tunnelling current flowing between the conductors is given by

$$I = aE^2 \exp\left(\frac{-b\phi^{3/2}}{E}\right), \tag{9.5}$$

where ϕ is the work-function of the conductor, and a and b are geometrical fitting parameters. Equations of this form are known as Fowler-Nordheim type equations [126]. At low values of, E, the dielectric properties of the gap are restored due to a vanishingly small value for I, however at very large values of E, the dielectric properties break down resulting in a leakage current. The values of E at which this 'breakdown' occurs is often referred to as the 'dielectric strength' of the material. For vacuum, the dielectric strength is typically $\sim 10^8\,\mathrm{V\,m^{-1}}$. This process is shown schematically in Fig. 9.8.

Due to the presence of a constant thermal population of electron-like quasiparticles in a superconductor at non-zero temperature, we can expect an analogous tunnelling process to occur in superconducting gates. By modelling the gated construction as a parallel plate capacitor, the electric field is given by $E = V_\mathrm{G}/d$. We therefore expect the differential conductance across the gap to be

$$\frac{dI}{dV_\mathrm{G}} = \frac{a}{d^2}(bd\phi^{3/2} + 2V_\mathrm{G}) \exp\left(\frac{-bd\phi^{3/2}}{V_\mathrm{G}}\right) = A(B + 2V_\mathrm{G}) \exp\left(\frac{-B}{V_\mathrm{G}}\right), \tag{9.6}$$

where $A = a/d^2$ and $B = bd\phi^{3/2}$ are our redefined fitting parameters. To understand the effect of field-dependent leakage currents on the properties of the junction, we can consider the heat-balance equation, assuming all power is dissipated in the constriction

$$\dot{Q} = \Sigma V(T_\mathrm{e}^5 - T_\mathrm{ph}^5), \tag{9.7}$$

where $\Sigma \sim 10^8\,\mathrm{W\,K^{-5}m^{-3}}$ is the electron-phonon coupling constant and V is the constriction volume. T_e and T_ph are the temperatures of the quasiparticle and phonon baths respectively. An electron tunnelling across the gate-constriction boundary can deposit an energy up to eV_G into the material which locally raises the temperature. According to Eq. (8.12) this will cause a significant modulation of the critical current. It is clear from Eq. (9.7) that a higher bath temperature will improve the relaxation rate at which the junction thermalises, reducing the effects of the locally elevated temperature. Therefore, higher temperatures will appear to suppress the field-effect mechanism.

9.4.1 Current-Voltage Measurements

To confirm the idea that the observed field-effect is related to an elevated temperature due to tunnelling electrons from the gate, the leakage current was measured as a function of the gate-voltage, using a DC current source with built-in digital voltmeter in a two-point measurements scheme.

Figure 9.9 shows the differential conductance as a function of gate-voltage at a cryostat temperature $T = 10\,\mathrm{mK}$. Consistent with the previous observations, an increase in the leakage current is observed at $V_\mathrm{G} \sim 30\,\mathrm{V}$, corresponding to a breakdown in the

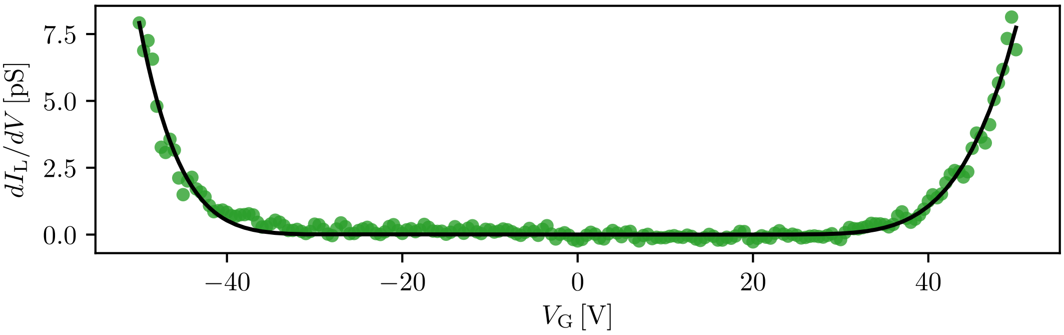

Fig. 9.9 Differential conductance measured from the gate to ground, for a gated-Dayem bridge at 10 mK. A clear increase in the leakage current is seen for $V_G \sim 30\,\mathrm{V}$, indicating electron tunnelling due to the strong electric field.

dielectric properties of the vacuum from the gate to the construction. To model the breakdown, Eq. (9.6) was used with, $A = 388\,\mathrm{pA\,V^{-2}}$, $B = 75.6\,\mathrm{V}$, as shown by the solid-black line providing an excellent fit to the data. The correlation between the theory and the experimental data is strong evidence that field-electron emission is occurring at high values of V_G. The stochastic nature of this process could then give rise to the non-equilibrium nature of the frequency signal.

Using a heat leak $\dot{Q} = 10^{-10}\,\mathrm{W}$, calculated from our leakage current at 50 V, and constriction dimensions $V = 900\,\mathrm{nm} \times 200\,\mathrm{nm} \times 30\,\mathrm{nm}$, the effective temperature can easily be $T \sim 1\,\mathrm{K}$, high enough to significantly modulate the critical current. Using Eq. (8.12), this temperature change would correspond to a decrease in I_c of $\sim 1\%$. Since the total inductance in the system is a sum of the kinetic and Josephson terms, and we do not have an independent measure of the kinetic inductance, it is difficult to exactly exactly predict the frequency shift such a change would correspond to. An independent measurement of an identical resonator, without the coupled Dayem bridge would be extremely useful in characterising the unloaded inductance. A further systematic investigation where the local temperature of the junction could be measured would provide the final piece of evidence that electron-emission is the cause of the field-effect.

9.5 Conclusions and Outlook

In conclusion, a gated Dayem bridge coupled to a superconducting resonator has been measured and characterised for the first time. Our novel scheme has allowed an investigation into the properties of the alleged superconducting field-effect on much shorter time-scales than was previously possible. In the presence of a strong electric-field, spectroscopy measurements of the resonator are consistent with a field-effect modulated critical current, due to a decreasing resonance frequency.

However, a simple reduction in the critical current cannot explain an observed increase in the system damping, without an overall weakening of the superconductivity. Time-series noise data recorded at single frequency clearly point towards a non-equilibrium thermal state modulating the properties of the junction, a conclusion strengthened by repeated measurements at different temperatures. We observe a clear difference in the noise-spectra at low gate voltages versus higher gate voltages. An increased temperature allows the system temperature to relax faster, by improving the electron-phonon coupling. By measuring the leakage current as a function of the applied gate-voltage, we can clearly point to field-electron emission as the source of the non-equilibrium temperature, and hence the source of the field effect. The very large electric fields are enough for quasiparticles to overcome the dielectric, and deposit energy in the superconductor. The leakage current results are in good agreement with a theoretical model for field-electron emission. Our conclusion is in direct contrast with the previously claimed mechanisms presented in the literature, where the authors propose an influence on the pairing mechanism [114].

The non-equilibrium nature of the field-effect rules out several possible applications previously discussed. Since the relaxation relies on the weak electron-phonon coupling, it is not possible to perform modulation of the critical current at GHz frequencies. A JoFET parametric amplifier, or generator is therefore impossible to realise. For the application of single-photon detection, the field effect still presents the possibility to tune the cavity frequency within a few %, without the need to resort to external magnetic fields. However, the significant increase in damping observed at high gate-voltages would severely impact detector performance. Whether a JoFET of this design could be used as a logic element in a superconducting qubit is also questioned by our result. A significantly elevated junction temperature would severely impact coherence times, offsetting any practical benefits from the gate tunability.

To ultimately confirm this, one could locally probe the junction temperature at a high frequency using an SNS, SNIS or SINIS thermometer coupled to an RF circuit. Performing fast temperature readout of a Dayem bridge under changing gate-voltage could unequivocally confirm that the perceived electrostatic field-effect is simply the result of a locally elevated temperature. In addition, a separate measurement of an identical resonator without the Dayem bridge would allow us to properly model the system, since we would know the ratio of the kinetic to Josephson inductance terms.

References

[1] R. William, “Helium, a gaseous constituent of certain minerals,” Proceedings of the Royal Society of London **59**, 325–330 (1895).

[2] H. K. Onnes, “The liquification of helium,” Proceedings of the Royal Academy of Sciences Amsterdam Leiden Communications , 168 (1908).

[3] S. H. Christian Enss, *Low-Temperature Physics* (Springer Berlin Heidelberg, 2005).

[4] W. Keesom and K. Clusius, “Leiden communication 219e,” Proceedings van de Koninklijke Nederlandse Akademie van Wetenschappen **35**, 307 (1932).

[5] J. F. Allen and A. D. Misener, “Flow of liquid helium II,” Nature **141**, 75–75 (1938).

[6] P. Kapitza, “Viscosity of liquid helium below the λ-point,” Nature **141**, 74–74 (1938).

[7] A. M. Guénault, *Basic superfluids* (CRC press, 2003).

[8] J. G. Daunt, K. Mendelssohn, and F. A. Lindemann, “The transfer effect in liquid he ii. i. the transfer phenomena,” Proceedings of the Royal Society of London. Series A. Mathematical and Physical Sciences **170**, 423–439 (1939), https://royalsocietypublishing.org/doi/pdf/10.1098/rspa.1939.0040 .

[9] J. F. Allen and H. Jones, “New phenomena connected with heat flow in helium ii,” Nature **141**, 243–244 (1938).

[10] V. Peshkov, “Second sound in helium II,” Journal of Experimental and Theoretical Physics **11**, 580 (1960).

[11] L. Landau, *Collected Papers of L.D. Landau*, edited by D. T. Haar (Pergamon, 1965) pp. 301 – 330.

[12] L. Tisza, “Transport phenomena in helium II,” Nature **141**, 913–913 (1938).

[13] E. L. Andronikashvili, “A direct observation of two kinds of motion in helium-II,” Journal of Physics. USSR **10**, 201 (1946).

[14] L. Landau, “On the theory of superfluidity,” Physical Review **75**, 884–885 (1949).

[15] A. Schmitt, *Introduction to Superfluidity* (Springer International Publishing, 2014).

[16] P. Hohenberg and P. Martin, “Microscopic theory of superfluid helium,” Annals of Physics **281**, 636 – 705 (2000).

[17] L. Skrbek, *Journal of Physics Conference Series*, Journal of Physics Conference Series, Vol. 318 (IOP Publishing, 2011) p. 012004.

[18] C. F. Barenghi, L. Skrbek, and K. R. Sreenivasan, “Introduction to quantum turbulence,” Proceedings of the National Academy of Sciences **111**, 4647–4652 (2014).

[19] R. P. Feynman, *Chapter II - Application of Quantum Mechanics to Liquid Helium*, edited by C. Gorter, Progress in Low Temperature Physics, Vol. 1 (Elsevier, 1955) pp. 17 – 53.

[20] W. F. Vinen and D. Shoenberg, "The detection of single quanta of circulation in liquid helium II," Proceedings of the Royal Society of London. Series A. Mathematical and Physical Sciences **260**, 218–236 (1961).

[21] W. F. Vinen, "An introduction to quantum turbulence," Journal of Low Temperature Physics **145**, 7–24 (2006).

[22] T. W. B. Kibble, "Topology of cosmic domains and strings," Journal of Physics A: Mathematical and General **9**, 1387–1398 (1976).

[23] M. Tsubota and M. Kobayashi, "Chapter 1 - energy spectra of quantum turbulence," in *Quantum Turbulence*, Progress in Low Temperature Physics, Vol. 16, edited by M. Tsubota and W. Halperin (Elsevier, 2009) pp. 1 – 43.

[24] L. Boué, R. Dasgupta, J. Laurie, V. L'vov, S. Nazarenko, and I. Procaccia, "Exact solution for the energy spectrum of kelvin-wave turbulence in superfluids," Physical Review B **84**, 064516 (2011).

[25] G. Krstulovic, "Kelvin-wave cascade and dissipation in low-temperature superfluid vortices," Physical Review E **86**, 055301 (2012).

[26] R. Blaauwgeers, M. Blažková, M. Človečko, V. B. Eltsov, R. de Graaf, J. Hosio, M. Krusius, D. Schmoranzer, W. Schoepe, L. Skrbek, P. Skyba, R. E. Solntsev, and D. E. Zmeev, "Quartz Tuning Fork: Thermometer, Pressure- and Viscometer for Helium Liquids," Journal of Low Temperature Physics **146**, 537–562 (2007).

[27] G. R. Pickett, M. P. Enrico, S. N. Fisher, A. M. Guénault, and K. Torizuka, "Superfluid ^{3}He at very low temperatures: a very unusual excitation gas," Physica B: Condensed Matter **197**, 390 (1994).

[28] M. Blažková, D. Schmoranzer, and L. Skrbek, "Transition from laminar to turbulent drag in flow due to a vibrating quartz fork," Physical Review E **75**, 025302 (2007).

[29] G. Sheshin, A. Zadorozhko, É. Ya. Rudavskii, V. K. Chagovets, L. Skrbek, and M. Blažková, "Characteristics of the transition to turbulence in superfluid ^{4}He at low temperatures," Low Temperature Physics **34**, 875–883 (2008).

[30] D. I. Bradley, M. J. Fear, S. Fisher, A. M. Guénault, R. P. Haley, C. Lawson, P. McClintock, G. R. Pickett, R. Schanen, V. Tsepelin, and L. Smethurst, "Transition to turbulence for a quartz tuning fork in superfluid ^{4}He," Journal of Low Temperature Physics **156**, 116–131 (2009).

[31] M. Blažková, D. Schmoranzer, L. Skrbek, and W. F. Vinen, "Generation of turbulence by vibrating forks and other structures in superfluid ^{4}He," Physical Review B **79**, 054522 (2009).

[32] Y. Nago, T. Ogawa, K. Obara, H. Yano, O. Ishikawa, and T. Hata, "Time-of-flight experiments of vortex rings propagating from turbulent region of superfluid ^{4}He at high temperature," Journal of Low Temperature Physics **162**, 322–328 (2011).

[33] D. I. Bradley, M. Človečko, S. N. Fisher, D. Garg, E. Guise, R. P. Haley, O. Kolosov, G. R. Pickett, V. Tsepelin, D. Schmoranzer, and L. Skrbek, "Crossover from hydrodynamic to acoustic drag on quartz tuning forks in normal and superfluid ^{4}He," Physical Review B **85**, 014501 (2012).

[34] A. Salmela, J. Tuoriniemi, and J. Rysti, "Acoustic resonances in helium fluids excited by quartz tuning forks," Journal of Low Temperature Physics **162**, 678–685 (2011).

[35] D. Schmoranzer, M. La Mantia, G. Sheshin, I. Gritsenko, A. Zadorozhko, M. Rotter, and L. Skrbek, “Acoustic emission by quartz tuning forks and other oscillating structures in cryogenic ^{4}He fluids,” Journal of Low Temperature Physics **163**, 317–344 (2011).

[36] M. Blažková, T. V. Chagovets, M. Rotter, D. Schmoranzer, and L. Skrbek, “Cavitation in liquid helium observed in a flow due to a vibrating quartz fork,” Journal of Low Temperature Physics **150**, 194–199 (2008).

[37] M. Blažková, D. Schmoranzer, and L. Skrbek, “On cavitation in liquid helium in a flow due to a vibrating quartz fork,” Low Temperature Physics **34**, 298–307 (2008).

[38] D. I. Bradley, M. Človečko, E. Gažo, and P. Skyba, “Probing andreev reflection in superfluid ^{3}He-B using a quartz tuning fork,” Journal of Low Temperature Physics **152**, 147–155 (2008).

[39] D. I. Bradley, P. Crookston, S. N. Fisher, A. Ganshin, A. M. Guénault, R. P. Haley, M. J. Jackson, G. R. Pickett, R. Schanen, and V. Tsepelin, “The damping of a quartz tuning fork in superfluid ^{3}He-B at low temperatures,” Journal of Low Temperature Physics **157**, 476 (2009).

[40] M. Človečko, E. Gažo, M. Kupka, M. Skyba, and P. Skyba, “High quality tuning forks in superfluid ^{3}He-B below 200 μK,” Journal of Low Temperature Physics **162**, 669–677 (2011).

[41] M. J. Jackson, O. Kolosov, D. Schmoranzer, L. Skrbek, V. Tsepelin, and A. J. Woods, “Measurements of vortex line density generated by a quartz tuning fork in superfluid ^{4}He,” Journal of Low Temperature Physics **183**, 208–214 (2016).

[42] M. Človečko, E. Gažo, M. Skyba, and P. Skyba, “NMR-like effect on the anisotropic magnetic moment of surface bound states in the topological superfluid ^{3}He-B,” Physical Review B **99**, 104518 (2019).

[43] D. I. Bradley, S. N. Fisher, A. M. Guénault, R. P. Haley, J. Kopu, H. Martin, G. R. Pickett, J. E. Roberts, and V. Tsepelin, “Relic topological defects from brane annihilation simulated in superfluid ^{3}He,” Nature **4**, 46 (2008).

[44] D. I. Bradley, S. N. Fisher, A. M. Guénault, R. P. Haley, G. R. Pickett, D. Potts, and V. Tsepelin, “Direct measurement of the energy dissipated by quantum turbulence,” Nature Physics **7**, 473–476 (2011).

[45] D. I. Bradley, A. M. Guénault, R. P. Haley, G. R. Pickett, and V. Tsepelin, “Andreev reflection in superfluid ^{3}He-B: A probe for quantum turbulence,” Annual Review of Condensed Matter Physics **8**, 407–430 (2017).

[46] S. Ahlstrom, *Quasiparticle beam profile measurements in superfluid* $^3\mathrm{He}-\mathrm{B}$, Ph.D. thesis, Lancaster University (2016).

[47] B. Jakoby, M. Scherer, M. Buskies, and H. Eisenschmid, “An automotive engine oil viscosity sensor,” IEEE Sensors Journal **3**, 562–568 (2003).

[48] M. González, G. Ham, A. A. Haddad, G. Bernero, and M. Deffenbaugh, “Downhole viscosity measurement platform using tuning fork oscillators,” in *2015 IEEE SENSORS* (2015) pp. 1–4.

[49] A. M. Guénault and G. R. Pickett, “Liquid ^{3}He at ultralow temperatures: The long mean free path limit,” Physica B+C **126**, 260 – 266 (1984).

[50] D. I. Bradley, S. N. Fisher, A. M. Guénault, R. P. Haley, C. R. Lawson, G. R. Pickett, R. Schanen, M. Skyba, V. Tsepelin, and D. E. Zmeev, “Breaking the superfluid speed limit in a fermionic condensate,” Nature Physics **12**, 1017 (2016).

[51] D. Bradley, S. Fisher, A. M. Guénault, R. Haley, M. Holmes, S. O'Sullivan, G. Pickett, and V. Tsepelin, "Grid turbulence in superfluid ^{3}He-B at low temperatures." Journal of Low Temperature Physics **150**, 364–372 (2008).

[52] J. Luzuriaga, "Measurements in the laminar and turbulent regime of superfluid ^{4}He by means of an oscillating sphere," Journal of Low Temperature Physics **108**, 267–277 (1997).

[53] M. Defoort, S. Dufresnes, S. Ahlstrom, D. I. Bradley, R. P. Haley, A. M. Guénault, E. A. Guise, G. R. Pickett, M. Poole, A. J. Woods, V. Tsepelin, S. N. Fisher, H. Godfrin, and E. Collin, "Probing Bogoliubov quasiparticles in superfluid ^{3}He with a 'vibrating-wire like' MEMS device," Journal of Low Temperature Physics **183**, 284–291 (2016).

[54] C. Barquist, W. Jiang, P. Zheng, Y. Lee, and H. B. Chan, "The effect of remnant vortices in He-II on multiple modes of a micro-electromechanical resonator," Journal of Low Temperature Physics **196** (2019).

[55] M. González, P. Bhupathi, B. H. Moon, P. Zheng, G. Ling, E. Garcell, H. B. Chan, and Y. Lee, "Characterization of MEMS devices for the study of superfluid helium films," Journal of Low Temperature Physics **162**, 661–668 (2011).

[56] P. Günther, U. Fischer, and K. Dransfeld, "Scanning nearfield acoustic microscopy," Applied Physics B **48**, 89–92 (1989).

[57] K. Karrat and R. D. Grober, "Tip-sample distance control for near-field scanning optical microscopes," in *Near-Field Optics*, Vol. 2535, edited by M. A. Paesler and P. J. Moyer, International Society for Optics and Photonics (SPIE, 1995) pp. 69 – 81.

[58] K. Karrai and R. D. Grober, "Piezoelectric tip-sample distance control for near field optical microscopes," Applied Physics Letters **66**, 1842–1844 (1995).

[59] K. L. Ekinci and M. L. Roukes, "Nanoelectromechanical systems," Review of Scientific Instruments **76**, 061101 (2005).

[60] M. Defoort, K. J. Lulla, T. Crozes, O. Maillet, O. Bourgeois, and E. Collin, "Slippage and boundary layer probed in an almost ideal gas by a nanomechanical oscillator," Physical Review Letters **113**, 136101 (2014).

[61] M. González, P. Zheng, E. Garcell, Y. Lee, and H. B. Chan, "Comb-drive micro-electro-mechanical systems oscillators for low temperature experiments," Review of Scientific Instruments **84**, 025003 (2013).

[62] G. I. Harris, D. L. McAuslan, E. Sheridan, Y. Sachkou, C. Baker, and W. P. Bowen, "Laser cooling and control of excitations in superfluid helium," Nature Physics **12**, 788 (2016).

[63] N. R. Wilson and J. V. Macpherson, "Carbon nanotube tips for atomic force microscopy," Nature Nanotechnology **4**, 483 (2009).

[64] V. Kara, Y.-I. Sohn, H. Atikian, V. Yakhot, M. Lončar, and K. L. Ekinci, "Nanofluidics of single-crystal diamond nanomechanical resonators," Nano Letters **15**, 8070–8076 (2015).

[65] T. P. Burg, M. Godin, S. M. Knudsen, W. Shen, G. Carlson, J. S. Foster, K. Babcock, and S. R. Manalis, "Weighing of biomolecules, single cells and single nanoparticles in fluid," Nature **446**, 1066 (2007).

[66] J. Melcher, J. Stirling, F. G. Cervantes, J. R. Pratt, and G. A. Shaw, "A self-calibrating optomechanical force sensor with femtonewton resolution," Applied Physics Letters **105**, 233109 (2014).

[67] J. Chaste, A. Eichler, J. Moser, G. Ceballos, R. Rurali, and A. Bachtold, "A nanomechanical mass sensor with yoctogram resolution," Nature Nanotechnology **7**, 301 (2012).

[68] A. Kraus, A. Erbe, and R. H. Blick, "Nanomechanical vibrating wire resonator for phonon spectroscopy in liquid helium," Nanotechnology **11**, 165–168 (2000).

[69] K. Y. Fong, D. Jin, M. Poot, A. Bruch, and H. X. Tang, "Phonon coupling between a nanomechanical resonator and a quantum fluid," Nano Letters **19**, 3716–3722 (2019).

[70] T. Kamppinen and V. B. Eltsov, "Nanomechanical resonators for cryogenic research," Journal of Low Temperature Physics (2018).

[71] D. I. Bradley, R. George, A. M. Guénault, R. P. Haley, S. Kafanov, M. T. Noble, Yu. A. Pashkin, G. R. Pickett, M. Poole, J. R. Prance, M. Sarsby, R. Schanen, V. Tsepelin, T. Wilcox, and D. E. Zmeev, "Operating nanobeams in a quantum fluid," Scientific Reports **7**, 4876 (2017).

[72] A. M. Guénault, A. Guthrie, R. P. Haley, S. Kafanov, Yu. A. Pashkin, G. R. Pickett, M. Poole, R. Schanen, V. Tsepelin, D. E. Zmeev, E. Collin, O. Maillet, and R. Gazizulin, "Probing superfluid ^{4}He with high-frequency nanomechanical resonators down to millikelvin temperatures," Physical Review B **100**, 020506 (2019).

[73] D. I. Bradley, R. E. George, D. Gunnarsson, R. P. Haley, H. Heikkinen, Yu. A. Pashkin, J. Penttilä, J. R. Prance, M. Prunnila, L. Roschier, and M. Sarsby, "Nanoelectronic primary thermometry below 4 mK," Nature Communications **7**, 10455 (2016).

[74] A. D. O'Connell, M. Hofheinz, M. Ansmann, R. C. Bialczak, M. Lenander, E. Lucero, M. Neeley, D. Sank, H. Wang, M. Weides, J. Wenner, J. M. Martinis, and A. N. Cleland, "Quantum ground state and single-phonon control of a mechanical resonator," Nature **464**, 697 (2010).

[75] M. Poot and H. S. van der Zant, "Mechanical systems in the quantum regime," Physics Reports **511**, 273 – 335 (2012).

[76] H. W. C. Postma, I. Kozinsky, A. Husain, and M. L. Roukes, "Dynamic range of nanotube- and nanowire-based electromechanical systems," Applied Physics Letters **86**, 223105 (2005).

[77] I. Kovacic and M. J. Brennan, *The Duffing equation: nonlinear oscillators and their behaviour* (John Wiley & Sons, 2011).

[78] A. N. Cleland and M. L. Roukes, "Fabrication of high frequency nanometer scale mechanical resonators from bulk Si crystals," Applied Physics Letters **69**, 2653–2655 (1996).

[79] A. Bokaian, "Natural frequencies of beams under tensile axial loads," Journal of Sound and Vibration **142**, 481 – 498 (1990).

[80] S. J. Blundell, *Concepts in Thermal Physics* (Oxford University Press, 2009).

[81] K. Karrai, "Lecture notes on shear and friction force detection with quartz tuning forks," Proceedings of the Work presented at the "Ecole Thématique du CNRS" on near-field optics, La Londe les Maures, France , 1–23 (2000).

[82] I. Wilson-Rae, "Intrinsic dissipation in nanomechanical resonators due to phonon tunneling," Physical Review B **77**, 245418 (2008).

[83] R. Lifshitz and M. L. Roukes, "Thermoelastic damping in micro- and nanomechanical systems," Physical Review B **61**, 5600–5609 (2000).

[84] M. Morishita, T. Kuroda, A. Sawada, and T. Satoh, "Mean free path effects in superfluid ^{4}He," Journal of Low Temperature Physics **76**, 387–415 (1989).

[85] L. Landau and E. Lifshitz, "Chapter VIII - sound," in *Fluid Mechanics* (Pergamon, 1987) 2nd ed., pp. 251 – 312.

[86] L. Bruschi and M. Santini, "Vibrating wire viscometer," Review of Scientific Instruments **46**, 1560–1568 (1975), https://doi.org/10.1063/1.1134103 .

[87] S. Balibar, "Nucleation in quantum liquids," Journal of Low Temperature Physics **129**, 363–421 (2002).

[88] L. D. Landau and E. M. Lifshitz, *Statistical Mechanics* (Elsevier, 2013).

[89] S. L. Ahlstrom, D. I. Bradley, M. Človečko, S. N. Fisher, A. M. Guénault, E. A. Guise, R. P. Haley, O. Kolosov, P. V. E. McClintock, G. R. Pickett, M. Poole, V. Tsepelin, and A. J. Woods, "Frequency-dependent drag from quantum turbulence produced by quartz tuning forks in superfluid ^{4}He," Physical Review B **89**, 014515 (2014).

[90] R. Hänninen, M. Tsubota, and W. F. Vinen, "Generation of turbulence by oscillating structures in superfluid helium at very low temperatures," Physical Review B **75**, 064502 (2007).

[91] M. Niemetz, R. Hänninen, and W. Schoepe, "On the transition from potential flow to turbulence around a microsphere oscillating in superfluid ^{4}He," Journal of Low Temperature Physics **187**, 195–220 (2017).

[92] R. Hänninen and W. Schoepe, "Universal onset of quantum turbulence in oscillating flows and crossover to steady flows," Journal of Low Temperature Physics **158**, 410 (2009).

[93] L. P. Pitaevskii, L. D. Landau, and E. M. Lifshitz, *Statistical Physics: Course of Theoretical Physics - Vol. 9* (Elsevier India, 2014).

[94] L. Galantucci, A. W. Baggaley, N. G. Parker, and C. F. Barenghi, "Crossover from interaction to driven regimes in quantum vortex reconnections," Proceedings of the National Academy of Sciences **116**, 12204–12211 (2019).

[95] H. E. Hall, "The inertia of heat flow in liquid helium II," Proceedings of the Physical Society. Section A **67**, 485–494 (1954).

[96] A. N. Cleland and M. L. Roukes, "Noise processes in nanomechanical resonators," Journal of Applied Physics **92**, 2758–2769 (2002).

[97] *CRC Handbook of Chemistry and Physics, 92nd Edition* (CRC Press, 2011).

[98] K. J. Lulla, M. Defoort, C. Blanc, O. Bourgeois, and E. Collin, "Evidence for the role of normal-state electrons in nanoelectromechanical damping mechanisms at very low temperatures," Physical Review Letters **110**, 177206 (2013).

[99] A. D. B. Woods and R. A. Cowley, "Structure and excitations of liquid helium," Reports on Progress in Physics **36**, 1135–1231 (1973).

[100] E. T. Swartz and R. O. Pohl, "Thermal boundary resistance," Reviews of Modern Physics **61**, 605–668 (1989).

[101] H. W. M. Salemink, H. van Kempen, and P. Wyder, "Ballistic-phonon pulses in a solid-liquid He-II interface," Journal of Physics C: Solid State Physics **13**, 5089–5103 (1980).

[102] D. Kivotides, J. C. Vassilicos, D. C. Samuels, and C. F. Barenghi, "Kelvin waves cascade in superfluid turbulence," Physical Review Letters **86**, 3080–3083 (2001).

[103] W. F. Vinen, M. Tsubota, and A. Mitani, "Kelvin-wave cascade on a vortex in superfluid ^{4}He at a very low temperature," Physical Review Letters **91**, 135301 (2003).

[104] D. I. Bradley, R. P. Haley, S. Kafanov, M. T. Noble, G. R. Pickett, V. Tsepelin, J. Vonka, and T. Wilcox, "Probing liquid ^{4}He with quartz tuning forks using a novel multifrequency lock-in technique," Journal of Low Temperature Physics **184**, 1080–1091 (2016).

[105] D. Schmoranzer, M. J. Jackson, V. Tsepelin, M. Poole, A. J. Woods, M. Človečko, and L. Skrbek, "Multiple critical velocities in oscillatory flow of superfluid ^{4}He due to quartz tuning forks," Physical Review B **94**, 214503 (2016).

[106] R. J. Donnelly and C. F. Barenghi, "The observed properties of liquid helium at the saturated vapor pressure," Journal of Physical and Chemical Reference Data **27**, 1217–1274 (1998).

[107] V. B. Efimov, D. Garg, O. Kolosov, and P. V. E. McClintock, "Direct measurement of the critical velocity above which a tuning fork generates turbulence in superfluid helium," Journal of Low Temperature Physics **158**, 456 (2009).

[108] D. O. Clubb, O. V. L. Buu, R. M. Bowley, R. Nyman, and J. R. Owers-Bradley, "Quartz tuning fork viscometers for helium liquids," Journal of Low Temperature Physics **136**, 1–13 (2004).

[109] J. Bardeen, L. N. Cooper, and J. R. Schrieffer, "Theory of superconductivity," Physical Review **108**, 1175–1204 (1957).

[110] M. Tinkham, *Introduction to superconductivity* (Courier Corporation, 2004).

[111] G. De Simoni, F. Paolucci, P. Solinas, E. Strambini, and F. Giazotto, "Metallic supercurrent field-effect transistor," Nature Nanotechnology **13**, 802–805 (2018).

[112] F. Paolucci, G. De Simoni, E. Strambini, P. Solinas, and F. Giazotto, "Ultra-efficient superconducting Dayem bridge field-effect transistor," Nano Letters **18**, 4195–4199 (2018).

[113] G. De Simoni, F. Paolucci, C. Puglia, and F. Giazotto, "Josephson field-effect transistors based on all-metallic Al/Cu/Al proximity nanojunctions," ACS Nano **13**, 7871–7876 (2019).

[114] F. Paolucci, F. Vischi, G. De Simoni, C. Guarcello, P. Solinas, and F. Giazotto, "Field-effect controllable metallic Josephson interferometer," Nano Letters **19**, 6263–6269 (2019).

[115] H. K. Onnes, "The resistance of pure mercury at helium temperatures," Communication Physics Laboratory Univiversity, Leiden, 122-124 (1911).

[116] W. Meissner and R. Ochsenfeld, "Ein neuer effekt bei eintritt der supraleitfähigkeit," Naturwissenschaften **21**, 787–788 (1933).

[117] V. L. Ginzburg and L. D. Landau, "On the theory of superconductivity," Journal Experimental and Theoretical.Physics USSR **20**, 1064–1082 (1950).

[118] P. Drude, "Zur elektronentheorie der metalle; II. teil. galvanomagnetische und thermomagnetische effecte," Annalen der Physik **308**, 369–402 (1900).

[119] R. G. Chambers and O. R. Frisch, "The anomalous skin effect," Proceedings of the Royal Society of London. Series A. Mathematical and Physical Sciences **215**, 481–497 (1952).

[120] J. Gao, *The physics of superconducting microwave resonators*, Ph.D. thesis, California Institute of Technology (2008).

[121] F. London, H. London, and F. A. Lindemann, "The electromagnetic equations of the supraconductor," Proceedings of the Royal Society of London. Series A - Mathematical and Physical Sciences **149**, 71–88 (1935).

[122] A. B. Pippard and W. L. Bragg, "An experimental and theoretical study of the relation between magnetic field and current in a superconductor," Proceedings of the Royal Society of London. Series A. Mathematical and Physical Sciences **216**, 547–568 (1953).

[123] B. Josephson, "Possible new effects in superconductive tunnelling," Physics Letters **1**, 251 – 253 (1962).

[124] J. Braumueller, J. Brehm, M. Pfirrmann, S. Probst, A. Schneider, Y. Schön, A. Stehli, and H. R. M. Wildermuth, "qkitgroup/qkit," GitHub (2019).

[125] B. Boashash, *Time-frequency signal analysis and processing: a comprehensive reference* (Academic Press, 2015).

[126] R. H. Fowler and L. Nordheim, "Electron emission in intense electric fields," Proceedings of the Royal Society of London. Series A, Containing Papers of a Mathematical and Physical Character **119**, 173–181 (1928).

[127] S. Holt and P. Skyba, "Electrometric direct current I/V converter with wide bandwidth," Review of Scientific Instruments **83**, 064703 (2012).

Experimental Details

A1 Scattering Parameters

A2 Experimental Cells

Two experimental cells were utilised for measurements in liquid helium. These were required to be leak-tight, whilst having RF feedthroughs for electrical signals. The first design used a conical cap, with vacuum grease creating the seal, whereas the second design used an indium seal. An indium seal is created by crushing a thin strip of indium wire between the two metal surfaces to fill any imperfections. This technique is used commonly to form seals at low temperature interfaces. Indium vacuum seal proved to be more reliable than seals formed with vacuum grease, with several experimental leaks attributed to a poor seal using vacuum grease. However, to allows space for the indium seal the cell had to be larger, and therefore heavier. Photographs of the two cell designs are shown in Fig. A.1.

A3 Cryostats

A3.1 1 K Cryostat:I

Cryostat:I consisted of a custom insert built for an Oxford instruments dewar, capable of reaching $\sim 1.2\,\mathrm{K}$. Working from the inside out, this system featured an experimental cell as shown in Fig. A.1(top), which housed the samples. This was thermally coupled to a 1 K pot, surrounded by a vacuum space called the IVC. Surrounding this was a large 4.2 K helium bath. A needle valve allowed the 1 K pot to be filled from the helium bath without thermal contact when not filling. Outside the helium bath is another vacuum space, followed by a nitrogen jacket at 77 K. A final vacuum space separates the nitrogen

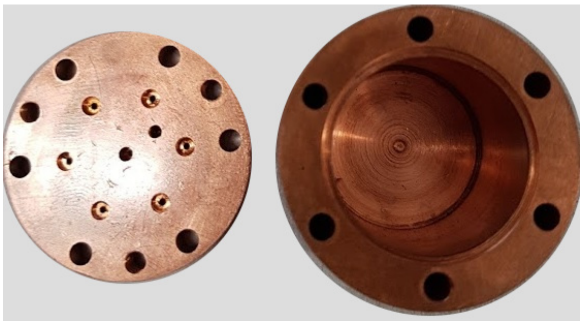

Fig. A.1 Photograph of two cell designs used in nanobeam measurements. Top: First design with four SMP feedthroughs and sealed using vacuum grease. Bottom: Second design with six SMP feedthroughs, closed with an indium seal.

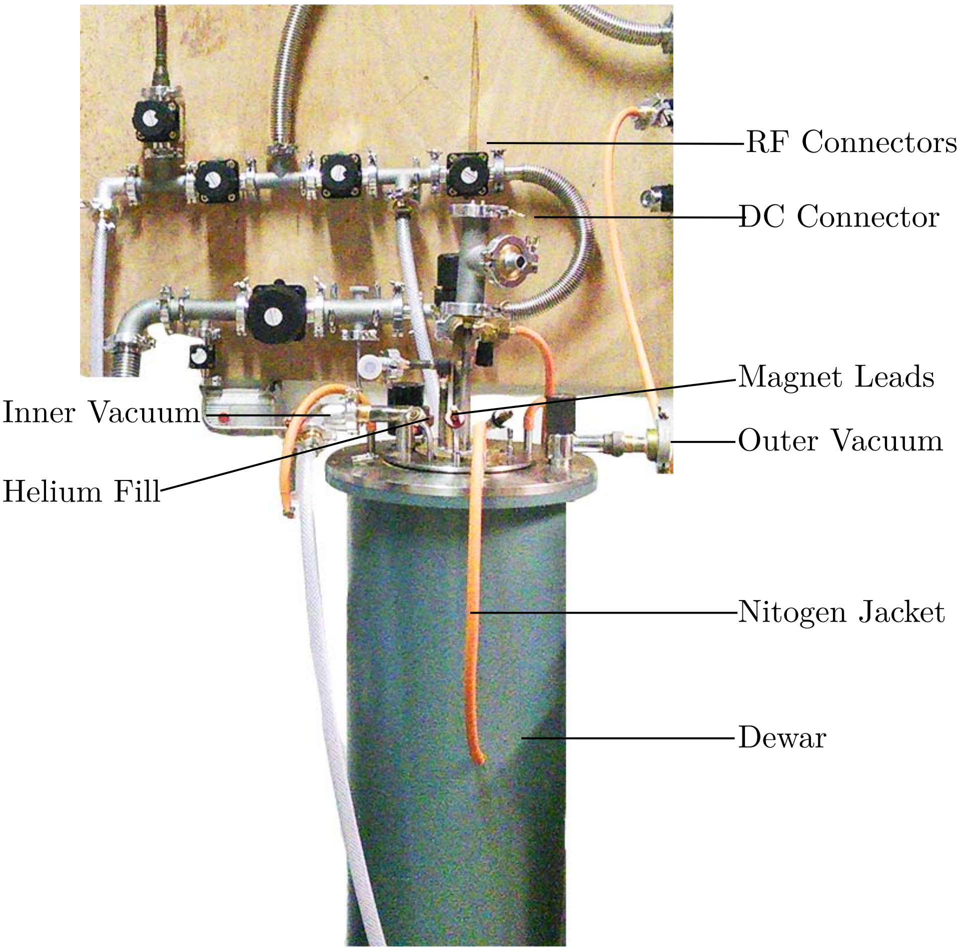
RF Connectors
DC Connector
Magnet Leads
Inner Vacuum
Outer Vacuum
Helium Fill
Nitogen Jacket
Dewar

Fig. A.2 Photograph of 1 K cryostat setup, and associated gas handling system, used for measuring nanomechanical beams in the temperature range 4.2 K to 1.2 K.

jacket from room temperature. The temperature of the helium in the cell was controlled by pumping on the 1 K pot, since these are in thermal contact. In this way, hot atoms are removed and the overall bath temperature decreases. The process by which this occurs is known as evaporative cooling, and the temperature is then inferred from measurements of the saturated vapour pressure [106]. This technique is typically effective to ∼1 K for ^{4}He, since the saturated vapour pressure is vanishingly small at these temperatures [106].

The use of a separate experimental cell inside the 1 K pot allowed vacuum measurements to be performed, and reduced the amount of dust and oil, since the cell could be removed and cleaned. The cell was typically filled directly from a ^{4}He dewar boil-off, using a separate capillary fill-line.

A wall-mounted gas handling system allowed the pumping and recovery of the helium, as well as evacuation of the vacuum spaces using a rotary pump. Electrically, transmission measurements were performed using a VNA, through SMA feed-throughs on the top of the fridge, connected to SMP connectors on the experimental cell. A 24-pin Fisher connector allowed the measurement of 8 level sensing resistors, 4 thermometry resistors, and a vibrating wire resonator. The thermometry resistors were read out using a resistance bridge which could be monitored remotely. A 5 T superconducting solenoid was mounted in the helium bath, to control the applied magnetic field. Also in the 1 K pot was a heater, such that the cryostat temperature could be varied independently. The base temperature of this system was ∼ 1.5 K, with a hold-time of ∼ 8 hours on its best run. Photographs and schematics of this setup are shown in Fig. A.2, Fig. A.3.

The electrical schematic is shown in Fig. A.4. The AC signal was typically passed through 80 dB of room temperature attenuation. Two Femto HSA-X-2-40 room temperature amplifiers were used to recover the signal. This setup did not utilise any cold attenuation or amplification which could have improved our signal-noise ratio.

A3.2 1 K Cryostat:II

Cryostat:II comprised of a custom-built glass cryostat for superfluid ^{4}He measurements from 4.2 K to 1.2 K. A central helium bath was surrounded by a vacuum space, which was surrounded by a liquid nitrogen jacket. The pressure in the vacuum space could be varied to control the heat exchange between the nitrogen bath and helium bath. Temperature was controlled by pumping on the main helium bath to reduce the vapour pressure, similarly to that described is App. A3.1, with the temperature extracted using saturated vapour pressure data [106]. A roots pump was used as the primary pump, with a rotary pump as the backing pump. Since no 1 K pot was used it is more difficult to ensure a clean sample environment. In addition, the experimental volume is very large and complex when compared with cryostat:II. This system had a base temperature of 1.2 K, with a very fast cool-down time (∼ 1 hour), and decent hold-time (∼ 4 hours).

The samples were mounted onto a copper PCB with high-frequency SMP and SMA connections to room temperature. This was attached to the end of a brass probe submerged directly in the helium bath. A schematic of the system used for measurements is shown in Fig. A.5.

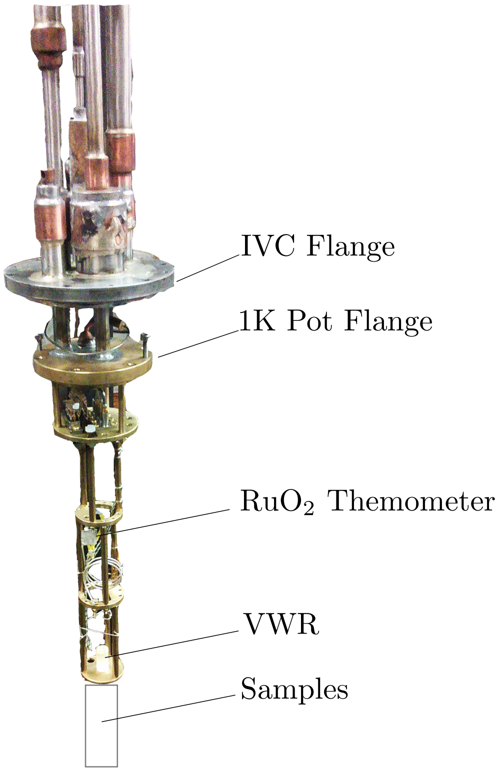
IVC Flange
1K Pot Flange
RuO_2 Themometer
VWR
Samples

Fig. A.3 Cryostat insert used to measure nanomechanical beams down to 1.5 K. Both the IVC and 1 K cans have a diameter reduction to accommodate the 5 T solenoid. The two cans are sealed using indium. The cell is mounted to a filling line and attached to the bottom of the insert. A vibrating wire resonator(VWR) and RuO_2 provide thermometry inside the system.

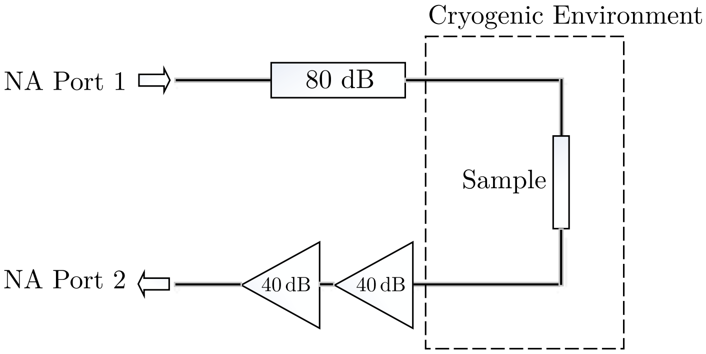
Cryogenic Environment
NA Port 1
80 dB
Sample
NA Port 2
40 dB
40 dB

Fig. A.4 The device is driven by a VNA through 80 dB of attenuation at room temperature. At the output, two 40 dB low-noise amplifiers are used at room temperature to improve the signal-to-noise ratio.

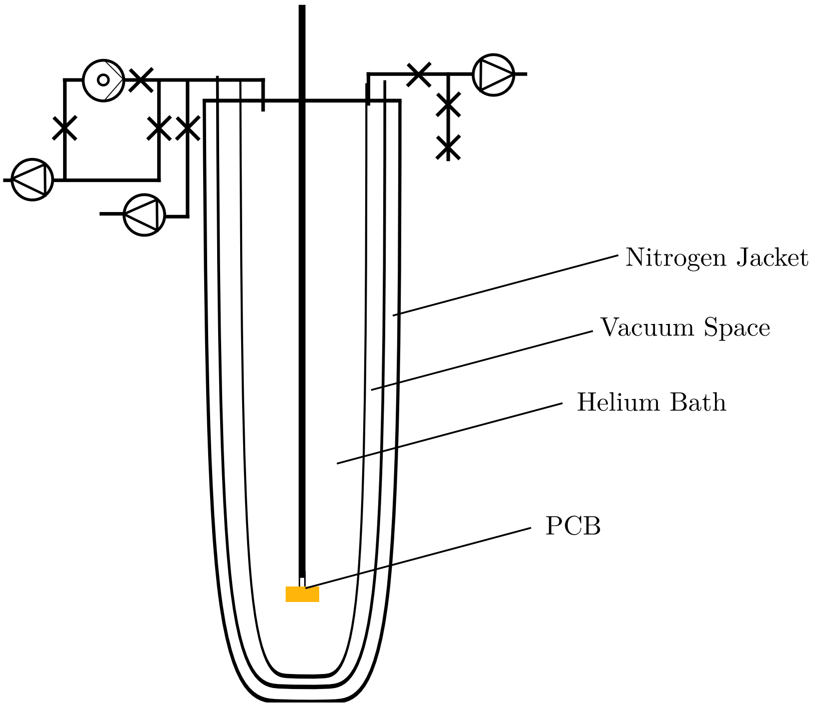
Nitrogen Jacket
Vacuum Space
Helium Bath
PCB

Fig. A.5 Schematic showing glass-cryostat and gas handling scheme used for measurements with multimode TFs, capable of reaching 1.2 K.

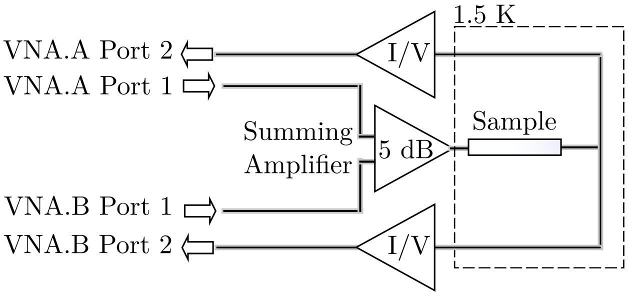
1.5 K
VNA.A Port 2
VNA.A Port 1
I/V
Summing
Amplifier
5 dB
Sample
VNA.B Port 1
VNA.B Port 2
I/V

Fig. A.6 Diagram showing an electrical setup for simultaneous measurement of two modes on the same tuning fork. Two VNAs supply two AC driving voltages at two frequencies which are combined using a summing amplifier with 5 dB gain, used to increase the dynamic range of the setup. The output current passes through an I-V converter with $10^3\,\mathrm{V\,A^{-1}}$ gain [127]. The two signals recovered using a splitter before being measured at each frequency by the two VNAs.

For measurements performed on quartz TFs with two well defined modes, two VNAs were connected for simultaneous driving. The driving signals from the two VNAs were combined using a 5 dB summing amplifier, in order to achieve a large dynamic range. The signal was then recovered using a splitter and two I-V converters, with a gain of $10^5\,\mathrm{V\,A^{-1}}$, before returning to their respective VNAs. No attenuation was used on the drive signal. A calibration was performed on both VNAs to account for possible impedence mismatches in the experimental circuit. The electrical schematic showing how the two VNAs were used to probe two modes on the same TF is shown in Fig. A.6.

A3.3 Cryogen-Free Dilution Cryostat

The cryogen-free system consists of a two-stage pulse tube with nominal stage temperatures 50 K and 3 K. These stages are associated with the two top plates, with the 3 K plate shown at the top of Fig. A.7. Further cooling is achieved by using a ^{3}He-^{4}He dilution cycle. A 96% ^{4}He mixture is condensed into the cryostat by narrow lines using a compressor stage to raise the pressure to $\sim$2 bar. The high pressure allows the ^{3}He and ^{4}He to condense at the mixing chamber, where a phase transition occurs. The mixture separates into a ^{3}He rich phase and a ^{3}He dilute phase, an endothermic process which draws heat from the cryostat into the mixture. The heat required to sustain this process produces the cooling power. Due to the phase separation, and the differing densities between the two phases, the ^{3}He rich phase can be selectively pumped away from the mixing chamber towards the still. Outgoing ^{3}He is used to cool incoming ^{3}He via a series of heat-exchangers. At the still, a heater is utilised to boil ^{3}He so it can be pumped back to room temperature, and the cycle restarted. The cooling power of a dilution unit is greatly dependent on both the circulation rate, and the effectiveness of the heat exchangers. The Bluefors LD250 cryostat is rated to have 250 μW at 100 mK. For our system, this allowed a base temperature of $\sim$ 7 K with an indefinite hold-time. However, it takes $\sim$ 2 days to reach base temperature from closing the vacuum cans.

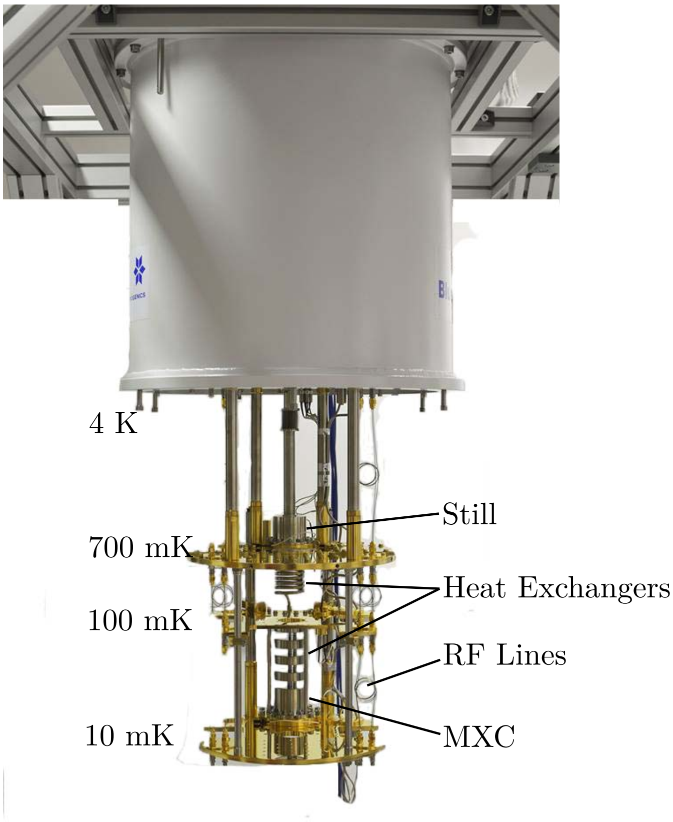

Fig. A.7 Photograph of cryogen-free dilution cryostat used for measurements down to 10 mK, with plates and dilution unit labelled.

Nanobeam measurements in ^{4}He cell

In order to perform liquid measurements at mK temperatures, a brass cell was mounted inside the vacuum of the dilution cryostat. The helium cell was mounted by fitting two 0.25 mm capillary lines, running from feed-throughs at the top of the cryostat, to the mixing chamber. To ensure adequate thermalisation, silver-sintered heat exchangers were mounted at each temperature stage. The two lines combined at the mixing chamber, and a 0.5 mm capillary connected this to the cell, which was mounted below the mixing chamber on a Tufnol cold finger. The cell was filled from a room-temperature gas handling system which allowed clean ^{4}He to be condensed by the evaporating gas from a storage dewar. Two lines to room temperature were utilised to allow a second return path for the liquid in case of a blockage. The extremely narrow capillary lines further helped the thermalisation of the condensing liquid by reducing the flow rate.

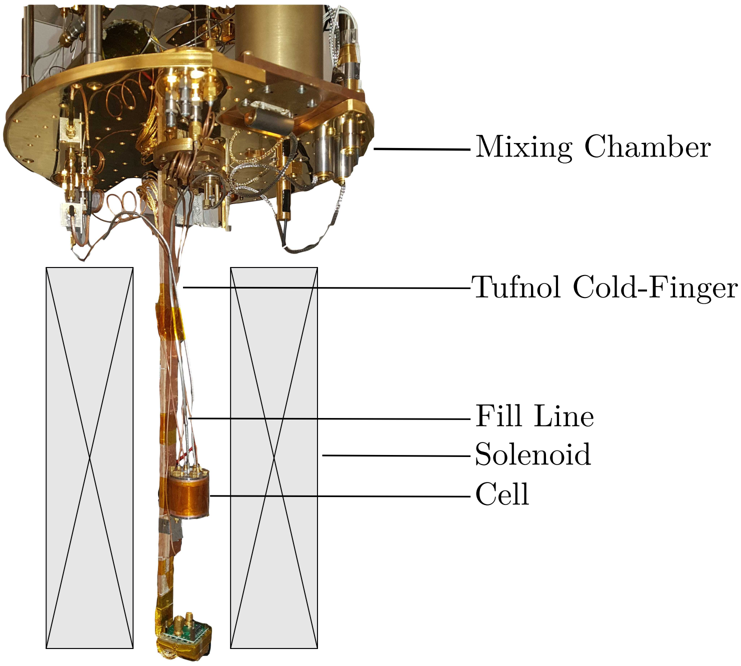

Fig. A.8 Photograph showing brass cell mounted to the cold-finger of a cryogen free dilution cryostat, with key components labelled.

Electrically, 38 dB of cold attenuation was utilised to minimise the noise temperature seen by the sample, as shown in Fig. A.9. Two 40 dB Femto HSA-X-2-40 room temperature amplifiers were utilised to improve the signal-to-noise ratio. Thermometry was provided by five calibrated resistance thermometers measured by a Lakeshore bridge. These are anchored to the 50K, 4K, magnet, still and mixing chamber. Thermometry of the samples was limited by the lack of a cell thermometer; the temperature at the mixing-chamber may not be exactly that of the sample. The temperature of the system could be varied using a heating resistor mounted to the mixing chamber. This allowed the temperature to be stably varied in the region of $10\,\mathrm{mK} < T < 1.5\,\mathrm{K}$.

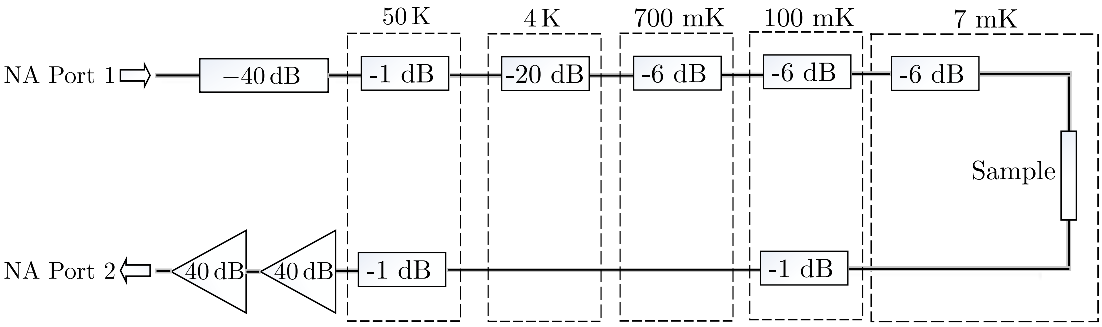

Fig. A.9 The device is driven by a network analyser through 79 dB of attenuation distributed over several temperature stages of the cryostat. At the output, two 40 dB low-noise amplifiers are used at room temperature to improve the signal-to-noise ratio. A 3 dB attenuator was used to protect the devices from amplifier noise.

Vortex measurements using nanobeams in ^{4}He cell

To perform measurements on vortex dynamics, a nanobeam and a TF were mounted inside the ^{4}He cell as described above. Electrically, the TF was driven using the schematic shown in Fig. A.10, with 20 dB of cold attenuation, and an IV converter to recover the signal. The nanobeam was measured using a multi-frequency lock-in technique (MLA) to measure the signal on short timescales. The electrical setup was the same as Fig. A.9, using an MLA instead of a VNA, and utilising an external oscilloscope as a triggering mechanism. A single feedback output from the MLA went to an oscilloscope, which sent a trigger pulse to the MLA when the signal dropped below a certain value, to begin taking measurements.

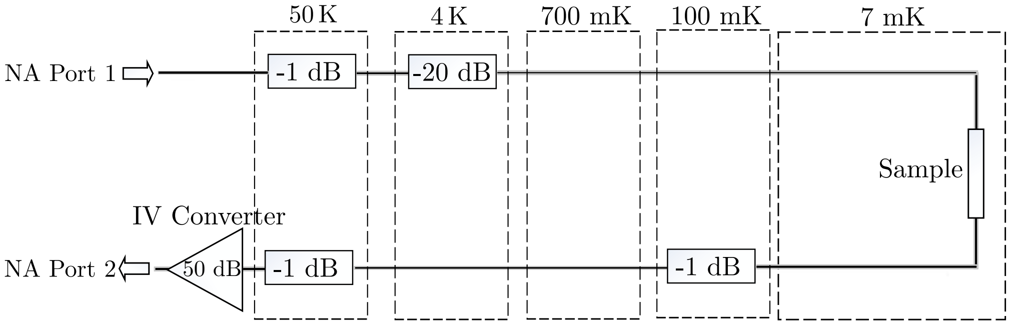

Fig. A.10 The TF is driven by a network analyser through 21 dB of attenuation distributed over several temperature stages of the cryostat. At the output, in IV converter with gain 10^5 was utilised to improve the signal-to-noise ratio.

JoFET measurements

The samples were mounted onto the mixing chamber of the cryogen-free dilution cryostat. The feedline was driven through by RF signals through 80 dB of attenuation distributed between the various temperature stages of the cryostat, as shown in Fig. A.11. DC was provided for the gates via a breakout-box connected to a 24-pin copper loom, which runs down to the mixing chamber. On the output, two cryogenic circulators were used at the 10 mK to prevent amplifier noise from reaching damaging the sample. Two Low-Noise-

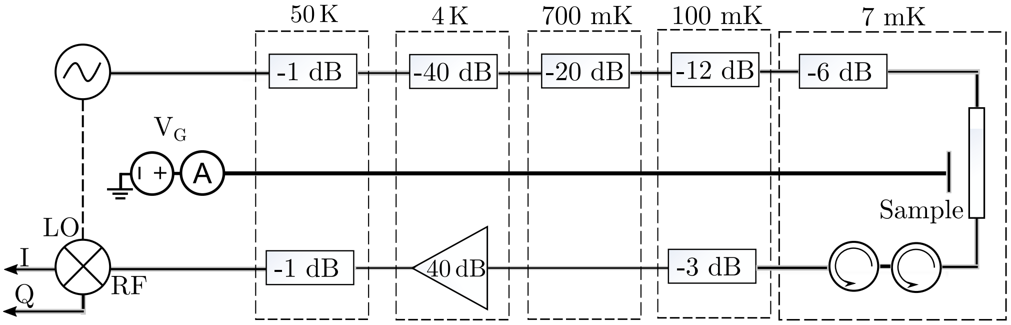
50 K
4 K
700 mK
100 mK
7 mK
-1 dB
-40 dB
-20 dB
-12 dB
-6 dB
V_G
A
Sample
LO
I
Q
RF
-1 dB
40 dB
-3 dB

Fig. A.11 The device is driven by a network analyser through 79 dB of attenuation distributed over several temperature stages of the cryostat. At the output, one 40 dB cryogenic amplifier was used at room temperature to improve the signal-to-noise ratio. A 3 dB attenuator was used to protect the devices from amplifier noise.

Factory cryogenic amplifiers were used to supply 80 dB of gain for the output signal.

Recipes

B1 Al-on-Si Nanomechanical Beams

The samples are prepared in a cleanroom environment using standard nanofabrication techniques. A silicon substrate is used, with aluminium deposited on top, and then undercut using a fluoride-based plasma to suspend the nanobeams. The full recipe is included below.

Spin Resists:

- Copolymer 6 % in Ethyl Lactate - 2000RPM - 3 min at 200°C
- 950 PMMA 2% in Anisole - 7000RPM - 3 min at 200°C

Exposure:

- 4th Lens - 2nd Aperture - 10 nA @ 50 kV

Development:

- Develop - Isopropanol:Water $(CH_3)_2CHOH$:H_2O 93:7 - 3 min
- Rinse - Isopropanol $(CH_3)_2CHOH$ - 30 s

Plasma Ashing:

- Mixing - O_2 (40 sccm) - $p = 200\,\mathrm{mTorr}$ - 3 mins
- Ashing - O_2 (40 sccm) - $p = 200\,\mathrm{mTorr}$ - $P = 50\,\mathrm{W}$ - 30 s

Deposition:

- Al - $2\,\text{Å}\,\mathrm{s}^{-1}$ - 1200 Å

Lift Off:

- Lift Off - Acetone $(CH_3)_2CO$ - 30 min
- Rinse - Water H_2O - 30 s

Silicon Etching:

- Mixing - O_2 (4 sccm), SF_6 (40 sccm) - $p = 180\,\mathrm{mTorr}$ - 5 mins
- Etching - O_2 (4 sccm), SF_6 (40 sccm) - $p = 180\,\mathrm{mTorr}$ - $P = 100\,\mathrm{W}$ - 3 min

B2 Al-on-Si_3N_4 Nanomechanical Beams

The samples fabricated in Grenoble follow the same basic steps however opt for a different substrate, and a different etchant. Si_3N_4 is grown onto Si and baked to a high temperature to pre-stress the substrate. This process helps to minimise the effect of differential contraction. XeF_2 is a highly selective etch at low pressures allowing a deep undercut to be performed, minimising the damping. Samples prepared with these techniques have typical Q-Factors around 10^5 at room temperature.

Spin Resists:

- PMMA 4% - 6000RPM - 5 min at 180°C

Exposure:

- 4th Lens - 2nd Aperture - 10 nA @ 20 kV - 250 μC cm^{-2}

Development:

- Develop - Isopropanol:MIBK $(CH_3)_2CHOH{:}(CH_3)_2CHCH_2C(O)CH_3$ 93:7 - 35 s
- Rinse - Isopropanol $(CH_3)_2CHOH$ - 1 min

Deposition:

- Al - 1 Å s^{-1} - 300 Å

Lift Off:

- Lift Off - NMP C_5H_9NO - 80°C 60 min
- Rinse - Water H_2O - 30 s

Silicon Etching:

- Etching RIE - SF_6 - 2 mins 30 s
- Etching Gas - XeF_2 - 3 min

B3 JoFETs Coupled to Superconducting Resonators

The JoFet samples were fabricated in a cleanroom environment, using a negative lithography process. The length of the final etching step allowed control over the size of the constriction.

Deposition:

- V - $2\,\text{Å}\,\text{s}^{-1}$ - $1000\,\text{Å}$

Spin Resists:

- Copolymer 6 % in Ethyl Lactate - 2000RPM - 3 min at 200°C
- 950 PMMA 2% in Anisole - 7000RPM - 3 min at 200°C

Exposure:

- 4th Lens - 2nd Aperture - 1 nA @ 50 kV
- 4th Lens - 2nd Aperture - 10 pA @ 50 kV

Development:

- Develop - Isopropanol:Water $(CH_3)_2CHOH{:}H_2O$ 93:7 - 3 min
- Rinse - Isopropanol $(CH_3)_2CHOH$ - 30 s

Plasma Ashing:

- Mixing - O_2 (40 sccm) - $p = 200\,\text{mTorr}$ - 3 mins
- Ashing - O_2 (40 sccm) - $p = 200\,\text{mTorr}$ - $P = 50\,\text{W}$ - 30 s

Vanadium Etching:

- Mixing - O_2 (4 sccm), SF_6 (40 sccm) - $p = 180\,\text{mTorr}$ - 5 mins
- Etching - O_2 (4 sccm), SF_6 (40 sccm) - $p = 180\,\text{mTorr}$ - $P = 100\,\text{W}$ - 3 min

Lift Off:

- Lift Off - Acetone $(CH_3)_2CO$ - 30 min
- Rinse - Water H_2O - 30 s

Software

A cornerstone in our ability to efficiently collect precision was the development of custom data-collection software, and analysis software. Data collection software was developed in Python, with the ability to perform spectroscopy measurements using a VNA, SA, or MLA. Results were plotted live using PyQtGraph and saved in hdf5 format. Fig. C.1 shows a sample output from the collection software. Three dimensional data was collected with the ability to vary arbitrary experimental parameters with many instrument drivers implemented. Adding new instruments was made as simple as possible to implement for rapidly changing experiments. For every frequency sweep measurement performed, each parameters is remeasured in case of experimental drift. Due to the speed of plotting in PyQtgraph, and saving in hdf5, the only limiting factor in the rate of data collection is that of the instrument measurement speed. For the experiments discussed, some measurements were performed with each frequency sweep taking just $\sim 0.1\,\mathrm{s}$ Additionally, experimental parameters were automatically written to a LateX logbook to allow for efficient analysis of collected data files. Included here was the path to the saved data, instruments, all parameters start and finish values, various cryostat temperatures and timestamps.

Lorentzian fitting was performed using custom python scripts capable of reading large hdf5 datasets, subtracting polynomial backgrounds, estimating close initial parameters, and then fitting to output the exact parameters for arbitrary phase. A least squares fitting routine was utilised on the real and imaginary components of the signal by default, however the user can choose fit individual components. The user can select in real-time whether to accept or reject each individual fit, allowing for easy vetting of misfits. The scripts were able to operate with a high degree of accuracy, fitting thousands of individual curves without error. The Lorentzian amplitude, width, phase offset, polynomial backgrounds and centre frequency are returned, allowing the calculation of the resonance Q-factor. A sample fitting is shown in Fig. C.2. Analysed datasets are saved back into hdf5 format in a new folder with the same timestamped named. This workflow allowed rapid prototyping of experimental setups, and real-time updates to experiments and analysis to allow for specific operations since all code was written in-house.

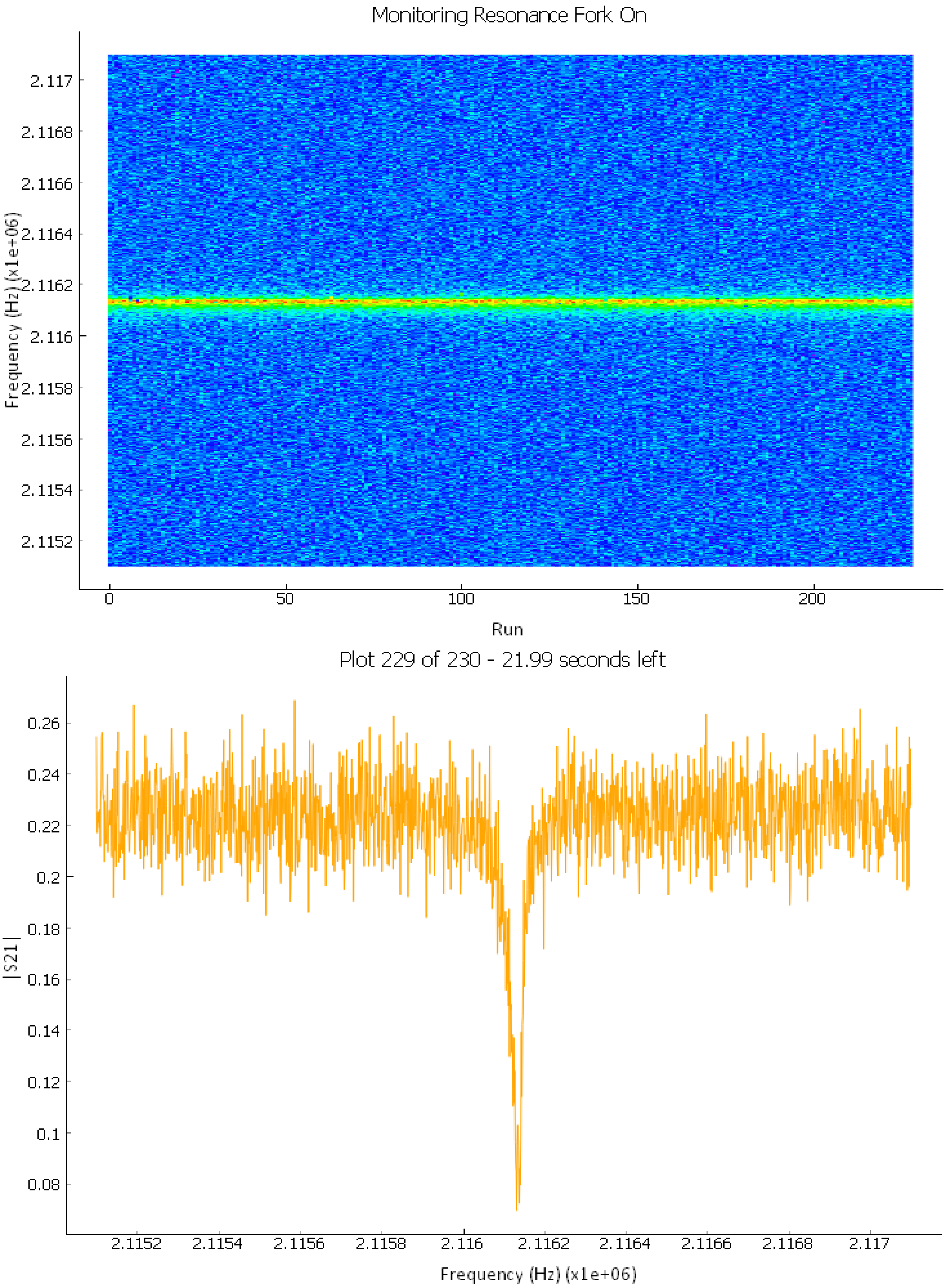
Monitoring Resonance Fork On
Frequency (Hz) (x1e+06)
2.117
2.1168
2.1166
2.1164
2.1162
2.116
2.1158
2.1156
2.1154
2.1152
0
50
100
150
200
Run
Plot 229 of 230 - 21.99 seconds left
|S21|
0.26
0.24
0.22
0.2
0.18
0.16
0.14
0.12
0.1
0.08
2.1152
2.1154
2.1156
2.1158
2.116
2.1162
2.1164
2.1166
2.1168
2.117
Frequency (Hz) (x1e+06)

Fig. C.1 Live-plotting GUI for the data-collection software.

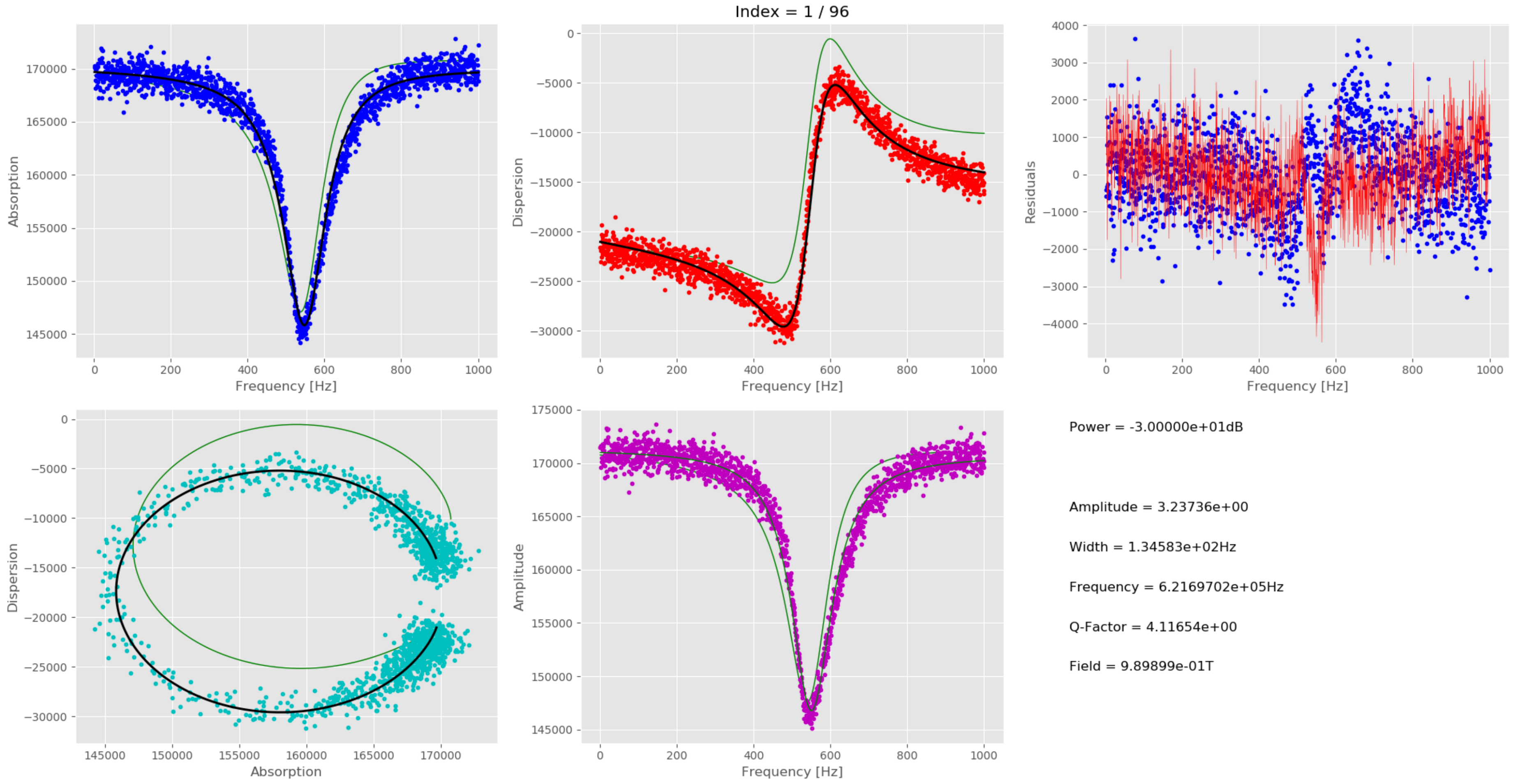

Fig. C.2 Live-plotting output for the data analysis script.